5-2022

# 2D materials based heterostructure for quantum tunneling: a lithography free technique.

Ali Alzahrani
*University of Louisville*

## Recommended Citation

Alzahrani, Ali, "2D materials based heterostructure for quantum tunneling: a lithography free technique." (2022). *Electronic Theses and Dissertations.* Paper 3985.
Retrieved from https://ir.library.louisville.edu/etd/3985

# 2D MATERIALS BASED HETEROSTRUCTURES FOR QUANTUM TUNNELING: A LITHOGRAPHY FREE TECHNIQUE

By

Ali Alzahrani

B.S., Umm-Alqura University, 2005

M.S., Western Illinois University, 2016

M.S., University of Louisville, 2019

A Dissertation

Submitted to the Faculty of

College of Art and Sciences of the at the University of Louisville

in Partial Fulfillment of the Requirements

for the Degree of

Doctor of Philosophy in Physics

Department of Physics and Astronomy

University of Louisville

Louisville, Kentucky

May 2022

# 2D MATERIALS BASED HETEROSTRUCTURES FOR QUANTUM TUNNELING: A LITHOGRAPHY FREE TECHNIQUE

By

Ali Alzahrani

B.S., Umm-Alqura University, 2005

M.S., Western Illinois University, 2016

M.S., University of Louisville, 2019

A Dissertation Approved on

March 31st, 2022

by the following Dissertation Committee:

Dr. Gamini Sumanasekera (Dissertation Director)

Dr. Mendes Sergio

Dr. Ming Yu

Dr. Xiao-An Fu

# ACKNOWLEDGEMENT

I would want to thank everyone whose contributions and efforts helped make this thesis a success. First and foremost, I want to thank my Ph.D. adviser, Dr. Gamini Sumanasekera, for his unwavering support and guidance during this process. I learned a lot from his expertise, and his criticism has always been invaluable, and I am grateful for the chance to work under his capable leadership and join his distinguished research team. The knowledge and talents I gained from him have tremendously aided my scientific career.

Next, I'd want to thank all the instructors who taught me courses throughout my Ph.D. studies, especially Dr. Chakram S. Jayanthi, Chair of the University of Louisville's Physics Department, Dr. Shudun Liu, and Dr. Ming Yu, Professor of Physics, who all provided me with vital guidance. It was a privilege to study with them, and I am glad for the chance. I'd also want to thank Dr. Chris. L Davis, my graduate program director, for his important advice on everything from course selection to major decisions during my Ph.D. journey. Dr. Chris. L Davis is a wonderful student adviser who is always nice, friendly, and considerate to his students. For his compassion toward me, I will be eternally grateful.

I'm also appreciative to the Conn Center for Renewable Energy's illustrious staff, who have always been willing to help, support, and assist me in any way they can. Dr. Thad Druffel and Jacek B. Jasinski.Dr. Sergio B. Mendes, Dr. Xiao An Fu, and Dr. Ming Yu were also members of my committee, for that I am grateful. I appreciate their time and valuable input.

I'd want to thank my beloved friends and Physics department staff members, particularly Ms. Mary Gayle Wrocklage, Ms. Missy Klotz, and Mr. Joshua Rimmer, for making my lab experience wonderful. Also, I would thank my friend Milinda for his help and support for me when I needed any kind of help, I am very grateful for his help despite his busy schedule. This was my chance to thank him, and I wish that he will have a fascinating future.

I'd like also to acknowledge and appreciate my Ph.D. sponsor, the Department of Physics, Al-Qunfudah University College, Umm Al-Qura University, Makkah, Saudi Arabia, provided me with a full scholarship to pursue my doctorate. As a result, I have been able to continue my studies at the University of Louisville

Finally, I'd want to thank my family, especially my parents, Mr. Ibrahim Mohamed Alzahrani and Mrs. Baraka Ahmed Alzahrani, my brothers, Mohamed Ibrahim Alzahrani and Saeed Ibrahim Alzahrani, and all my sisters. I owe a big debt of appreciation to my wonderful wife and adorable children. My family's patience, sympathy, and spiritual support provided me with a huge sense of relief, allowing me to focus entirely on my academics. Their never-ending prayers have been a gift to me, and I think it is because of them that I have achieved this amazing achievement.

# ABSTRACT

# 2D MATERIALS BASED HETEROSTRUCTURES FOR QUANTUM TUNNELING: A LITHOGRAPHY FREE TECHNIQUE

Ali Alzahrani

March 31st, 2022

Two-dimensional electron gas (2DEG) systems have played a vital role in the development of superior electronic devices including tunnel junctions consisting of two such 2DEG systems. With the advent of the new 2D electronic material systems, it has opened a new route for 2D–2D tunneling in such extended systems

In this study, we have utilized a plasma enhanced chemical vapor deposition (PECVD) technique to directly deposit graphene (nanowalls) and h-BN on Si/SiO$_2$ substrates to construct two-dimensional material based, vertically stacked electron tunneling devices free of expensive and cumbersome microfabrication steps.

In the first study, we fabricated direct quantum tunneling devices by depositing atomically thin tunnel barriers of h-BN as the tunneling barrier with equally doped (p-doped under ambient conditions) graphene nanowalls as the active electrode layers (top and bottom) on Si/SiO$_2$ substrates. Current-voltage (I-V) measurements for varying h-BN thicknesses of these single barrier tunneling devices showed linear I-V characteristics at low bias but an exponential dependence at higher bias. Our measurements of the electron tunnel current through the barrier demonstrated that the h-BN films act as a good tunnel barrier. The

barrier thickness dependent tunneling current was in good agreement with the tunnelling currents computed using the Bardeen transfer Hamiltonian approach with equally doped top and bottom graphene electrodes.

Presence of negative differential resistance (NDR) is characteristic of the current–voltage relationship of a resonant tunneling device, enabling many unique applications. NDR arises at a voltage bias corresponding to aligned band structures of the 2D systems, causing a sharp peak in the tunnelling current. The existence of devices with NDR has been reported since the late 1950's in devices that contained degenerately doped p-n junctions with thin oxide barriers (tunnel diodes) and double barrier heterojunction devices where quantum tunneling effects are utilized. The NDR in the I-V characteristics of these devices has been used in many applications involving microwave/millimeter wave oscillators, high speed logic devices and switches. We investigated NDR phenomenon in our graphene/h-BN systems in two different routes. In the first case, graphene/h-BN/graphene single barrier device, the bottom and top graphene layers were unequally doped. One of the graphene layers was n-type doped using ammonia or hydrazine. Nitrogen doping using ammonia was accomplished during the growth by incorporating ammonia in the PECVD system. Hydrazine doping was accomplished by exposing the graphene to hydrazine vapor in vacuum. The unequal doping of graphene causes alignment of the band structures of graphene systems giving rise to NDR. The tunnelling devices consisting of unequally doped graphene with a single barrier shows resonant quantum tunneling with the presence of a pronounced peak in the current corresponding to NDC whose peak current value and the voltage value depend on the doping levels. The results are explained according to the modified Bardeen tunneling model.

Next, resonant tunneling behavior was demonstrated in Graphene/h-BN/Graphene/h-BN/Graphene double barrier (DB) devices by directly depositing graphene and h-BN successive layers on Si/SiO2 substrates using PECVD. DB Tunneling junctions with various barrier widths were investigated (by varying the thickness of the second graphene layer). The I-V parameters of tunneling current at room temperature demonstrated resonant tunneling with negative differential conductance. A quantum mechanical double barrier tunneling model was used to explain the phenomenon, by solving the Schrödinger's equation in either side of the system. A systematic behavior of the current peak values and the corresponding voltage values in I-V curves were seen to be in good agreement with the transmission coefficient calculated using a quantum mechanical model.

Josephson tunneling is a different kind of tunneling phenomenon in superconductors, in which superconducting cooper pairs tunnel across a thin insulating barrier. A supercurrent can flow between two superconductors that are separated by a narrow insulating barrier. The current is influenced by the phase difference between the two superconductors. We fabricated Josephson junctions with atomically thin tunnel barriers by combining h-BN with magnesium diboride ($MgB_2$) active electrode layers on a $Si/SiO_2$ substrate using a PECVD (for h-BN) and a Hybrid Physical-Chemical Vapor Deposition (HPCVD) (for $MgB_2$). The I-V characteristics were measured above and below the transition temperature $T_c$ (37 K). A measurable supercurrent was detected below $T_c$.

# TABLE OF CONTENTS

# LIST OF TABLES

# LIST OF FIGURES:

# CHAPTER 01

# INTRODUCTION

## 1.1 Two-dimensional heterostructures:

Due to their unique and interesting structural, physical and chemical features, two-dimensional (2D) materials are attracting attention from a variety of disciplines and industries[1]. These two-dimensional materials have a crystal structure that resembles bulk layered crystals with weak van der Waals forces connecting the layers. Whether printed laterally on substrates or layered in heterostructures, 2D materials are crucial for device development[2]. A vertical 2D heterostructure is formed when two two-dimensional materials are layered on top of each other[3]. Regardless, the layers are frequently composed of several types of crystals with mismatched lattices.

In several important respects, traditional three-dimensional(3D) semiconductor heterostructures differ from these stacked devices[4]. The layers of a 2D heterostructure function both as a bulk material and as an interface, reducing load displacement within each layer. On the other hand, charge transfers between layers can be significant, resulting in high-quality electric powered fields and exciting band structure engineering possibilities[5].

2D physics, often known as physics of 2D materials and heterostructures, is a fascinating new field of study. Long-range order, 2D excitons, equal-unequal transition, and peculiar physics are all required for the fabrication of innovative heterostructure devices such as modest emitting diodes, tunneling transistors, and resonant tunneling diodes[6], among others. The final size scale of such 2D materials, 2D heterostructures, and their related specific properties may also be beneficial to device innovation. Different heterostructures feature strong connections between two or more construction components, resulting in increased functional properties. Each component adds to the system's multifunctionality in its own unique way. Researchers employed a variety of synthetic ways to produce heterostructures[7]. The influence of recent developments in nucleation processes and heterostructure formation on interfacial behavior and structural features has been investigated. It's critical to comprehend how various heterostructures are formed. A regulated development process employing 1D, 2D, or 3D building components is required for integrated design and synthesis of heterostructures[8]. Heterostructures may be constructed in three ways: sequentially growing discrete material components, directly growing independent construction pieces, and simultaneously developing several areas by guiding the building blocks.

The size, shape, and uniformity of building blocks, including the design and synthesis of complex heterostructures with meticulously regulated assembly of each material component[9], are all critical components in improving the physical characteristics of heterojunctions. Understanding the underlying mechanics of nucleation and development, as well as the unidirectional growth of crystal facets, might be immensely useful in the development of functional nanostructure devices[10]. Great productivity, noncontaminated heterostructures, and minimum aggregation effects in conventional and innovative synthesis techniques are in high demand. Systematic research is also required to completely comprehend the morphological development of heterostructures. Heterostructures composed of two dissimilar nanomaterials outperform single-material equivalents[11]. A nanotube's internal channel is smaller than 100 nm in diameter, making it excellent for encapsulating metals, metal oxides[12], organic chemicals, pharmaceuticals, and therapeutic treatments. By filling nanotubes with different materials, nanotube heterostructures[13] can be employed as magnetic materials, catalysts, drug transporters, and biomedical imaging.

There are two forms of heterostructures in the layered system: stacked heterostructures, which are generated by sequential vertical stacking of distinct 2D materials, and layered heterostructures[14]. Multiple molecules are bonded inside the planes of the area to generate in-plane (lateral) heterostructures. Stacked structures, on the other hand, may be formed by combining and then transferring many synthesis processes. One method is to chemically etch the substrate to remove it from the single layer coating. The emitted film can then be layered on additional monolayer films to create a multilayer heterostructure. Complex heterostructures are created using techniques such as chemical etching, electrostatic transfer, mechanical separation, and chemical vapor deposition[15]. The in-plane heterostructure, on the other hand, has proven to be much more challenging to synthesize.

The purpose of heterostructure development is to integrate systems with qualities that are unique from the system's individual components[16]. Transition metal Dichalcogenides (TMDs) produce a natural stacking or homo-structure for various layers of the same TMD as a result of this[17]. One such theoretical study found that by stacking TMDs with the same transition metal but distinct chalcogen atoms, the direct bandgap electrical structure that is generally only seen in monolayer TMDs might be preserved[18]. The change from direct to indirect bandgap happens when the same TMDs are doubled. The straight bandgap has the benefit of being more efficient in photon use. Another significant advantage is the band alignment of each material. The conduction band minimum (CBM) and valence band maximum (VBM) of each material are modified to equilibrium when the various systems in heterostructures come into contact[19]. The charges are exchanged between the materials in a significant way when their respective Fermi levels approach their equilibrium point. As a result, the CBM of the connected system may be included inside a single material, while the VBM may be housed within another[20]. Due to layer separation, electrons and holes are physically separated in the CBM and VBM. Photocatalysis, solar cells, photodetectors, and other junction devices benefit from the separation because the exciton lifespan increases[21].

This research examines direct deposition of 2D materials using a plasma enhanced chemical vapor deposition technique and non-microfabrication approaches for manufacturing 2D material based heterostructures[22]. The electrical properties of these devices have also been thoroughly examined. Specifically, (i) direct quantum tunneling, (ii) resonant quantum tunneling (asymmetric doping and double barrier) and (iii) Josephson tunneling have been studied.

### 1.2. Two dimensional Materials:

Materials with two dimensions (the XY plane) and atomic-scale thicknesses higher than nanometers are referred to be two-dimensional (two-dimensional) (Z dimension)[23]. Graphene, a single sheet of hexagonally arranged carbon atoms[24], was the first two-dimensional substance. Material research in 2D (graphene) has advanced faster than research in 0D (fullerene) and 1D (carbon nanotubes) [25]as shown in Figure 1. Other 2D materials such as tungsten disulfide, molybdenum disulfide, and silicon nitride provide up additional possibilities for future devices[26], in addition to 2D graphene and h-BN, which have been widely used in a number of possible applications[27]. This chapter has introduced and discussed the creation and applications of numerous 2D materials.

#### 1.2.1. Transition metal dichalcogenides' history (TMDCs):

When a transition metal atom is joined to two atoms from Group 16 (chalcogen) of the periodic table, transition metal dichalcogenides are created[28]**.**Figure 1. depicts 44 transition metal dichalcogenides (TMD) compounds made up of transition metals and three chalcogen elements.

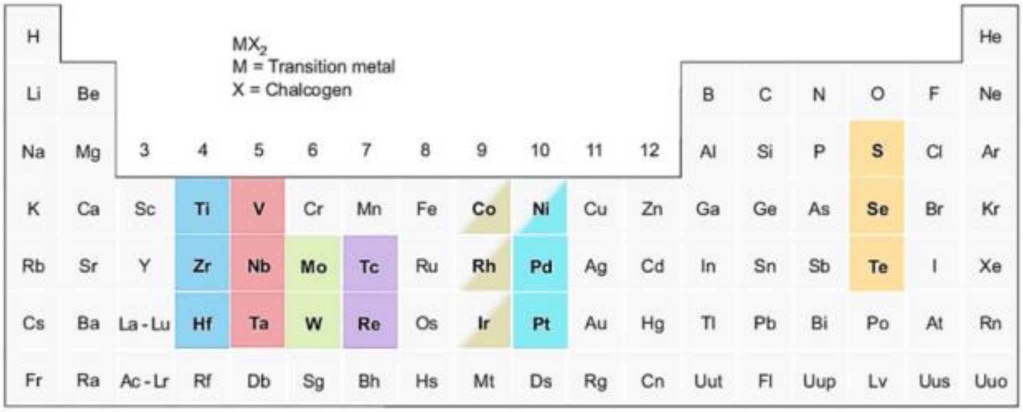

Figure 1 The periodic table with transition metals and three chalcogen elements[29, 30].

They've been used as additives to minimize friction through lubrication for decades. They sparked interest[30], however, when graphene was introduced in 2004. TMDs have also been proven to be capable of catalysis[31]. The margins of monolayer $MoS_2$ have been shown to be extremely active catalytic sites, whereas the basal plane is catalytically inactive[32]. Furthermore, extraordinary optical properties [33]have also been observed, such as room temperature photoluminescence in a single layer of $WSe_2$ and $WS_2$.

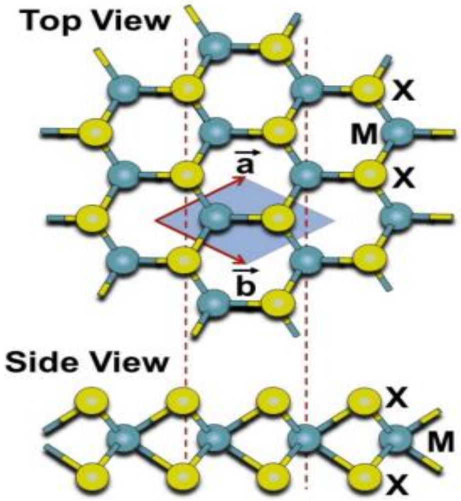

Figure 2: Monolayer structure of various TMDs

TMDs are made up of many layers stacked vertically on top of one another[34]. layers of material are arranged in a manner that allows them to be stacked vertically[35]. They have hexagonal Orth rhombohedral symmetry (Figure2).

Previously, multiple layers of TMDs could be separated using a mechanical exfoliation approach to create a single layer TMD[36], hence the presented work has increased the number of TMD systems available. As a result of this approach, new materials, such as monolayer TMDs with metallic, semiconducting, or insulating properties, have been created[37]. They have a variety of qualities that vary depending on how many layers are present in the specimen. The stacking number influences photoluminescence, band structures, conductivity, and vibrational modes. Along with its monolayer form and tunable properties, TMDs are a very promising material in microelectronics and other fields[38]. In monolayer TMDs, for example, the photoluminescence (PL) effect is induced by a transition from indirect bandgap (in bulk) to direct bandgap (in single-layer form)[39]. Since this lack of inter-layer van der Waals contact may modify the restoring forces of the lattice vibrations, the phonon modes in single-layer sheets can also shift.

The $MX_2$ TMD grouping is the most well-known, with M = Mo, W and X = S, Se, Te. In the electronic configuration $1s^2\ 2s^2\ p^6\ 3s^2\ p^6\ d^{10}\ 4s^2\ p^6\ d^5\ 5s^1$, molybdenum has 42 electrons[40], whereas sulfur has 16 electrons in the electronic configuration $1s^2\ 2s^2\ {}_2p^6\ {}_3s^2\ {}_3p^4$. Because of the 4d orbital of molybdenum and the 3p orbital of sulfur, in-plane bonding is covalent. TMDs are interested by out-of-plane bonding. The van der Waals forces interplay between the neighbors of each layer. TMDs can be manufactured in monolayer form since the attraction is minimal (15–20 meV/$Å^2$)compared to in-plane forces[41].

In a monolayer, TMDs exhibit a bandgap ranging from 1.0 to 2.5 eV. Due to a drop in energy at the point and an increase in energy at the K point in the energy dispersion relation as the number of layers decreases[42], the bandgap of $WS_2$ rises[43]. Many heterostructures may be created since the TMD group has a tiny lattice misfit and is a van der Waals material[44]. You can accomplish bandgap engineering, absorption augmentation, and developed charge separation with the structures mentioned above. Due to the obvious exceptional properties of TMDs, these materials are in high demand for a wide range of innovative optoelectronic devices[45]. Field effect transistors, photocatalysis, photovoltaics, and logic circuits have all been investigated thus far[46]. At the laboratory scale, the physics of these monolayer compounds has been shown to be quite rich and to have a variety of device presentations. The vertically stacked heterostructures of graphene/h-BN that have been manufactured are an outstanding example[47], while graphene/$MoS_2$/graphene and graphene/$WS_2$/graphene have been utilized to explain photoactive semiconductors[48]. Hypothetical considerations show that obtaining a direct bandgap layered material with the proper mix of rotated TMD sheets is likely; particularly when the chalcogen iota is changed in the abutting layers, the photogenerated electrons and openings might be contained in surrounding layers. The rapid shift of TMD components has recently resulted in the advancement of $WSe_2$/$MoS_2$ heterojunctions with photovoltaic activity[49].

Water splitting may be possible with certain TMD band alignments based on 2D heterojunctions[50]. Even though quantum structures are so sensitive, thickness engineering has been utilized to speed up manufacturing[51]. The band compensates for the lack of layers by performing a different piece.

### 1.2.2. Background of Two Dimensional of Graphene:

When layered 2D materials are pushed to their physical limits, a trait emerges that distinguishes them from bulk counterparts. Because of its amazing optoelectronic, electrochemical, and biological implications, graphene is the most studied two-dimensional materials[52].

Carbon is a periodic table group 14 element found in all biological compounds, as well as the earth's crust and atmosphere[53]. Because of the flexibility of their chemical bonds, carbon-based systems can have an endless number of different structures with varying physical properties. Only a few examples of carbon-structured materials are graphite, diamond, and amorphous carbon[54]. The sixth atomic number is carbon, which has the electron configuration $2s^2$ $2p^2$. Carbon atoms form covalent chemical connections via the $sp^1$, $sp^2$, and $sp^3$ hybridization processes. With a layered structure, intralayer $sp^2$ hybridization, and interlayer van der Waals interactions, graphite is the best-known $sp^2$ hybridized carbon allotrope[55]. Graphitic materials are classified into four categories, each with its own set of features (See Figure 3). Graphitic is a three-dimensional graphene material that may be utilized to create three-dimensional structures[56]. 3D graphite is produced by stacking graphene sheets, 1D nanotubes are produced by rolling graphene sheets, and 0D fullerene is produced by wrapping graphene sheets[57].

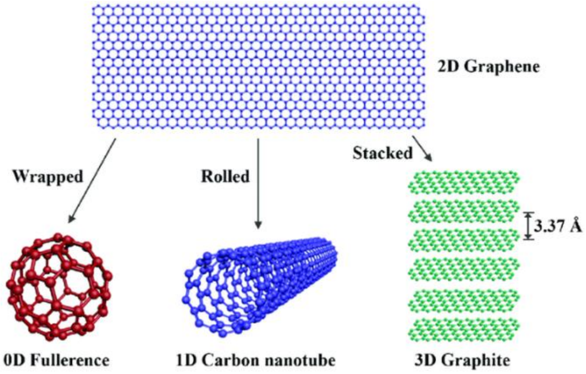

Figure 3: 2D-graphene, 3D-graphite, 0D-fullerene, and 1D-nanotube are all graphitic materials with increasing dimensionalities, clockwise from top left.

Scientists employ graphene, a two-dimensional nonmaterial made up of a one-atom-thick planar sheet. It was formerly thought to be a thermodynamically unstable chemical that couldn't stand on its own. In 1947, Canadian researcher Philip Wallace was the first to discover graphene's remarkable electrical characteristics[58]. Despite being assumed for decades to be only useful for academic and theoretical purposes, Geim, Novoselov, and colleagues succeeded in constructing the elusive free-standing graphene sheet, a breakthrough in graphene research that earned them the Nobel Prize in Physics in 2010[59]. Graphene, a two-dimensional honeycomb lattice formed of a monolayer of carbon atoms, is the basis for graphitic materials of various dimensions.

Graphene is an outstanding condensed material in terms of (2+1) dimensions quantum electrodynamics, according to scientific research conducted over the last forty years. This research was essential in establishing graphene as a realistic theoretical model. In charge carriers, the graphene scan looked for the lack of mass Dirac fermions[60]. The potential of graphene's characteristic sparked the interest of researchers.

Landau and Peierls predicted over 70 years ago that 2D crystals would not form and would be thermodynamically unstable[61]. They anticipated that variations in temperature would cause their interatomic range to fluctuate. As a result of the diverging contributions of thermal fluctuations to a low-dimensional crystal lattice, displacements proportional to the interatomic range may occur. The outcomes of the experiments validated this hypothesis.

According to the experimental discovery of graphene and other free-standing 2D atomic crystals, researchers have been able to grow crystals on non-crystalline surfaces and in liquid suspensions (e.g., single-layer boron nitride). A 2D crystal has a single atomic plane, whilst a thin film of a 3D material has several layers. Ten to twenty layers of graphene are typically considered three-dimensional[62].

### 1.2.2.1 Band structure of graphene:

Wallace became the first to study the electrical energy bands structure of graphene[63]. He explained that as semimetal because of the bands lack an energy gap between the valance and conduction bands, therefore, that the density of states decreases at the Brillouin region corners by using the tight binding approach[64].

As seen in Figure4. (a), the Fermi level is precisely at the Dirac point, which is the point where graphene atoms meet in undoped graphene[65], showing that it is a zero-bandgap semiconductor. This level offers the carriers a constant Fermi velocity, allowing them to be changed from hole-like to electron-like by an external gate.

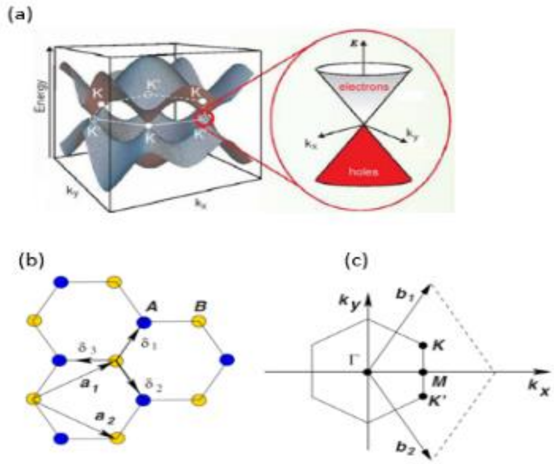

Figure 4: (a) Graphene band structure and its honeycomb lattice. Right: an enlarged image of one of a Dirac point's energy bands. (b) The primordial $a_i$ (i =1,2) vectors and nearest neighbor $\delta_i$ vectors are contained in a hexagonal graphene lattice. On the graphene Brillouin zone, the Dirac points[66] K and K' are represented.

The geometry of graphene is a triangular lattice with a base of two atoms for each unit cell[67], as seen in Figure 4; the lattice vectors are[68] provided by

$$\boldsymbol{a}_1 = a\,(3, \sqrt{3}),\ \boldsymbol{a}_2 = a\,(3, -\sqrt{3}), \qquad (1\text{-}1)$$

where a ≈1.42 Å. On the other hand, the reciprocal-lattice is represented by the vectors

$$\boldsymbol{b}_1 = \frac{2\pi}{3a}\,(1, \sqrt{3}),\ \boldsymbol{b}_2 = \frac{2\pi}{3a}\,(1, -\sqrt{3}) \qquad (1\text{-}2)$$

The positions of Dirac points are represented by the vectors

$$\boldsymbol{K} = \frac{2\pi}{3a}, \frac{2\pi}{3\sqrt{3a}},\ \boldsymbol{K}' = \frac{2\pi}{3a}, -\frac{2\pi}{3\sqrt{3a}}, \qquad (1\text{-}3)$$

The three nearest neighbor vectors in real space are represented by

$$\boldsymbol{\delta_1} = \frac{a}{2}\,(1, \sqrt{3}),\ \ \boldsymbol{\delta_2} = \frac{a}{2}\,(1, -\sqrt{3}),\ \boldsymbol{\delta_3} = -a\,(1, 0) \qquad (1\text{-}4)$$

The location of six second nearest neighbors is at

$$\boldsymbol{\delta_1}' = \pm a_1,\ \boldsymbol{\delta_2}' = \pm a_2,\ \boldsymbol{\delta_3}' = \pm\,(a_2 - a_1).$$

The tight-binding Hamiltonian for each electron in graphene is given by

$$H = -t\sum\nolimits_{<i,j>,\sigma}(a^{+}_{\sigma,i}b_{\sigma,j} + H.C.) - t\sum\nolimits_{\ll i,j\gg,\sigma}(a^{+}_{\sigma,i}a_{\sigma,i}\ + b^{+}_{\sigma,i}\,b_{\sigma,j} + H.C.) \qquad (1\text{-}5)$$

The general energy bands derived from this Hamiltonian [69]has the following form [10]:

$$E_{\pm}(k) = \pm t\sqrt{3 + \mathrm{f(k)}} - t'\,f(\mathrm{k}), \qquad (1\text{-}6)$$

$$f(\mathrm{k}) = 2\cos(\sqrt{3}k_y a) + 4\cos\left(\frac{\sqrt{3}}{2}\,k_y a\right) + cos\left(\frac{3}{2}\,k_x a\right), \qquad (1\text{-}7)$$

The top r (π*) band is represented by a plus symbol, while the bottom (π) band is represented by a minus sign.

In graphene's case, there's no bandgap, therefore its conductivity cannot be switched on and off using a gate voltage to represent Fermi's temperature, prohibiting it from being employed in conventional transistor applications.

### 1.2.2.2 Properties and Potential Applications of Graphene:

A pristine graphene sheet is made up of two carbon atoms. Each carbon atom has four valence electrons, three of which are needed to form chemical bonds. The bonding energy of a single C-C bond in graphene is 4.93 eV[70]. Due to their parallel arrangement, the remaining 2p orbitals on each carbon atom form highly delocalized π bonds. Graphene has properties that are broadly categorized, and in a one-unit cell there are two electrons, corresponding to two π bands π, π* and, with the π corresponding to the valence band and the π*corresponding to the conduction band[71].

Graphene's mechanical properties: graphene is very light[72], weighing just 0.77 g/$m^2$. The experimentally determined second- and third-order elastic stiffnesses of graphene[73] are $E^{2D}$ = 340 ± 50 Nm–1 and $D^{2D}$ = –690 ± 120 Nm–1, respectively. The intrinsic length of $\sigma^{2D}$int = 42 ± 4Nm–1is the Young's modulus, while D = –2.0 ± 0.4 T P is the third-order elastic stiffness.

Graphene's Electronics properties: as there is no bandgap[74], the charge carriers in graphene have a lower effective mass; the graphene monolayer has an electrical[75] conductivity of (4.84–5.30) 103 W mK−1and charge mobility of 200,000 cm2V-1s-1. Even though graphene absorbs 2.3 percent of light[76], it can interact with all wavelengths of light. It is also claimed that graphene has a heat conductivity of 3000–5000 Wm-1K-1[77].

Graphene is projected to be useful in the following applications: Because transparent graphene electrode layers are suitable materials[78], they might be employed in solar cells and touch displays[79]. They can also help lithium batteries lose weight, which is why they're used in the anode to create a tunnel for lithium ions to adhere to the substrate. As a result, micro cells are increasingly being used in next-generation power systems. Supercapacitors are most likely to be used as conductive plates in electric vehicles, planes, and automobiles due to their large surface area to mass ratio. Because of a feature of green energy solutions in electric vehicles, aircraft, and automobiles, such an application can have a significant impact. Graphene may be used in a variety of ways. For example, it might be used to detect glucose[80], cholesterol[81], hemoglobin[82], and cancer cells[83]. Because the carbon atoms in its structure are exposed to the environment, it is particularly sensitive to changes in molecular activity.

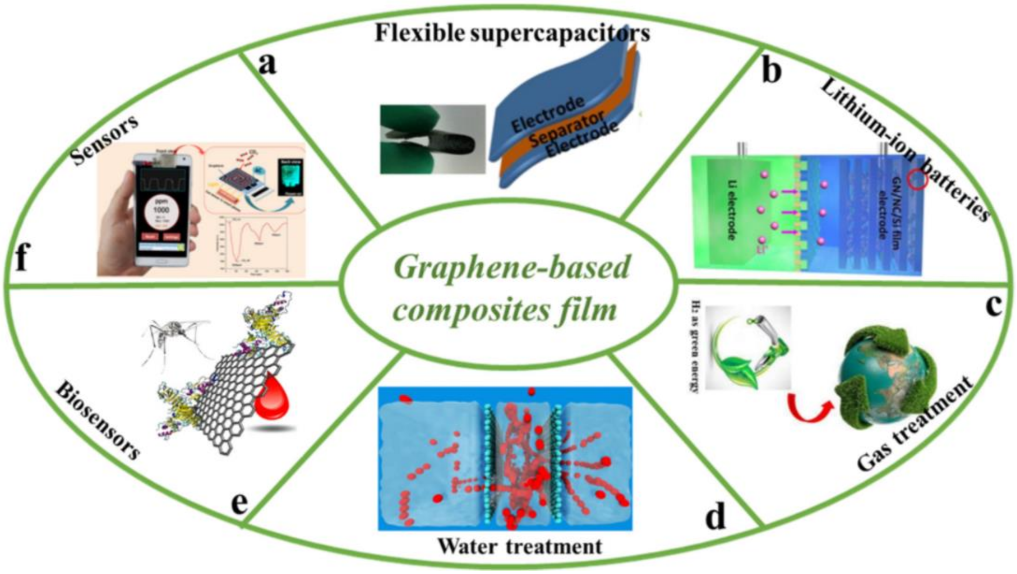

Figure 5: Commercial graphene applications[84]

Figure 5 demonstrates graphene's industrial applications; it's been widely used in semiconductors, electronics, optoelectronics, and energy applications (primarily rechargeable battery), as opposed to aerospace, composites, medicine, and telecommunications[85]. Many obstacles must be overcome before graphene's promise in terms of technological and economic applications [86]may be realized. Among the challenges are the expensive cost of large-scale synthesis and a lack of knowledge of its electrical sensitivity.

### 1.2.3 Hexagonal Boron Nitride Background:

Hexagonal boron nitride stands apart from other types of carbon due to its hexagonal structure. Hexagonal boron nitride, found in the carbon system, is a white powder[87]. As a result, it has a greater range of applications. It's a graphite allotrope called graphene that has a graphite-like structure.

At the start of the nineteenth century, boron nitride was discovered[88], and various attempts to manufacture it were attempted. Mechanical exfoliation was employed by a team from the University of Manchester to create a two-dimensional h-BN in 2005[89]. Nagashima et al. grew an h-BN epitaxially on metal surfaces to form an h-BN. Boron nitride is a III-V material that can exist in several different states. Some of the various types include hexagonal to crystalline, amorphous, cubic, and wurtzite[90]. The most common kind is hexagonal graphite, sometimes known as white graphite. It is made up of 0.33 nm thick hexagonal layers connected by weak van der Waals interactions and includes covalently bound B and N. ($sp^2$ -hybridization). Hexagonal boron nitride has a variety of characteristics. It has a refractive index [91]of approximately 1.8, a bandgap of approximately 5.9 eV, and a thermal conductivity of 600 to 1000 $Wm^{-1} K^{-1}$.

In the real world, it has a wide range of uses. It's used in oxidants, acids, and solvents since it's chemically stable[92]. Because of its dielectric property, $SiO_2$ has good insulating characteristics. It has a 6-eV bandgap, making it perfect for usage in 2D electronics and graphene as an atomic flat insulating substrate or a tunneling dielectric barrier. Because of its strong covalent $sp^2$ B-N bonds, which provide excellent thermal and chemical stability, mechanical strength, and thermal conductivity, it is also used as a robust coating in hazardous situations.

### 1.2.3.1 Hexagonal Boron Nitride Structures:

In contrast to graphene, the B and N atoms in a 2D hexagonal boron nitride are organized in a honeycomb pattern using the hexagonal lattice formation rule (Figure 6). The bond length (B-N) of $sp^2$ hybridization is 1.45 Å. A strong connection is generated when one adjacent N atom joins three $sp^2$ orbits of B atoms. B-N bonds with different but similar chemical structures are linked by a strong linkage. Adjacent layers were joined by weak Van der Waals forces.

The distance between graphite layers is much bigger than the 1/3 nm spacing between h-BN layers. The intermediate layers move smoothly because to the high layer separation and variable bonding pressure inside the h-BN axis[93].

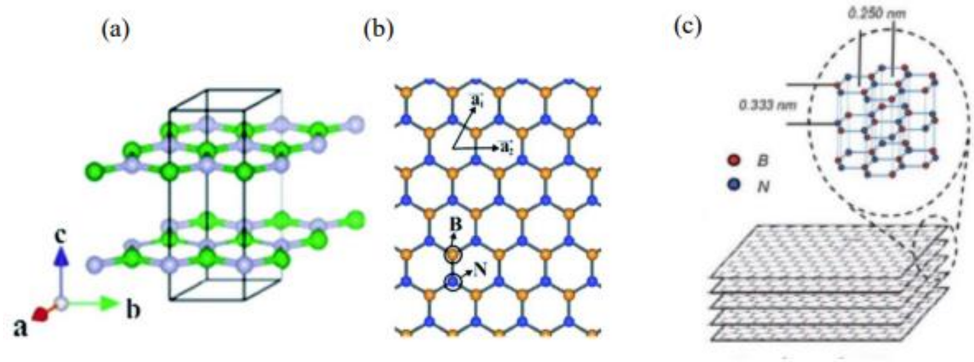

Figure 6: (a) h-BN structure (b) Stereogram (c) 2D floor layout (single layer) with a few layers of h-BN[94, 95]

### 1.2.4 Beyond Graphene and Hexagonal Boron Nitride:

Insulators, semiconductors, metals, and even superconductors (Figures 1–6) are all examples of two-dimensional electronic materials. For a long period after its discovery, graphene remained the most researched 2D material structure. Following that, other fascinating 2D materials and their properties, as well as their distinguishing qualities, were investigated. When graphene was placed atop hexagonal boron nitride (h-BN), a groundbreaking 2D material that rose to popularity swiftly[96], it was projected that it would induce a bandgap in graphene. Due to its discovery, which sparked a massive rush in research about h-BN, it has been identified as a potential substrate for devices that rely on graphene[97]. Experiments on a variety of additional semiconducting 2D layers after graphene and h-BN found that when the band structure of a subset of the 2D materials family was lowered to monolayer thickness, the band structure of a subset of the 2D materials family changed substantially. The newly established fabrication technology drew many employees in the electronic market. 2D semiconductors, particularly transition metal dichalcogenides, are being studied by many scientists (TMDs). 2D material research has exploded since the mid-2000s, as seen in Figure 8. TMDs are being researched alongside layered materials like GaSe, mono elemental 2D semiconductors [98](silicene, phosphorene, germanene), and MXenes (Figure 8).

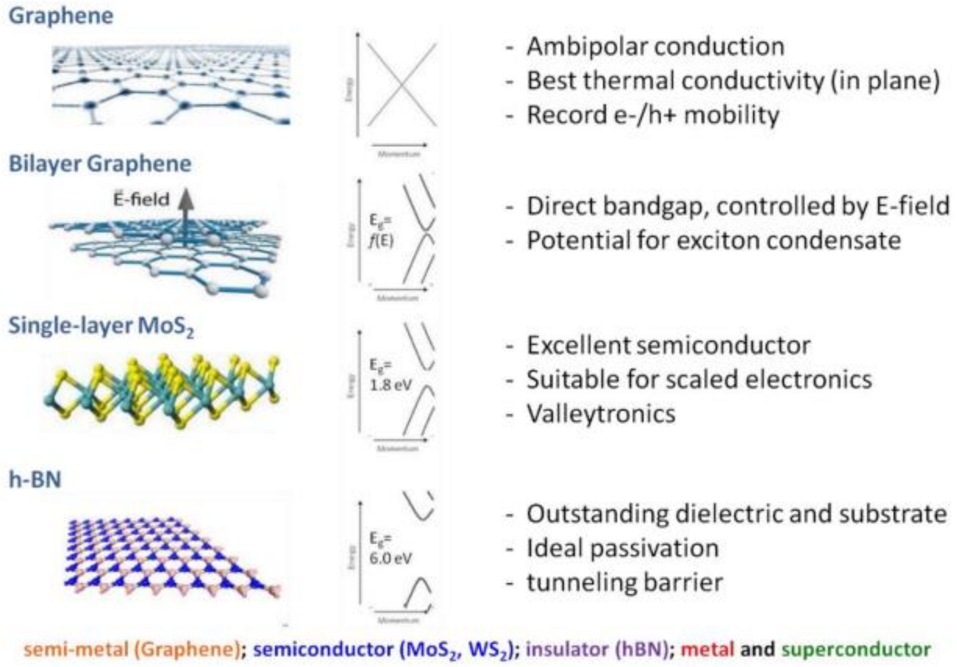

Figure 7: Two-dimensional materials showing their band structure[99]

Two-dimensional materials have a diverse material system and a wide range of characteristics, making them appropriate for a wide range of applications[100]. Semiconductors, superconductors, semimetals, and insulators are really a handful of the many types of materials that exist.

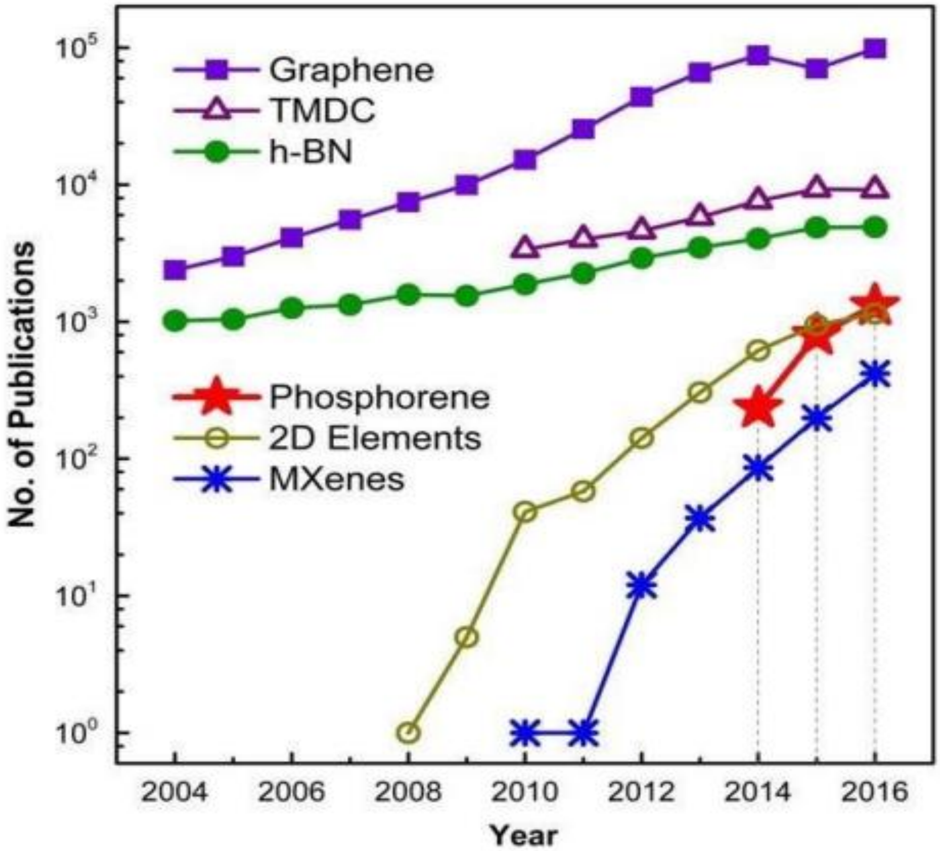

Figure 8: A ten-year comparison of the number of papers produced in the field of two-dimensional materials (the vertical axis is in log scale)[101].

As a consequence of various achievements in the optoelectronics and information technology industries, modern electronic devices continue to miniaturize and integrate, offering significant challenges to current production procedures[102]. As an outcome of two-dimensional (2D) atomically crystalline materials, new prospects for micro- and nanoscale device design and manufacture have emerged. Hexagonal boron nitride (h-BN) is a fascinating technical addition to the 2D material family, displaying a variety of unexpected properties with far-reaching implications.2D h-BN has proven to be a good platform for a wide range of applications in the current generation of 2D material research[103]. Therefore, researchers examine current achievements in h-BN applications such as optoelectronics and photonics, thermal management, batteries, and supercapacitors, as well as the potential and constraints for effective implementation in next-generation energy-efficient devices. As a result of the adoption of 2D materials, Van der Waals layered crystals have emerged as the most promising solid crystalline materials for optoelectronics. Photons and electrons may be held in planar dimensions by 2D atomically thin crystalline layers and hybrid materials, allowing nanoscale integrated circuit creation and manipulation. In comparison to conventional amorphous $SiO_2$ surfaces, the flatness of 2D h-BN crystals reduces charged traps and undulation while increasing acoustic-phonon scattering.2D h-BN crystals are also appropriate for protective coatings due to their chemical inertness and anti-permeability. At cryogenic temperatures, h-BN encapsulation can significantly increase graphene device room-temperature mobility[104], allowing for ballistic carrier propagation at length scales higher than 15 m. h-BN was used as a buffer layer as well as a mechanical transfer release layer in the production of high-quality nitride semiconductors. 2D h-BN is a flexible technology with a lot of potential for energy-efficient, compact devices. It not only helps with energy management by removing and conveying heat efficiently, but it also speeds up the development and integration of low-energy devices. Like diamond and silicon carbide, imperfect h-BN emits single photons, making it an ideal material platform for studying quantum processes and expanding photonic material potential. LEDs are one of today's most energy-efficient and ecologically beneficial lighting options[105]. For optical data storage and improved communication systems, high-throughput LEDs and laser diodes are also necessary (LDs)[106]. In the early days of LED research, red and green LEDs based on GaAs and GaP were developed and sold. Because of its high internal quantum efficiency, the Al (Ga)N family of direct-bandgap nitride semiconductors is extensively used in blue and ultraviolet LEDs (IQE)[107]. Due to reabsorption of emitted photons, Al (Ga)N materials have a poor photon extraction efficiency in the deep UV (2002–90 nm) (200-290 nm)[108]. External quantum efficiency is known to be controlled by the IQE and extraction efficiency (EE) of photons emitted from the active layer (EQE). As a result, the supply of Al (Ga)N-based LED deep-UV light sources is severely limited.

### 1.2.5 Magnesium-Diboride:

From 1911 until 1973, when superconductivity was discovered, the highest known transition temperature[109] (Tc) increased at a modest average rate of 0.3 K per year, from 4 K in Hg to 23 K in $Nb_3Ge$[110]. The microscopic underpinnings of superconductivity, based on electron–phonon interactions and explained by the immensely powerful BCS theory[111], were well known at the time. In the early 1980s, it was commonly anticipated that this matching strategy would not result in a significant increase in Tc. The discovery of superconductivity in $MgB_2$, a typical binary molecule, came as a pleasant surprise in 2001, at a time when science had mostly settled down[112]. $MgB_2$ was discovered to be more comparable to low $T_c$ superconductors (LTS) than oxide superconductors (then called as high temperature SCs or High Temperature Superconductors) (HTS). The finding of a substantial boron (B) isotope effect demonstrated[113] that $MgB_2$ superconductivity is phonon-mediated, and comprehensive experimental evidence supported the s-wave symmetry of the order parameter. On the other hand, directly contradicted the widely held opinion that $Nb_3Ge$'s Tc represented the upper limit for this process, revealing $MgB_2$'s uniqueness and requiring us to reconsider some of our earlier assumptions. Although $MgB_2$ was discovered[114] in the 1950s, it was not investigated or utilized as a conventional superconductor until 2001. $MgB_2$ has the highest critical temperature of any known intermetallic compound[115], with a temperature of 39 Kelvin. In this chapter, we'll look at the crystal structure of $MgB_2$, the origins of superconductivity, and manufacturing procedures. This section will discuss what distinguishes this superconductor from others.

### 1.2.5.1 Crystal and Electronic Structure of $MgB_2$:

$MgB_2$ outperforms other conventional superconductors in terms of critical temperature (Nb, for example)[116]. The transition temperature of 39K is three times lower than the transition temperature of mercury-based high-Tc superconducting cuprates, which is (130K)[117]. At liquid nitrogen temperatures, copper oxide with a high Tc has also been demonstrated to operate. Because of manufacturing issues and the substantial residual resistance generated by the weak link effect, these unconventional superconductors are only appropriate for SRF holes. Let's start with the crystal and electrical structures[118] of $MgB_2$, then go on to the intriguing features that make it a candidate superconductor material.

## 1.3. SYNTHESIS OF TWO DIMENTINAL MATERIALS:

### 1.3.1. Transition Metal Dichalcogenide Synthesis:

The layered structure of the transition metal dichalcogenides is comparable to that of graphene. It should also be added that a monolayer of TMD is usually a layer of transition metal atoms between two chalcogenide layers[119]. Aside from this peculiarity, monolayer TMDs are produced in the same manner as graphene. Only five of the 44 monolayer TMDs that have been theoretically described appear to be unstable[119]. Currently, novel monolayers like as $MoS_2$, $WS_2$, $MoSe_2$, and $WSe_2$ are being synthesized; there are yet more to be synthesized—for several reasons, more TMD minelayers have yet to be identified experimentally.

Several TMDs exhibit stable crystal structures, according to theoretical simulations. Several TMDs have not been synthesized due to the difficulty of developing a synthesis process[120]. It may take numerous attempts to achieve a single synthesis if a TMD lacks a well-developed formula. Chemical vapor deposition[121], as well as elements like sufficient volume flow rates, precursor components, temperature levels, and pressure, may all affect the result of a recipe. Even though a formula is well-established, variations in equipment, such as heat loss due to insulation, might cause issues in the material synthesizing process.

#### 1.3.1.1 Chemical Vapor Deposition of TMDs:

One of the most fundamental ways for manufacturing monolayer TMDs on a regular basis is chemical vapor deposition (CVD)[122].

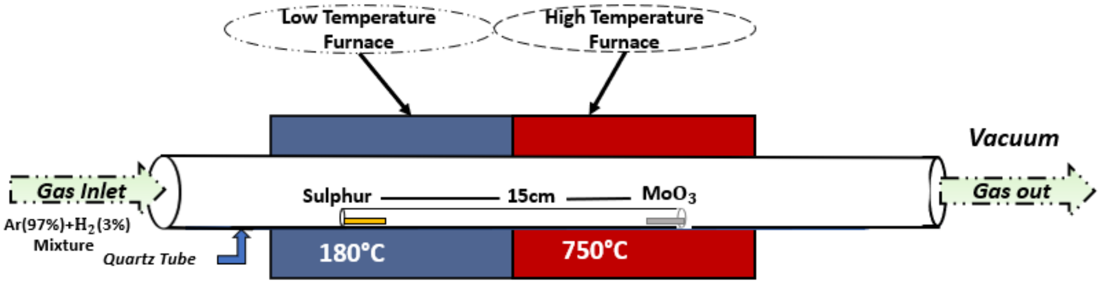

Figure 9: Schematic diagram of a CVD reactor used for TMD growth

Quartz tube furnaces, rate of volume flow concerns, a pressure sensor, and a vacuum system are all part of this system. In most situations, a quartz tube furnace has a single and multi-zone heating stage (as illustrated in Figure 9).

Compared to mechanical exfoliation, CVD provides several advantages[123]. The capacity to make large-scale monolayer films is a key utility of CVD[124]. These films have a uniform thickness due to the controlled growth parameter. Once a formula is created, it may be used to generate monolayers indefinitely. The recipe formulation, on the other hand, can be a little challenging since CVD scans more than ten factors at simultaneously, all of which might impact monolayer formation. It is worth mentioning that the method by which the substrate is prepared has a considerable impact on growth. "Inadequate substrate cleaning impacts material production and deforms the layers," said Arend M. van der Zande et al. The mismatch between the substrate lattice and TMD might adversely impair the monolayer formation process[125]. In addition, as the temperature rises, the substrate options may become more limited.

### 1.3.1.2 Exfoliation Utilizing Liquid Mechanical Method of TMDs:

In the fabrication of monolayer TMDs, many forms of liquid mechanical exfoliation (LME) have been utilized[126]. Lithium ions can be intercalated into the crystal lattice of TMDs to reduce inter-layer contact in bulk material[127]. This is accomplished using lithium-ion, which widens the interlayer gap between successive layers and diminishes the van der Waal forces. After expanding the space between the 26 layers with lithium, the material is submerged in a solvent[128]. As a liquid solvent, deionized water is used to add lithium. The equation $2Li(s) + 2H_2O(l)\ 2LiOH(aq) + H_2\ (g)$ describes the interaction between lithium and water[129]. The formation of lithium hydroxide bubbles aids in the consumption of any lithium present in the material, as well as the exfoliation process, due to the visible lattice expansion caused by the lithium hydroxide bubbles. Long lengths of time, up to 15 hours, are commonly spent sonicating the solvent material mixture. Various ultrasonic frequencies and temperature fluctuations can affect the number of layers of resulting slurry. After the sonication process, the sample is centrifuged, and the material is separated according to the number of layers it contains. The final step of LME is to inject the slurry onto the target substrate. LME has the added benefit of being able to work with a wide range of substrates[130]. Because of the flake restacking, LME has less control over the number of layers, which is a hindrance. Spin coating can aid in improving the layering number consistency in samples. Another challenge is that LME settings make regulating the exact monolayer impossible. Instead of a fixed number of layers, a range of layering numbers is constructed using a set of LME parameters[131].

### 1.3.2 Synthesis of graphene:

Graphene may be made in a variety of ways, with the process employed having an influence on the graphene's quality[132]. Graphene is now manufactured in a variety of forms and quality using a variety of processes. The discovery in the 1970s that carbon can solidify as a thin graphite covered layer on transition metal surfaces sparked the development of this material[133]. However, the procedures are not entirely applicable in a large-scale industrial environment.

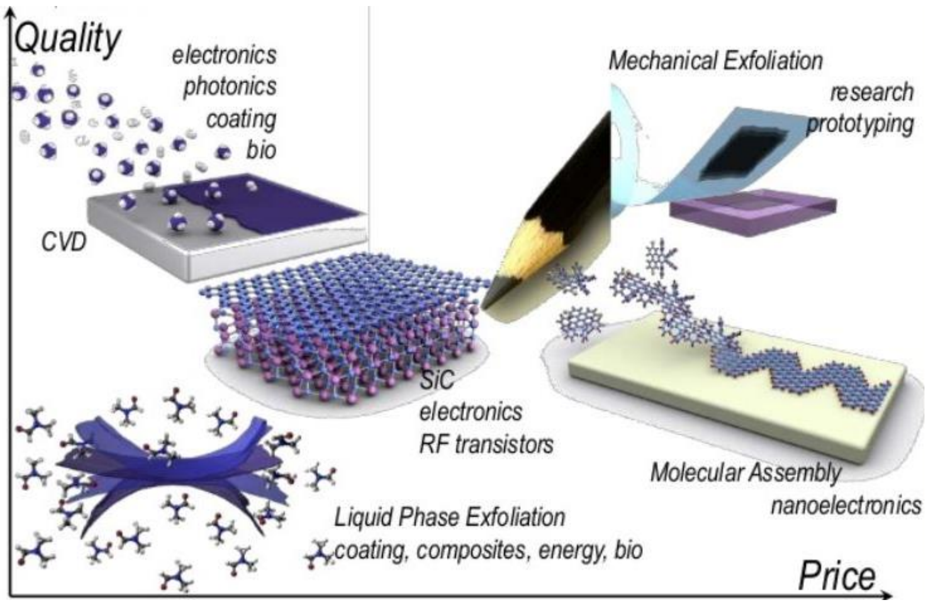

Figure 10: Comparison of the cost and quality of graphene manufactured mostly using conventional methods. (*Manufacturing high-quality graphene in high volumes has been an obstacle. SOURCE: University of Manchester*)[134].

### 1.3.2.1 Mechanical Exfoliation of Graphene:

Previously, this process has been used to create single layers of high-quality graphene flakes on a variety of substrates[135]. During mechanical exfoliation, a nanotechnology process, a transverse force is applied to the surface of layered structure materials[136]. The method's appropriateness is since weak van der Waals forces hold unpacked layers of highly ordered pyrolytic graphite (HOPG) together[137]. Furthermore, the inner layer distance is 3.34, and their bond energy[138] is 2 eV/nm$^2$. To extract single layers of graphene from graphite[139], an external force of roughly 300 nN/µm$^2$is required, which may be contained using adhesive tapes. Go-betweens like scotch tape, ultrasonication[140], and an electric field, as well as a transfer printing procedure[141], are used to remove graphene that has collected on the sticky tape. Graphene is substantially pressed onto $SiO_2/SiO_2$ after effective detaching off procedures (Figure 11). Mechanical exfoliation is a straightforward procedure that can be performed using common instruments[142], which motivates scientists to immediately implement it. Outside of a large-scale industrial environment, however, it is inapplicable. This method, on the other hand, creates graphene flakes which might be examined using optical microscopy, Raman spectroscopy, and AFM. They're also rather tiny, with micro-meter-wide width margins[143].

Figure 11: A schematic depicting the stages involved in exfoliating graphene layers with scotch tape.

#### 1.3.2.2. Liquid Phase Exfoliation of Graphene:

A solvent with a surface tension (γ) of around 40 mJm-2, as well as an increase in the total area of graphite crystallites[144], is needed to separate graphene from graphite layers[145]. N-methyl-2-pyrrolidone (NMP), ortho-dichlorobenzene (ODCB)[146], and dimethylformamide are three of the most often used solvents (DMF)[147]. For this kind of separation, sonication is utilized. Graphene of varied sizes and thicknesses is created using an ultrasonic process. Centrifugation is used to remove the unexfoliated components from the graphene sheets.

Researchers used this approach to create liquid graphene and remove chemical vapor deposition samples recently[148]. This has made it possible to process more data for practical reasons. For use on a variety of surfaces, graphene dispersion in spray, inkjet, or spin coating forms is available[149]. Graphene flakes films as transparent conductors or sensors, graphene dispersions as optical limiters, and peeled off graphene as mechanical reinforcement for polymer-based composites are only some of the applications for this technology[150].

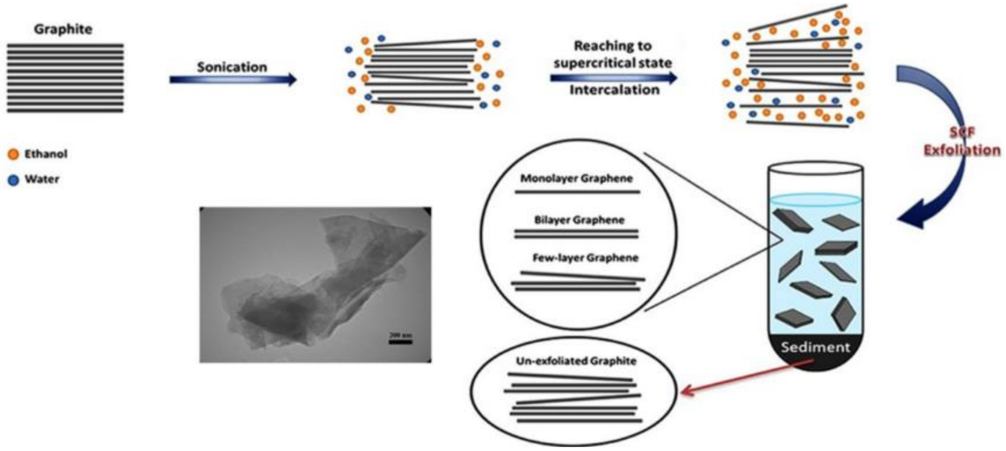

Figure 12: Schematic illustration of the Liquid phase exfoliation process (Optimization of graphene production by exfoliation of graphite in supercritical ethanol: A response surface methodology approach)[151].

### 1.3.2.3 Wet Chemical Synthesis of Graphene:

A low-cost way of producing graphene is to convert graphite into graphene oxide sheets on a large scale. Hummers' approach[152] oxidizes graphite to create graphene oxide using oxidants such as nitric acid, sulfuric acid, and potassium permanganate[153]. Since they include $sp^3$ hybridized atoms, the graphene oxide sheets must be reduced. In the reduction process, several different strategies are applied. One of these is thermal treatment, which involves heating oxide functional groups to eliminate them. Reducers such as hydrazine, sodium borohydride, hydroquinone, and ascorbic acid are also used to remove oxygen atoms from graphite sheets, making them less hydrophilic. Particularly when functionalization groups such oxygen, hydroxyl, and epoxy are not removed during the chemical reduction process. However, due to the obvious procedure's limitations, further study is required to enhance it[154].

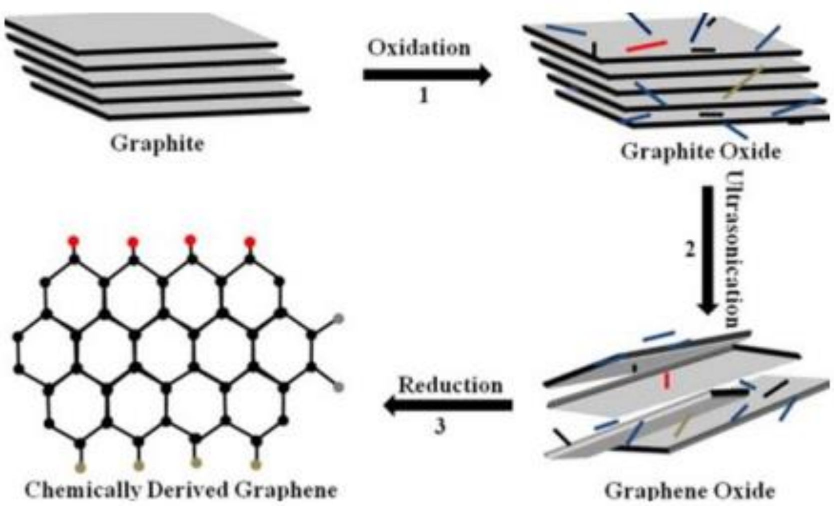

Figure 13: Schematic representation of the chemical technique used to produce graphene.

Graphene, which is employed in a variety of applications including paper-like materials, polymer composites, energy storage materials, and transparent conductive electrodes, is created using this approach[155].

Other methods of manufacturing graphene are not considered in this study. However, research suggests that before they can be used in industrial settings, they will need to be cost-effective and have a large-scale applicability modification. Electron beams are employed to irradiate PMMA nanofibers, graphite is arc discharged, PAHs are thermally fused, and nondiamond is transformed[156].

### 1.3.2.4. Epitaxial Growth of Graphene on Silicon Carbides:

On a single crystalline silicon carbide, epitaxial thermal growth is used ($SiC_2$)[157]. $SiC_2$ has two distinct terminations: the Si face, which corresponds to the (0001) polar surface, and the C face, which corresponds to the (0002) polar surface (0001). The same physical process drives graphene formation at both ends: Si sublimation at various temperatures at a far faster rate than C due to its higher vapor pressure[158], hence this is the most frequently utilized approach. A graphene layer develops on the surface with the leftover C. Surface reconstructions and growth kinetics for Si and C faces depend on graphene growth rates, morphologies, and electrical characteristics. The approach offers several benefits, including the ability to regulate the size of the graphene generated on the substrate and the lack of a transfer during device manufacturing.

On the other hand, the method's weaknesses are clear. The graphene produced, for example, is more brittle than that produced during exfoliation. This is since SiC, and graphene are not the same thing. It's also expensive since it requires extremely high temperatures[159], on top of the high cost of SiC.

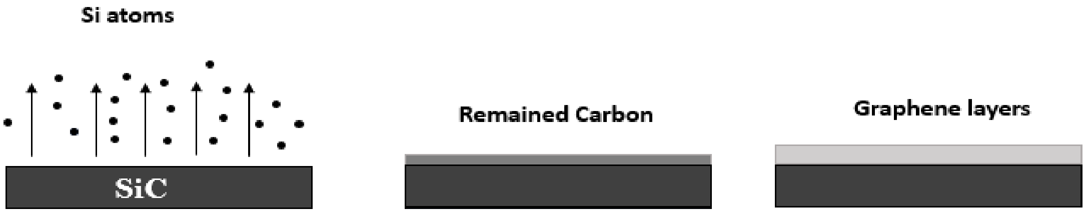

Figure 14: Growth model of epitaxial graphene on SiC (0001) by thermal decomposition in argon and its etching in oxygen atmosphere

### 1.3.3 Hexagonal Boron Nitride Synthesis:

Boron nitride has been successfully manufactured utilizing a variety of techniques. For large-scale manufacturing of h-BN, CVD is the best option[160]. Exfoliation in the mechanical and liquid phases are two additional techniques. Because it is dependent on the breakdown of antecedents, CVD may also be regulated.

Boron Nitride Nanosheets (BNNS) can be made in two ways[161]: (a) from the bottom up using chemical vapor deposition and other deposition techniques, or (b) from the top down using peeling techniques. The most often utilized techniques (a) and (b) include pulsed laser deposition, chemical vapor deposition, exfoliation, and mechanical exfoliation, respectively (c). Large quantities of BNNS can be difficult to create due to exfoliation operations, even though they are normally crystalline (see method description below).

#### 1.3.3.1 Exfoliation by Mechanical Methods of Hexagonal Boron Nitride:

Based on the sticky tape graphene production process, this is the most simple and efficient solution. Small monolayers of h-BN, measuring only a few microns, have been isolated from h-BN powder. For layers thicker than 100 microns, synthetic highly oriented pyrolytic boron nitride (HOPBN)[162] or mechanical cleavage are employed. Another method of mechanical exfoliation of nanosheets used by Li et al. was totally controlled low energy ball milling. The method was utilized to produce many high-quality h-BN nanosheets while minimizing their downsides.

#### 1.3.3.2 Exfoliation In liquid Phase of Hexagonal Boron Nitride:

In this process, solvents are employed to make hexagonal boron nitride. Exfoliation and scattering are done with 1,2-dichloroethane, dimethylformamide

(DMF)[163], and water. Several solution methods must be completed to produce considerable volumes of h-BN. By matching the surface energy of the solvent to that of h-BN, the solvent is selected to counteract van der Waals forces between layers[164]. The optimal choice is a solvent that can minimize exfoliation energy, diminish van der Waals forces between layers, and offer a perfectly defined dispersion where the Hansen solubility parameter theory may establish polar hydrogen bonding and cohesive energy density. This technique has several limitations. Although the number of single layers created is limited, layer management is difficult. The nearby area's comparably modest size is also a disadvantage.

#### 1.3.3.3 Chemical Vapor Deposition (CVD) of Hexagonal Boron Nitride:

Because it is more practical for large-scale synthesis of monolayer h-BN than the other approaches, this method is presently the most widely used. In 1995, the Oshima group reported that monolayer h-BN was epitaxially formed on Ni (111), Pd (111), and Pt (111) using low-pressure CVD (LPCVD) and atmospheric pressure CVD (APCVD)[165] with a variety of precursors including borazine[166], ammonia borane, and diborane with ammonia at a high temperature of around 1000 °C. Despite the need for transfer methods, h-BN has been created using standard substrates such as Pt, Cu, and Ni. h-BN has been discovered to grow directly on $SiO_2$/Si at high temperatures (1000 °C)[167].

#### 1.3.3.4 Physical Vapor Deposition (PVD) of Hexagonal Boron Nitride:

The previously unclear relationship between increased information and the CVD process has vanished. On the Ru (0001) substrate, B and N atoms form a conventional h-BN layer[168]. Another method uses a similar strategy to make an h-BN movie on an Au (111) substrate with a 60-degree rotation angle between the h-BN domain names of the required triangles.

#### 1.3.3.5 Pulsed Laser Deposition (PLD) of Hexagonal Boron Nitride:

The temperature rise was reduced using this approach to obtain good stoichiometric h-BN[169]. Glavin et al. Used Glavin et al. An approach to produce highly crystalline h-BN in the amorphous state[170] at 700 °C. Terry et al. It was also possible to form multiple h-BN monolayers on $SiTiO_3$ substrates using Ag films as buffer layers. Compared to liquid and CVD exfoliation, this approach has less crystalline h-BN.

The field of hexagonal boron nitride research is continually developing, and attempts are presently being made to improve large-scale and efficient synthesis procedures.

## 1.4. Modification of Surfaces and Edges of Two-Dimensional Materials:

### 1.4.1 TMD and Graphene Modifications:

The more developed a 2D material, the more its intrinsic qualities change. To influence semiconductor characteristics, heterostructures, doping, and surface functionalization have all been used[171]. It is critical to have a solid grasp of the characteristics of 2D materials in modern electronics. A metal-insulator transition was discovered by functionalizing graphene with nitrogen in an RF plasma[172]. Even though graphene heterostructures have been developed to take use of its long-range transport and massless Dirac fermions, the dilemma of how to overcome its zero bandgap remains unanswered. It was only natural for graphene to be tinkered with in attempt to overcome its limits and improve its qualities.

### 1.4.2 Functionalization of the Surface/Edge:

Even though dangling bonds and lone pairs of electrons may be quickly absorbed, gas molecules commonly interact with 2D systems. Functionalization is the process of linking components to a 2D system via surface / edge connections. The atoms do not need to be integrated into the sample's crystal structure during this procedure. Functionalization can be improved by employing lasers, according to Li et al. It has been established that the physical absorption of $NH_3$ on the surface of $WS_2$ nano-flakes may be used to detect gas[173]. Aside from being easy, functionalization serves another vital purpose: when several atoms are coupled to 2D systems, many features of the structure can change. Bandgap engineering might be used to design new optical devices[174]. Commercial devices with surface functionalization, such as photodetectors and gas sensors, might be the next big thing in optoelectronics[175].

### 1.4.3 Doping of Two-Dimensional Materials:

The technique of inserting a small number of atoms into the lattice of another material is known as doping[176]. Between doping and alloying, there is just one change in material concentration[177]. Dopant atoms can increase the number of electrons in a 2D material, but in an alloyed system, all the elements have the same concentration. Active sites can be located between the atoms' margins in a $MoS_2$ layered structure[178]. After bond formation, the system still gets an electron contribution from a dopant known as an n-type dopant or donor. The energy levels of dopant electrons are usually near to the CBM of parent systems[179]. The energy required to excite the provided electrons into the CBM, where they may freely participate in the 2D system's conduction, can be supplied by finite temperatures. P-type (acceptors) dopant atoms, on the other hand, contain less electrons and feed holes into the VBM of the system. The extra charge carriers boost the conductivity rate of the 2D system[180]. When more dopants are introduced, the Fermi level of the initial system moves toward the site of the dopant atoms. TMDs doped with potassium at the drain/source contacts of a FET give reduced contact resistance, according to one study[181]. For doping 2D materials, several approaches have been devised. By carefully manipulating the precursor material in CVD, graphene has been shown to be capable of being doped with nitrogen[182]. Plasma-assisted CVD and chemisorption have comparable properties. To introduce atoms into the system's lattice, the energy of dopant atoms can be enhanced. Because plasma-assisted doping may cover large portions of a sample, it is beneficial. In contrast, plasma procedures have the potential to induce defects in the sample[183].

Substitutional doping happens when a dopant atom is introduced into a system and takes over a lattice position that would have been occupied by an atom from the original system[184]. Interstitial space is the space between the lattice sites of a crystalline material that can be filled by a dopant atom. P-type dopants at isolated electron pairs in the host system can create magnetic moments[185].

# CHAPTER 02

# CHEMICAL VAPOR DEPOSITION (CVD) AND PLASMA ENHANCED CHEMICAL VAPOR DEPOSITION (PECVD) SYNTHESIS OF 2D MATERIALS AND CHARACTERIZATION

## 2.1 Introduction:

As we mentioned in Chapter 01, building 2D material systems may be done in a variety of ways. To construct the desired 2D material, several factors must be modified, including temperature, pressure, and gas flow[186]. Growth and characterization of 2D materials have been addressed for single layer films[187]. Even though monolayers have a diverse set of properties, it is important to subject prepared materials to controlled surface engineering to elicit new and fascinating characteristics. Heterostructures are one of the most direct ways to do this[188]. TMDs Graphene, h-BN, and $MgB_2$ have been identified in both in-plane and stacked heterostructures[189]. Due to several synthesis issues, in-plane heterostructures have advanced more slowly than stacked heterostructures. High control and reproducibility are critical in large-scale device manufacturing[190]. Prior methods lacked control since they relied heavily on CVD processes for synthesis. By utilizing and combining thermal evaporation/conversion and PECVD, we developed a novel method for generating h-BN/graphene of single and double quantum barrier and h-BN/ $MgB_2$ heterostructures with great control.

## 2.2 Plasma Enhanced Chemical Vapor Deposition (PECVD):

To produce carbon-based chemicals, PECVD is a prominent method. A thin-film coating that converts gas to solid on a substrate is known as PECVD[191]. This approach offers a few benefits, including a typically clean working environment and optimal operating temperatures[192]. It requires a high level of growth selectivity as well as control over the pattern that Nanostructures create. When employing the PECVD technology to manufacture direct graphene and h-BN on insulating surfaces like $SiO_2/Si$, quality degradation and additional faults caused by the transfer process are avoided[193]. From a single hydrogen hydrocarbon fuel, plasma is made up of molecules, ions, and a variety of radicals. The utilization of plasma in this scenario generates an environment that allows for a quicker growth rate and lower deposition temperature than thermal CVD. CVD-produced graphene is still of higher quality than PECVD-produced graphene.

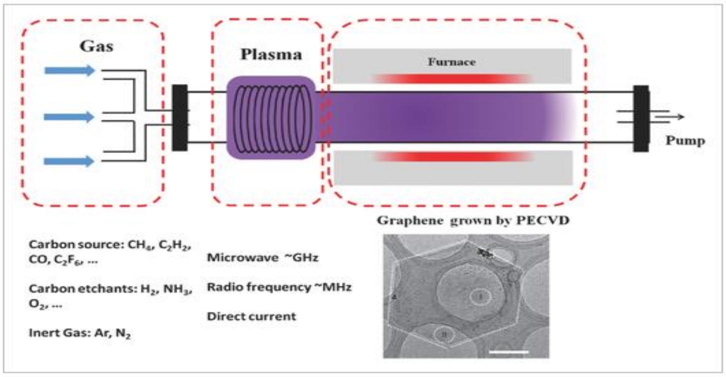

Figure 15: Schematic diagram of the Graphene synthesis technique involving plasma and $CH_4/H_2$ decomposition. (Controllable Synthesis of Graphene by Plasma-Enhanced Chemical Vapor Deposition and Its Related Applications)

The graphene creation process is depicted[15] in Figure 15, which comprises mixed plasmas of methane and hydrogen, as well as CHx radicals formed following methane breakdown[194]. Through metastable carbon atoms and molecules, the CHx radicals reattach after a certain distance to create an $SP^2$ structure on a substrate. An appropriate carbon source must be identified, and the amount of carbon in the feedstock combination of gases must be managed, to promote high-quality growth. The transfer of a huge amount of gas is required for big-scale graphene synthesis. The bulk of PECVD procedures, on the other hand, are carried out at low pressure to ensure that electrons have a lengthy mean free path. Even though reactor layouts differed, a variety of plasma sources, including microwave plasma, DC discharges, and radiofrequency plasma, were successfully examined for graphene production in the PECVD process[195].

## 2.3 Electrical Properties of Materials:

### 2.3.1 The Electrical Conductivity:

Based on their electrical properties, materials are classified as conductors, semiconductors, or insulators[196]. Superconductors are now included in this category. It's critical to understand two ideas when working with new materials: how electrons react to electrical forces and how atoms react to mechanical forces[197]. The first is electrical conductivity, or the ease with which charge travels through it. Charge is carried by electrons, ions, charged holes, or a combination of these. A current of magnitude I flows when an electric potential V is applied across a material[198]. Therefore, the current I in most conductors is proportional to V, according to Ohm's Law:

$$V = RI$$

where R represents electrical resistance, which is determined by the material's intrinsic qualities(ρ) as well as the shape (length l and cross-sectional area A of the current).

$$R = \frac{\rho l}{A}$$

The inverse of resistivity is electrical conductivity[199] (a substance's capacity to transport an electric current): $\sigma = 1/(\rho)$ (Since the material's electric field intensity is E = V/L, Ohm's Law may be stated in terms of current density J = I/A as follows:

$$J = \sigma E$$

Another way to write it is $J = nqv_d$, where n is the charge carrier density and q is the electron charge. The drift velocity $v_d$ is the rate at which changes propagate in the applied field's direction. When a material has less dispersion, charge carriers can travel further with the same electric field. This is referred to as the mobility ratio[200], $\mu = v_d/E$. As a result, a material's mobility may be utilized to determine its conductivity: $\sigma = nq\mu$

According to the equation, the electrical conductivity of a material may be changed by manipulating the number of charge carriers, n, or managing the mobility of the carriers[201]. Electrical conductivity varies by more than 27 orders of magnitude between materials, the greatest variety of any physical property[202].

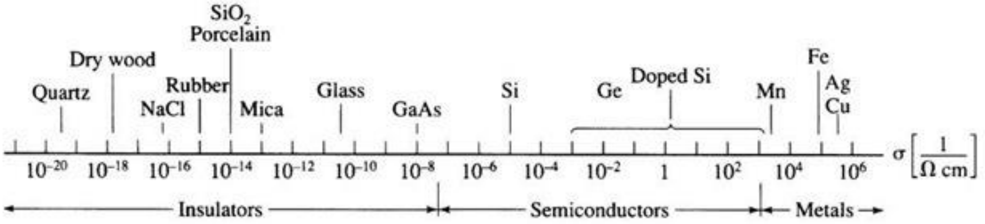

Figure 16: The conductivity of various materials at room temperature. The impact of temperature and purity on semiconductor conductivity is significant[203]**.**

### 2.3.2 Four Probe Resistivity for Sheet Resistance

The sheet resistance's concept is utilized to describe both wafers as thin doped layers since it is often simpler to measure sheet resistance rather than material resistivity[204]. The ratio of a layer's resistivity, ρ, and thickness, t, determines its sheet resistance.:

$$R_s = \frac{\rho}{t}$$

It's worth mentioning that sheet resistance is measured in ohms as well, and it's usually represented as $\Omega sq^{-1}$ (ohms per square) to distinguish it from resistance. The origin of this unique unit name may be traced back to the fact that a square sheet with a sheet resistance of $1\,\Omega sq^{-1}$ has the same resistance regardless of size. As a result, the resistance of a rectangular rod with length l and cross section $A = wt$ may be expressed as $R = \rho l/A$, which immediately simplifies to $R = Rs$ for the specific example of a square lamella with sides $l = w$ (see Figure 17).

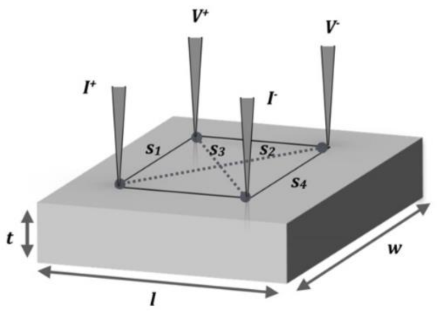

Figure 17: A schematic of a square 4-probe resistance measurement

For analyzing very thin films, the square form is recommended over a straight line since it takes up less space (maximum probe spacing is roughly $\sqrt{2}s$ against 3s for the collinear arrangement) and has somewhat higher sensitivity. The infinite 3D and 2D systems with both in-line and square configurations of four probes[205] were summarized in Table 1.

| Sample shape | 4P in-line | 4P square |
|---|---|---|
| 3D bulk | $2\pi s\frac{V}{I}$ | $\frac{2\pi s}{2-\sqrt{2}}\frac{V}{I}$ |
| 2D sheet | $\frac{\pi}{ln2}\frac{V}{I}$ | $\frac{2\pi}{ln2}\frac{V}{I}$ |
| 1D wire | $\frac{\Sigma}{s}\frac{V}{I}$ | – |

Table 1:Sheet resistance $R_{sh}$ or bulk resistivity   with four probes laid out linearly and squarely for a semi-infinite 3D substance, infinite 2D sheet, and 1D wire.

### 2.3.3 Thermoelectric Power

In solids, an electron is a negative-charged elementary particle that conducts electric current[206]. Because so many electrons in solids are in thermal equilibrium, they also transfer heat and entropy. As a result, when there is a temperature differential, they can flow from one side to the other, producing an electric current. This implies a connection between heat and electrical processes, known as thermoelectric effects[207], which include the Seebeck and Peltier effects. The Seebeck effect is a phenomenon in which voltage V increases according to the applied temperature gradient T, represented as

$$V = S\Delta T \tag{5}$$

The Seebeck coefficient, commonly known as thermoelectric power or thermopower[208], is denoted by the symbol S.

A number of techniques, including pulse [209]and ac [210], can be used to assess thermoelectrical power. We presented a simple and low-cost method for getting thermopower in the 4 K to 700 K range using ordinary thermocouple devices.

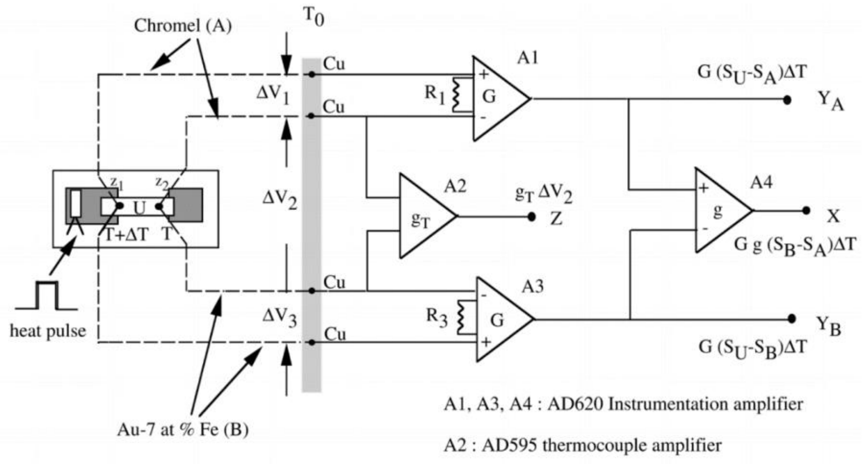

Figure 18: The schematic of the circuit diagram[211] used for thermopower measurement.

Figure 18. $\Delta V_1$, $\Delta V_2$, and $\Delta V_3$are the three thermoelectrical voltages that define the sample's absolute thermoelectrical power, $S_U$, and average sample temperature, $T$ [211]. The voltage difference $\Delta V$ generated between sites $z_1$ and $z_2$ in a homogeneous material with a temperature profile $T(z)$ is computed using the thermoelectrical power S definition can be given by:

$$\Delta V = V(z_2) - V(z_1) = \int_{z_1}^{z_2} S \frac{dT}{dz} dz \tag{6}$$

The voltages at $z_1$ and $z_2$ are denoted by $V(z_1)$ and $V(z_2)$. As a result, the voltages in Figure 18 can be expressed as follows:

$$\Delta V_1 = \int_{T_0}^{T} S_A \, dT + \int_{T}^{T+\Delta T} S_U \, dT + \int_{T+\Delta T}^{T_0} S_A \, dT$$

$$= \int_{T}^{T+\Delta T} (S_U - S_A) dT = (S_U - S_A)\Delta T \tag{7}$$

$$\Delta V_2 = \int_{T_0}^{T} S_A \, dT + \int_{T}^{T_0} S_B \, dT$$

$$= \int_{T}^{T_0} (S_B - S_A) dT = V_{BA}(T) \tag{8}$$

$$\Delta V_3 = \int_{T_0}^{T} S_B \, dT + \int_{T}^{T+\Delta T} S_U \, dT + \int_{T+\Delta T}^{T_0} S_B \, dT$$

$$= \int_{T}^{T+\Delta T} (S_U - S_B) dT = (S_U - S_B)\Delta T \tag{9}$$

The thermocouple wire materials (A and B) or the sample are denoted by subscripts in equations (7)-(9). (U). The thermocouple junctions A and B, which incorporate copper leads and transfer signals from the reservoir to the instrumentation amplifiers, have a temperature of $T_0$. This approach may be used to determine the thermopower of a wide range of materials, including graphene sheets, across a broad temperature range[212].

## 2.3 Sample Holder Design:

The holders were machined by the physics department's machine shop at the University of Louisville. All three holders were designed for the deposition of graphene, h-BN (PECVD), and $MgB_2$ (HPCVD).

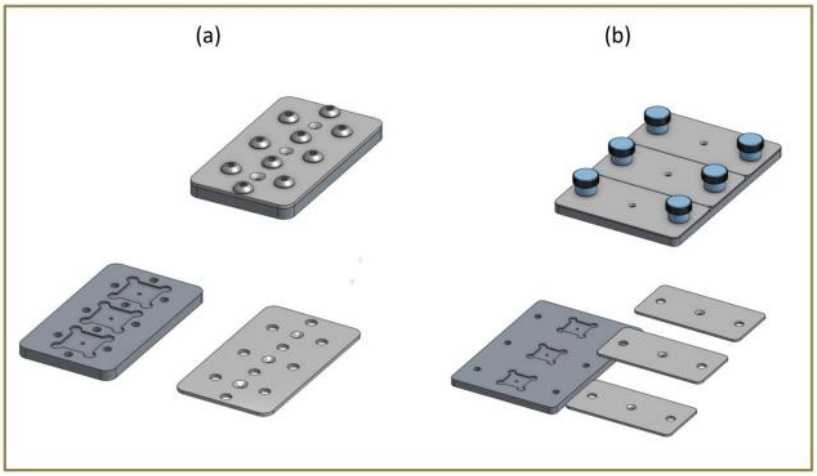

Figure 19: Sample holders utilized to stabilize the substrate during (a) the graphene h-BN deposition and (b) the $MgB_2$ deposition processes.

The sample holders had to fit inside the quartz reactor within the tube furnace, hence the dimensions of the holders were chosen accordingly. All sample holders were made of stainless steel to endure high temperatures.

## 2.4 Characterization of 2D Materials:

### 2.4.1 Raman Spectroscopy

Figure 20: A diagram displaying the Renishaw invia Raman spectroscopy setup.

For smooth monochromatic scattering of the laser source, Raman spectroscopy is an inelastic spectroscopy, whereas Rayleigh scattering is an elastic spectroscopy[213]. When laser photons strike the pattern, dispersion inelasticity causes the frequency shift. Raman scattering absorbs and re-emits them at higher or lower frequencies depending on the true monochromatic frequency. To scatter Raman and Rayleigh light, molecules must move from their lowest level to a digital state. The artwork of Jablonski is ideal for depicting the power transfer between Rayleigh and Raman (Fig. 20).

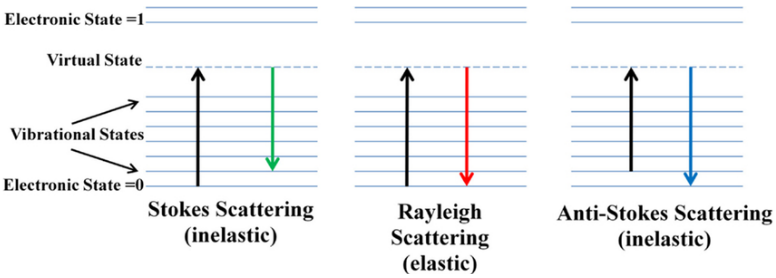

Figure 21: Schematic diagram depicting Rayleigh and Raman scattering events[214]

By allowing a molecule to create either a stoke or an anti-stoke in contrast to an incoming photon, Raman scattering adds a new dimension to the equation. Molecules are found in their ground state at room temperature. As a result, the chances of having a stoke outnumber the possibilities of obtaining an anti-stoke. In a Raman spectrum, the Raman shift, sometimes called the frequency differential (delta, v), offers information on rotational, vibrational, and other transition frequencies. The abscissa of the Raman spectrum can be used to illustrate a Raman shift.

There are a variety of applications for Raman spectroscopy[215]. It is used to follow the molecular structure and crystallinity of solid, liquid, and gaseous substances, as well as to look for polymorphs and compounds that have never been observed before[216]. It's also used to educate how to compute the residual stress factor and how to keep track of molecular orientation.

The most effective tool for studying two-dimensional (2D) materials and graphene is Raman spectroscopy. It is used to determine the density of defects, the deformation, and the number of layers in the structure[217]. It has been used to study how electrons and photons behave in graphene. Laser activation changes the energy of graphene. As a result, Raman spectroscopy has two main peaks. The most prominent vibrational mode in the planar vibrational mode of graphene composed of $sp^2$-hybrid carbon atoms is 1580 $cm^{-1}$. A two-photon oscillation process produces the grating`s second peak, 2D. (2690 $cm^{-1}$). The D (1350 $cm^{-1}$) band is frequently used to denote a defective or disorganized band. It`s a breathable ring on a $sp^2$ carbon ring meant to be worn near a graphene defect or edge. The last band is defective due to crystal symmetry and cannot be observed in high-quality graphene (See Fig. 22(a)).

The G band changes to lower frequencies as the number of layers in a graphene sample increases[218]. This is due to the G band's sensitivity to strain effects while also revealing the amount of graphene layers. Because the G band position is vulnerable to doping, it may be utilized to determine drug doping levels. Doping levels are determined by the line width and frequency of the end of a G band. In graphene, on the other hand, a 2D band may be used to distinguish between single and multiple layers of fewer than four layers (Figure 22 (c)). The distinction is defined by the band's location as well as its form. Alternatively, the band layers of defect free single graphene layers might be recognized utilizing both 2D and G bands. The absence of a D band and a crisp symmetric 2D prove the defect-free, distinct layers of graphene. A thorough examination of the peak intensities of the G and 2D bands confirms this[219].

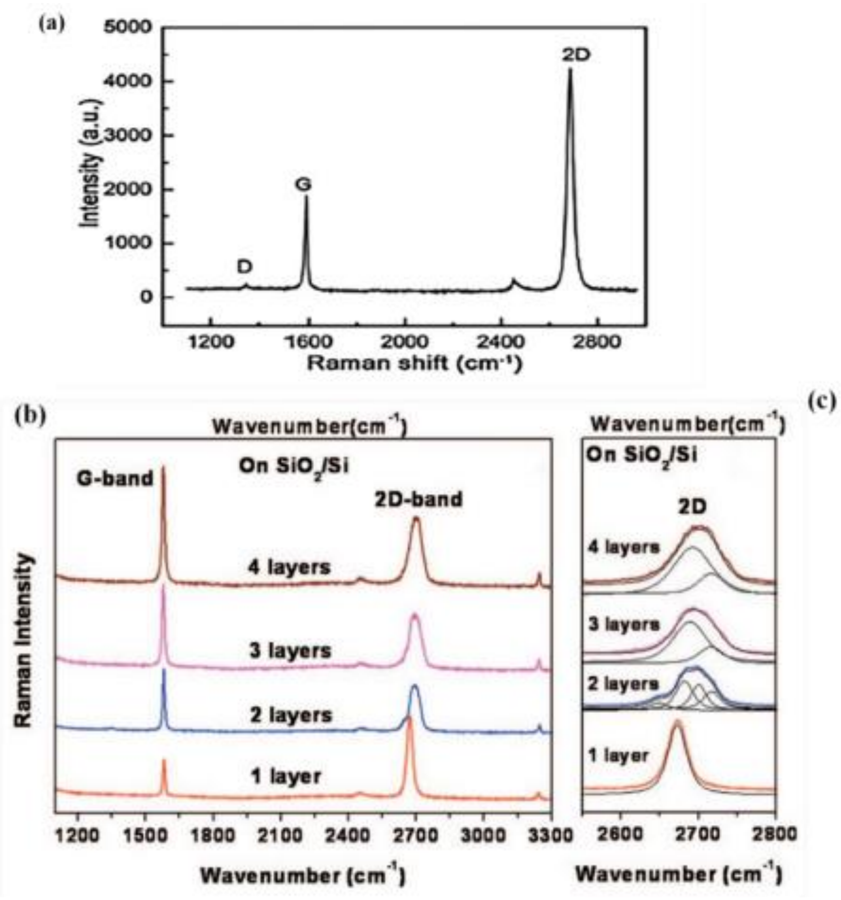

Figure 22:(a) Graphene Raman spectra on $SiO_2$/Si[220], (b) Raman spectra for various layers of graphene on $SiO_2$/Si, (c) 2D band method for determining graphene layer number[221]

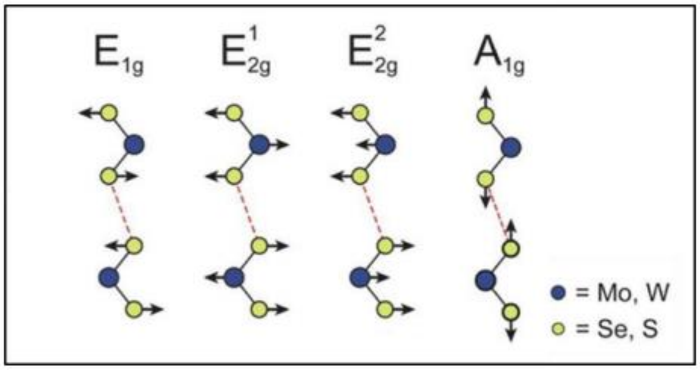

Figure 23: Four Raman active modes of transition metal dichalcogenide shown schematically[222].

In Figure 23, the vibrational modes of TMDs are shown. Backscattering geometry on a basal plane is not possible with the first-order active peak $E_{1g}$. The second-order peak of

$E_{2g}$ is less than 100 $cm^{-1}$, which is relatively low[223]. The wave numbers near the laser would be removed by the notch filters. TMDs' physical properties change as a result of the wide range of vibrational spectrums they show. Raman modes alter when the number of $MX_2$ (M = Mo, W; X = S, Se) similar layers decreases. $MoS_2$ and $WS_2$ layers may be determined by differentiating $E_{2g}$ and $A_{1g}$ modes. For monolayer, the difference in these two modes of $MoS_2$ is 19.5 $cm^{-1}$ while for bilayer it is 21.5 $cm^{-1}$. For $WS_2$, the difference for bilayer is around 63 $cm^{-1}$, but the monolayer difference is approximately 60 $cm^{-1}$, which is equivalent to $MoS_2$ (Figure 24). However, in both $WS_2$ and MoS2, the precise location of the Raman modes has been found to be wavelength dependent[224].

In 1966, Geick et al. presented a complete investigation of h-polarization, based on BN's discovery of four active optical modes [225]after two single Raman lines. Because of h-great BN's symmetry, the combined action of two in-plane modes yields one in-plane mode and one shear mode, and two shear modes can exist on the same Raman shift[226]. The two Raman active modes (Figure 24 (b)) are shear mode (low-frequency phonon) and in-plane mode $E_{2g}$ (high-frequency phonon).

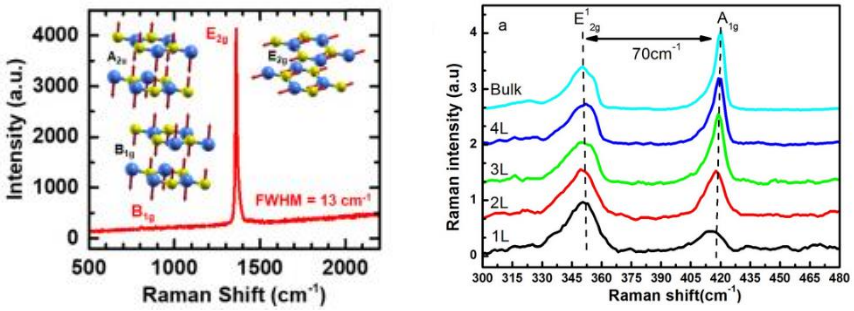

Figure 24 : Absorption band of (a) W$S_2$ from bulk to monolayers, and (b) h-BN from few layers[227, 228].

### 2.4.2 Scanning Electron Microscope:

Figure 25: Field emission scanning electron microscope (FESEM).

The specimens' surfaces are studied using a scanning electron microscope. When an item is exposed to a fine electron beam, secondary electrons are reflected from its surface. "Electron probe" refers to a narrow stream of electrons. The topography of a specimen surface may be investigated using a two-dimensional scanning of the electron probe across the specimen surface and an image of the discovered secondary electrons.

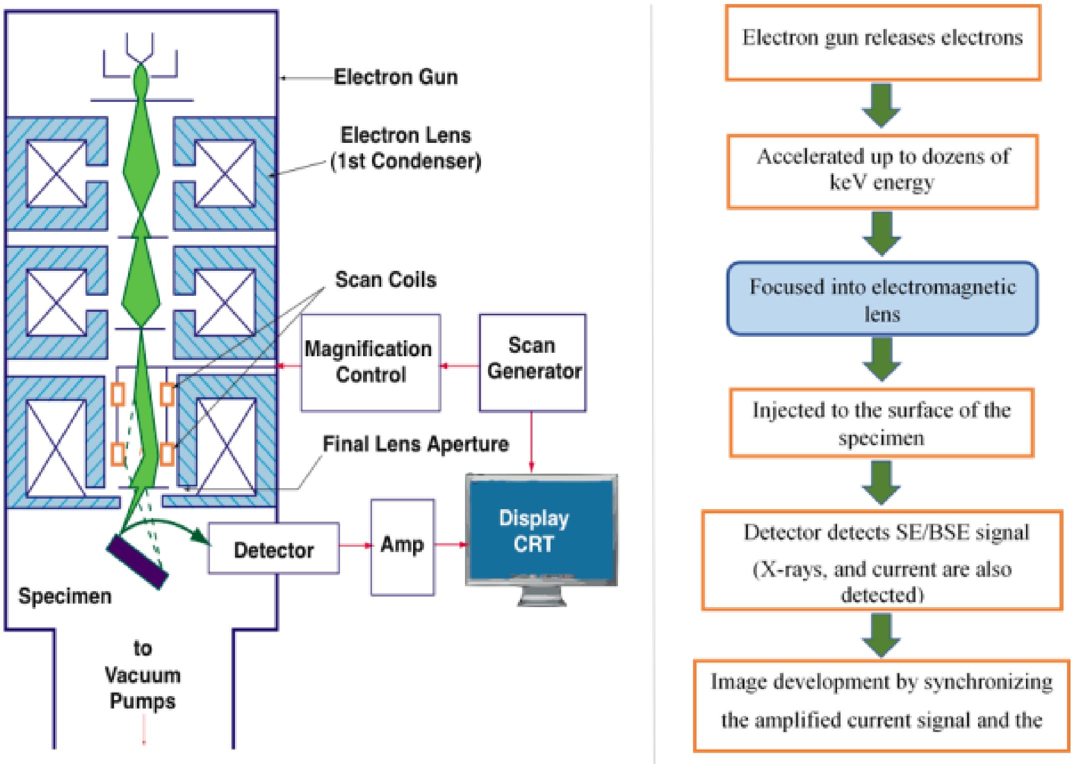

Figure 26: Internal SEM components schematic (left), image formation process flow chart using electron beam in SEM (right)[229].

Nano and micro lengths are regularly studied with scanning electron microscopes. This procedure is popular since it is both quick and painless. As a result, it's handy for looking at internal structures. This therapy has also been proven to be successful. Reduced transmission and the detection of ruptures, folds, and other faults in produced 2D materials on a variety of substrates, as well as voids and impurities, are just a few of the advantages demonstrated.

### 2.4.3 X-ray Photoelectron Spectroscopy:

Because it enables for surface characterization of material composition, X-ray photoelectron spectroscopy (XPS)[230] is an essential technique for evaluating 2D functionalized materials. This approach induces photoelectrons to be released from a material`s surface by stimulating mono-energetic Al K or Mg K x-rays. The energy of the released photoelectrons is detected using an electron energy analyzer. The chemical state, element identification, and amount of a detected element are calculated using the binding energy and intensity of a photoelectron peak. When a photon with an energy of h impinges on the surface, electron activation happens as the first step in a three-step model. Following that, the electron escapes by overcoming a vacuum barrier with kinetic energy $E_{kin}$, which may be measured using an energy analyzer, which can be seen in Figure 27

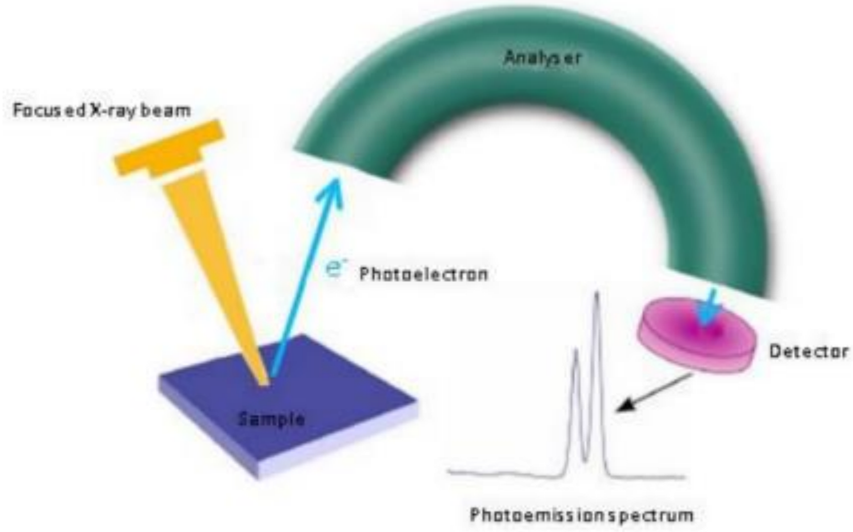

Figure 27: Schematic representation of X-ray photoelectron spectroscopy[231]

The following formula can also be used to convert kinetic energy into a binding energy scale:

$$E_{binding} = E_{Photon} - ( E_{kin} + \phi) \qquad (2.18)$$

The binding energy of an electron is denoted by $E_{bin}$; the energy of X-ray photons is denoted by Ephoton; the instrument's measurement of the electron's kinetic energy is denoted by $E_{kin}$; and the work function is impacted by the spectrometer and the material. is a universal reality that everyone must acknowledge. To explain it, a significant change in the kinetic energy of the photoelectron is all that is required[232]. It is absorbed by the detector of the device. X-ray photoelectron spectroscopy may be used to detect the chemical state and elemental concentration of a material[233]. Because the compositions' binding energy change, the compositions' binding energies differ. The fact that the chemical environment modifies the binding energy of the electron's core level makes this easier.

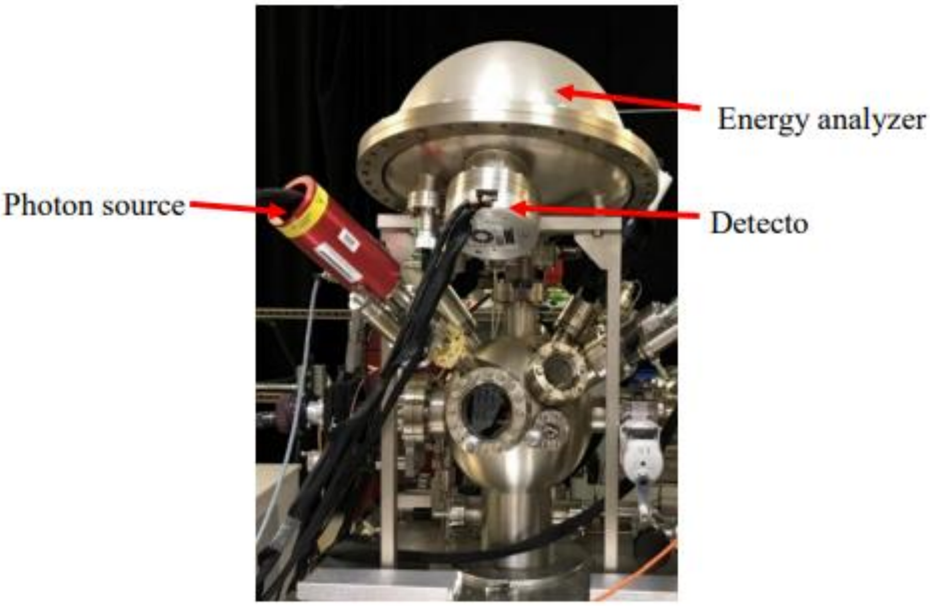

Figure 28: X-ray photoelectron spectroscopy setup used in this investigation.

### 2.4.4 Atomic Force Microscopy:

In 1986, Binning, Quate, and Gerber invented atomic force microscopy[234] as a type of very high-resolution scanning probe microscope. (SPM). It employs a probe to detect friction, height (thickness of 2D materials), and magnetic in samples. This approach may be used to conductors, semiconductors, and insulators, among other materials. It may conduct force spectroscopy on materials by measuring stiffness, young modulus, and other properties that need mutual separation. AFM can create a three-dimensional picture via raster scanning. AFM is made up of a cantilever and a probe tip constructed of silicon nitride or silicon. Hook's law determines how it works. AFM is made up of a cantilever with a tip that is used to scan a specimen using Hooke's law and the deflection of the cantilever as a function of the force between the sample and the tip. The force applied by the probing tip to the sample ranges from 10-11 to 10-6 N. Many different types of probes are used to measure various qualities. Depending on the circumstance, AFM registers many forms of force. Van der Waal forces, capillarity, electrostatic forces, and Casimir forces are among the forces measured.

The sample illumination is determined by the AFM tip type. There are two kinds of modes: static and dynamic. Because the probe and sample are so near to one other, static mode is also known as touch mode. To keep the cantilever's tip from drowning, deep lighting is employed. Depth's repelling force maintains the company's focus on the specimen. Static deflection is used to regulate the tip. High scan speed, ability to scan rough pictures despite significant topographical changes, and high atomic resolution are all advantages of this technology. The approach, on the other hand, has the drawback of being able to deform the face of a 2D sample due to the strong lateral force involved in the mechanism. AC mode is the tapping mode in which the tip is controlled by the oscillation amplitude. The cantilever makes no touch with the sample surface in non-contact mode. Reduced resonance is maintained by Van der Waals forces in the cantilever's oscillated tip, which keeps a gap between the sample and the tip. The tip is controlled by resonance frequency. Furthermore, an x, y plot is used to construct a topographic image by graphing the distance between the image and a tip. While employing contactless mode saves time and eliminates picture distortion, it comes at the sacrifice of higher resolution, which isn't always desirable. Finally, separating the sample diminishes lateral resolution, which influences overall lateral resolution. AC mode switches between contact and non-contact mode. Tap mode is appropriate for samples due to its high lateral resolution, minimum loss of sample quality, and insensitivity to environmental changes. Scanning is slower in touch mode than in non-touch mode.

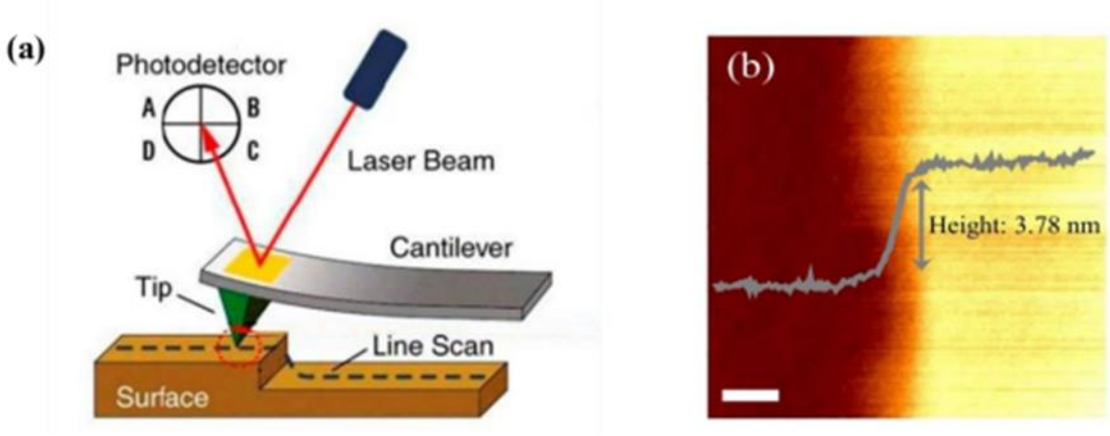

Figure 29: (a) A typical AFM system schematic design [231](b) $WS_2$ AFM image and height profile[235]

As seen in Figure 29 The AFM's central notion is illustrated (a). The surface of a sample is routinely scanned line by line using a cantilever beam with a sharp point at the free end. Due to contact forces between the tip and the surface, the cantilever bends. A laser beam directed on the backside of the cantilever detects its deflection, which is subsequently reflected onto a photodetector. This technique allows for easy monitoring of the cantilever's deflection by adjusting the placement of the laser light on the photodetector. The tip-surface contact is then maintained at a consistent set-point value via a feedback loop in most AFM systems[93].

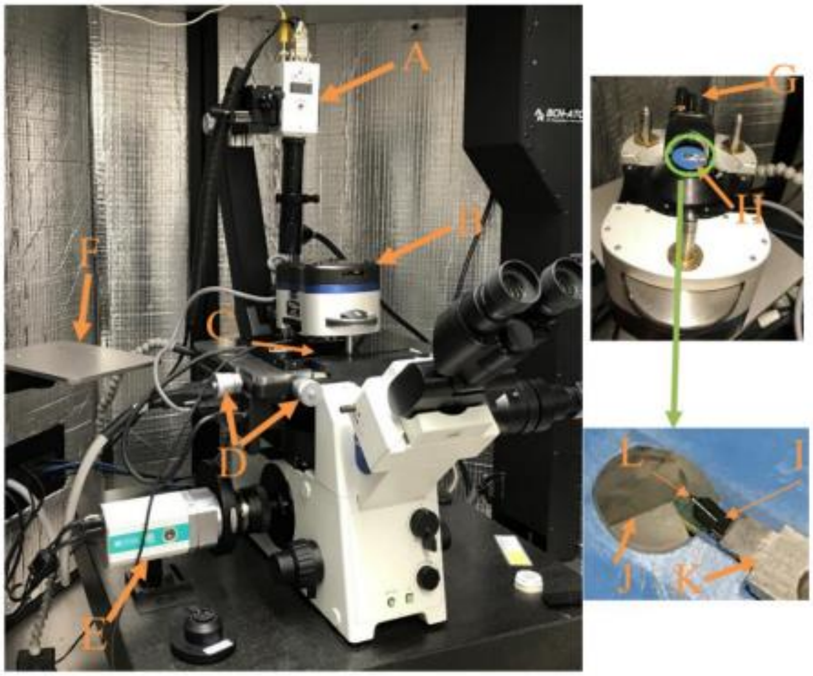

Figure 30: MFP-3D BIO AFM setup that we used to characterize our materials

# CHAPTER 03

# N-TYPE DOPING OF GRAPHENE: IN-SITU THERMOELECTRICPOWER CHARACTERIZATION

## 3.1 Introduction:

In order to create n-type graphene, we employed two different types of doping techniques using ammonia gas ($NH_3$) and liquid Hydrazine ($N_2H_4 \cdot H_2O$.)[236]. The as prepared graphene is typically p-type due to electrochemically mediated charge transfer from ambient[237].

Graphene is a significant scientific achievement as well as a possible choice for next-generation electrical components. The absence of a semiconducting gap in pure graphene limits most electrical applications. Devices composed of zero-bandgap graphene, for example, are difficult to turn off, balancing for analogous metal oxide semiconductor technology's low static electricity. To restrict electron mobility and allow graphene to be used in nanoelectronics devices, a band gap must be formed in it. A bandgap can be created by surface functionalization or chemical doping[238]. Doping graphene can change its physical/chemical characteristics[239], enabling for novel chemistry and physics on graphene, according to theoretical and experimental findings. The perfect $sp^2$ hybridization of carbon atoms are disrupted when other elements are doped into graphene, resulting in significant local variations in electrical performance and chemical reactions.

Boron (B) and nitrogen (N) atoms are suitable candidates for graphene doping due to their comparable atomic size to carbon (C) and their hole acceptor (p-type) and electron donor (n-type) capabilities for substitutional B- and N-doping[240] (Figure 31). Nitrogen doping of graphene can result in important chemical properties like oxygen reduction reaction catalysis or improved lithium intercalation in batteries. Biocompatibility and bio sensitivity may be improved by N-doped carbon nanostructures.

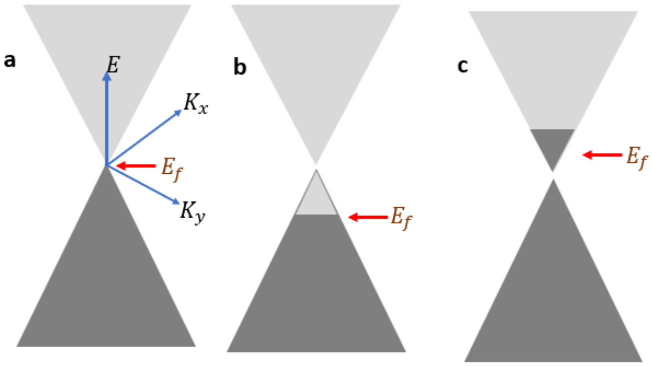

Figure 31:Graphene band structures showing the Dirac cones (a) undoped Graphene (b) p-doped graphene (c) n-type graphene

As illustrated in Figure 31, graphene doped with N atoms has three typical bonding topologies inside the carbon lattice: quaternary N (or graphitic N), pyridinic N, and pyrrolic N. Quaternary N refers to N atoms that replace C atoms in a hexagonal ring. The term pyridinic N refers to nitrogen atoms that are linked to two carbon atoms and supply one p-electron to the aromatic system at the margins of graphene planes. The enhanced oxygen reduction reaction (ORR) activity of carbon materials was commonly thought to be linked to pyridinic N doping. Nitrogen atoms that are connected to two carbon atoms and supply two p-electrons to the system are referred to as pyrrolic N. Because of its unique forms and capabilities, N doped graphene is widely used in electronics, fuel cells, secondary batteries, supercapacitors, and other fields[241].

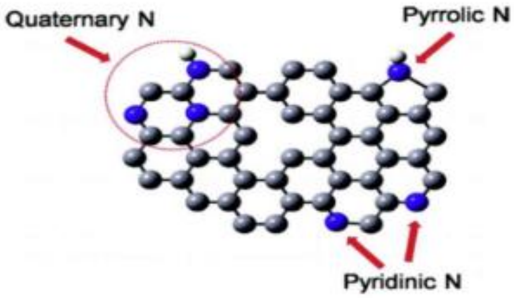

Figure 32; Three popular Nitrogen-doped Graphene bonding arrangements.

### 3.2 Nitrogen Doped Graphene:

Direct synthesis and post treatment are two of the most common ways for creating nitrogen-doped graphene that have been studied. Nitrogen-containing precursors are employed in CVD, segregation, solvothermal, and arc discharge processes, whereas ammonia and $N_2/NH_3$ plasma treatment are used to thermally anneal graphene oxide.

Modifying the flow rate and the carbon source ($CH_4$, $C_2H_4$) to nitrogen source ratio can change the nitrogen content of the CVD process ($NH_3$). The bonding pattern of nitrogen doped graphene varies depending on the catalysts and precursors utilized. During the manufacture of nitrogen doped graphene, the flow rate, catalyst, and increasing temperature are all employed to modify the doping environment. Because carbon atoms are partially replaced by nitrogen atoms when carbon material is subjected to a nitrogen plasma environment, this process was used to create nitrogen doped graphene[242]. Plasma strength and/or exposure period can readily impact nitrogen concentration.

## 3.3 Synthesis of Pure Graphene and Nitrogen Plasma Doped Graphene and their characterization:

Without the requirement for a transferring procedure, graphene was synthesized on $SiO_2$ substrates utilizing Plasma Enhanced Chemical Vapor Deposition (PECVD). Graphene on $SiO_2$ surfaces were used in electrical measurements. To evaluate thermopower, two Chromel (KP/Au7 at. percent Fe (Au: Fe) thermocouples and a platinum resistive heater were utilized. Figure 34(a) shows a custom-built split ring capacitively linked RF plasma system for producing nitrogen plasma at certain value of temperature (13.56 MHz, maximum power 600 W). The plasma exposure period was managed by controlling time of growth of the samples in real time (during the experiment). A chip carrier containing the graphene sample was relocated to a closed cycled refrigerator (Janis Research Co. CCS-350ST-H) capable of cooling down graphene samples from room temperature to a 20 K base temperature to measure thermopower at both room-temperature and low-temperature. A Lakeshore type EM4-CV 4-in. gap, Horizontal Field electromagnet encloses the sample-holding refrigerator column, generating a magnetic field that can be swept between -1 and +1 T.

## 3.4 Preparation of Samples for Thermopower Measurements After PECVD:

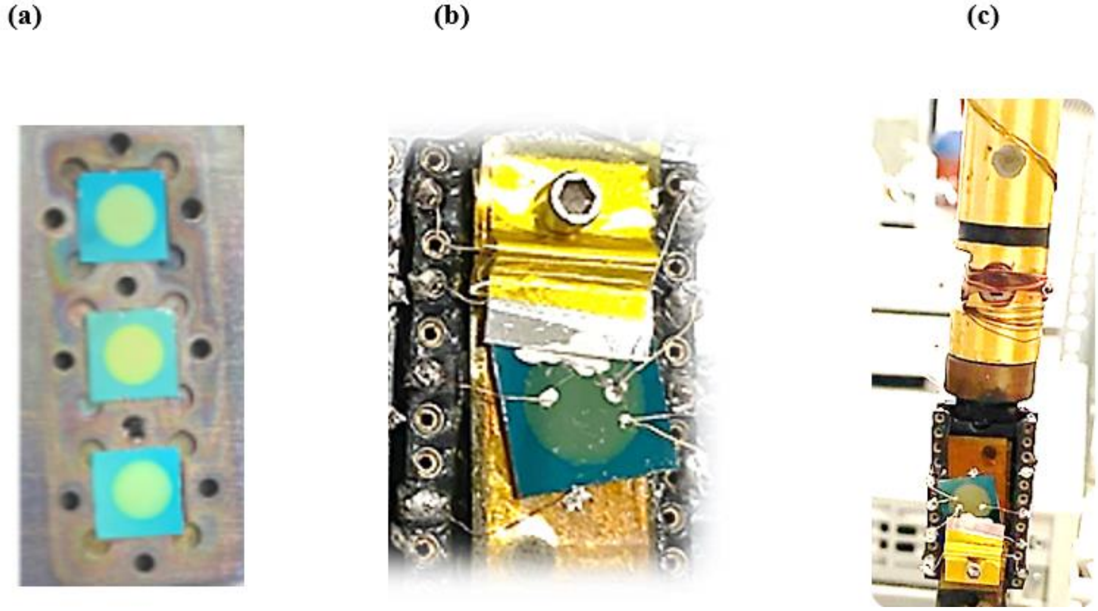

Figure 33: (a) Samples after synthesis (b) Sample with electrical contacts mounted on a chip carrier (c) Chip carrier inserted into a closed cycled refrigerator for low temperature measurements.

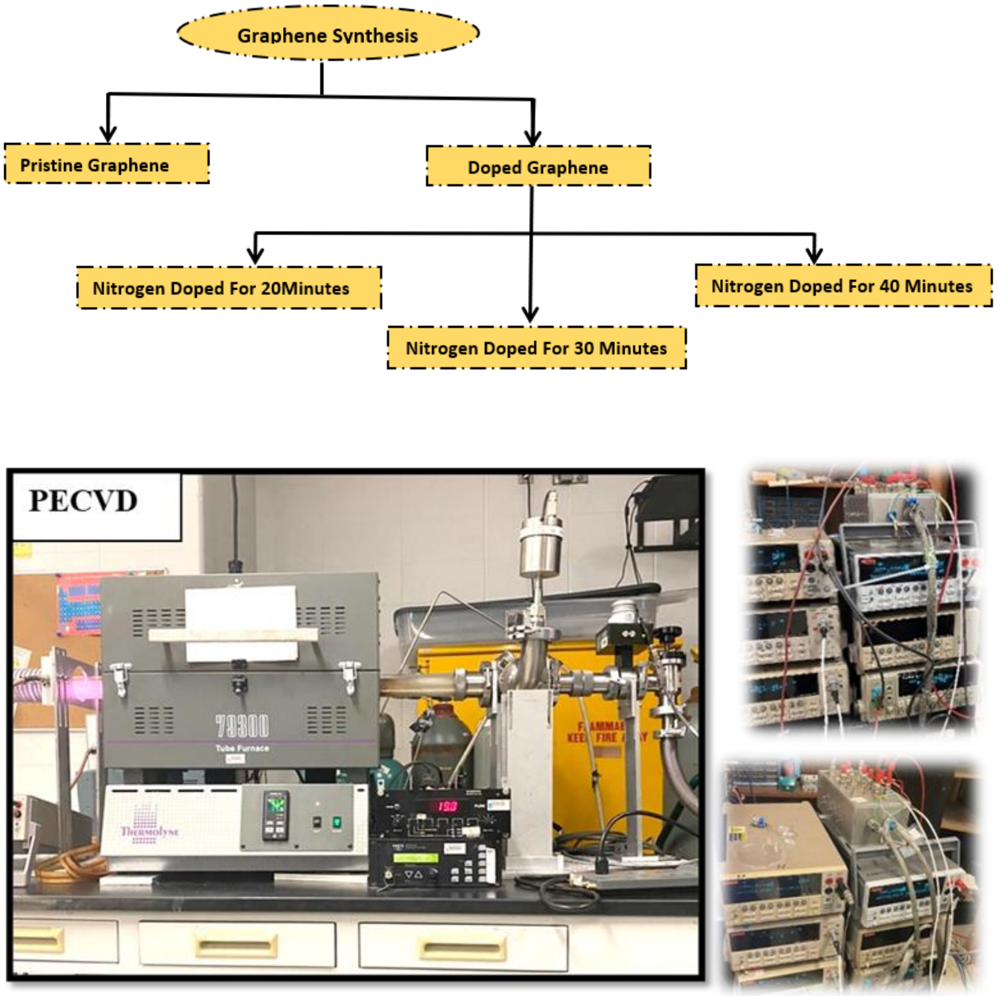

Figure 34: (a) Synthesis of *in-situ* Nitrogen doping of Graphene (b) thermopower/resistance measurement setup.

An Invia Renishaw Raman spectrometer with a 632 nm excitation wavelength was used to collect the Raman spectra for all four graphene samples starting from pristine graphene to three different levels of nitrogen doping[243]. The investigations were carried out at room temperature as well as at low temperatures under ultrahigh vacuum. The time of exposure to ammonia (nitrogen) plasma was set to 20 minutes, 30 minutes, and 40 minutes respectively. The temperature dependence of the thermopower of each sample was also measured. Each sample was handled with extreme caution during the operation to ensure that it was not damaged in any form.

## 3.5 Hydrazine doping:

### 3.5.1. Procedure:

During the first part of the experiment, the vacuum pump is utilized to remove all matters from the chamber. As a result, a clean vacuum is required for a wide range of exciting scientific applications, particularly those requiring physical extremes such as severe cold and high energy. A perfect vacuum is defined as a space that is devoid of matter. The absolute pressure within a chamber can be used to assess whether or not a vacuum occurs. When the pressure is low, the vacuum is larger. Although applying force on a surface to detect a vacuum is popular, it is not necessarily the best strategy. This is especially true when there is a lot of vacuums (low pressures). Therefore, in our experiment, at very low pressure ($10^{-6}$torr), the vacuum pump was turned off to immediately introduce Hydrazine dopant (Liquid phase) to the graphene sample for certain amount of time, so while the Hydrazine was exposed to graphene sample, so, as a result, the pressure went up to certain value. After the first exposure time, the valve key being immediately closed. At this stage, waiting is a crucial to have a saturation phase. By reaching saturation phase, the second and third exposures of Hydrazine have been managed as the first exposure, the difference is that at each exposing of Hydrazine the pressure has been increasing and the thermopower signs (TEP) of graphene converted from positive to negative signal (P-type to N-type). Using an analog-subtraction method, we measured the thermopower of p and n-graphene in our lab. The tests used two micro thermocouples (Chromel (KP)/Au7 at. % Fe (Au/Fe; 100 m diameter) and a resistive heater. The deposited graphene was revealed to be p-type, with a thermopower of +60 mV/K Graphene was n-doped by exposing it to hydrazine. Figure 36 displays the thermopower conversion of graphene to hydrazine at room temperature. The places where hydrazine was given at pressures of 3, 7, and 10 Torr are shown by decreasing arrows. The thermopower declined after the initial 3 Torr exposure, turned negative, and finally became saturated at 10 mV/K. Thermopower saturation occurred at -55 and -80 mV/K after further exposure to pressures of 7 Torr and 10 Torr, respectively. With ammonia, the thermopower of n-doped graphene is -250 mV/K. (See Fig. 35).

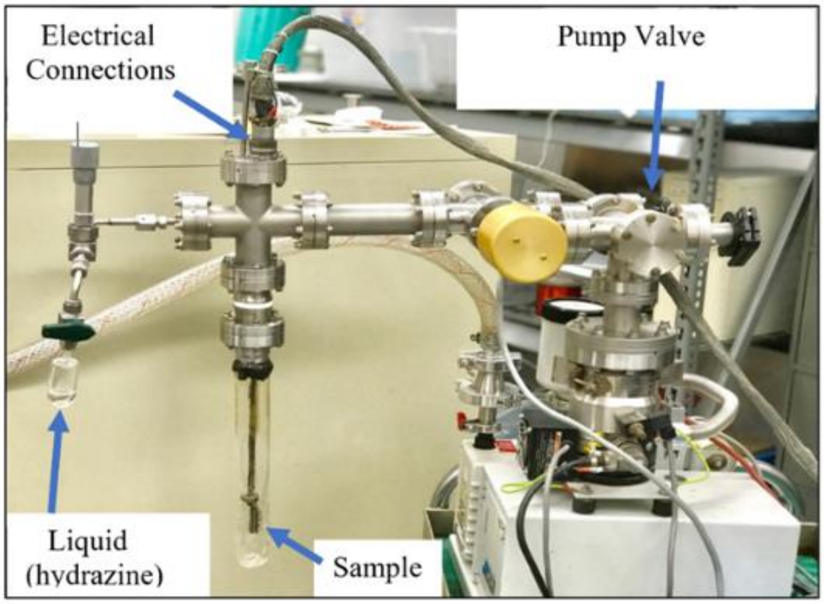

Figure 35: In-situ Hydrazine doping set up

### 3.5.2 Results and Discussion of Hydrazine doped graphene:

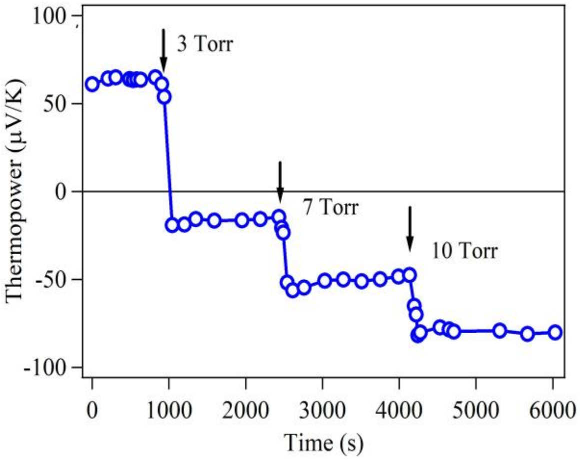

Figure 36: At ambient temperature, graphene's thermopower reaction when exposed to hydrazine. The downward arrows represent the locations where hydrazine was delivered at 3, 7, and 10 Torr.As a function of time, the thermopower of p and n-graphene types.

## 3.6 Characterization of nitrogen doped Graphene Samples:

### 3.6.1 SEM Images of Nitrogen doped graphene:

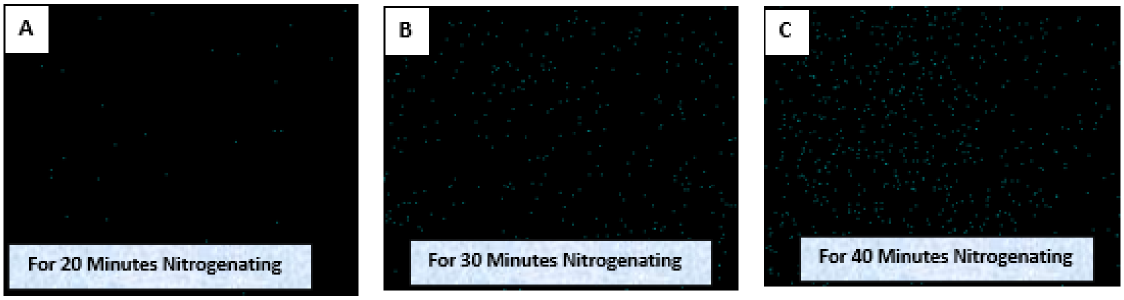

Figure 37: EDAX mapping of nitrogen in all Nitrogen Doped Graphene Samples at different time of nitrogenating.

As illustrated in Figure.37, the rates of nitrogen doping in EDAX images may be correlated, ranging from the lowest to the highest degree of doping in all three exposures. The degree of nitrogenation in Figures A (20 min), B (30 min), and C (40 min) is seen to increase as the doping duration is increased. As a result, the sign of TEP has been modified from positive to negative (P-type to N-type) systematically[244].

## 3.7 Results and Discussions of Nitrogen Doped Graphene:

### 3.7.1 Electrical Measurement of TEP At Ambient Temperature:

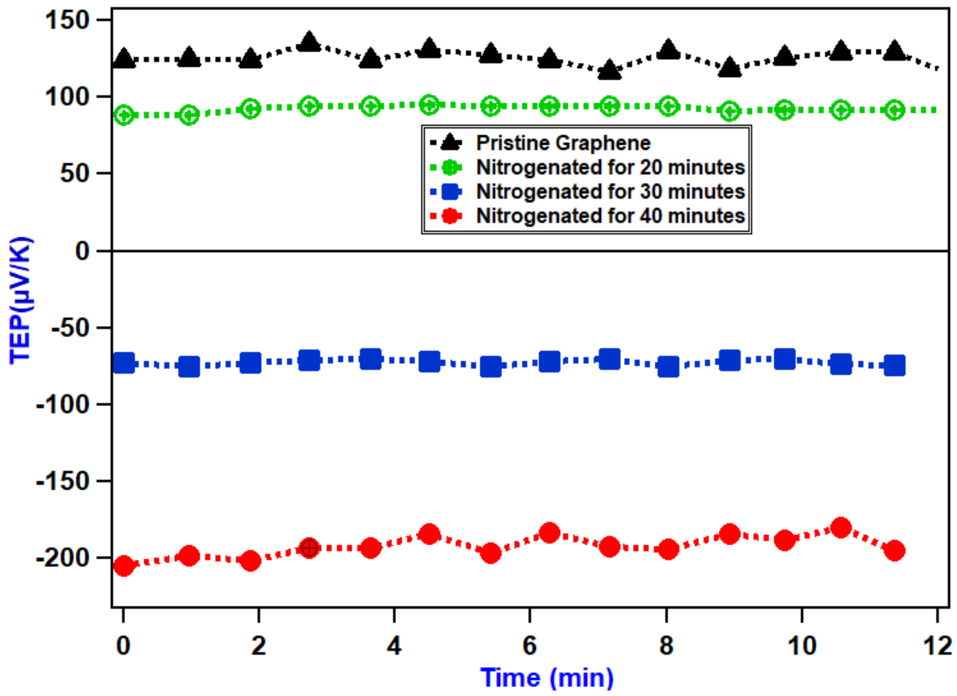

Figure 38: Ex situ thermopower measurement at room temperatures for pristine graphene and nitrogen doped graphene samples.

### 3.7.2 Electrical Measurement of TEP At Low-Temperature:

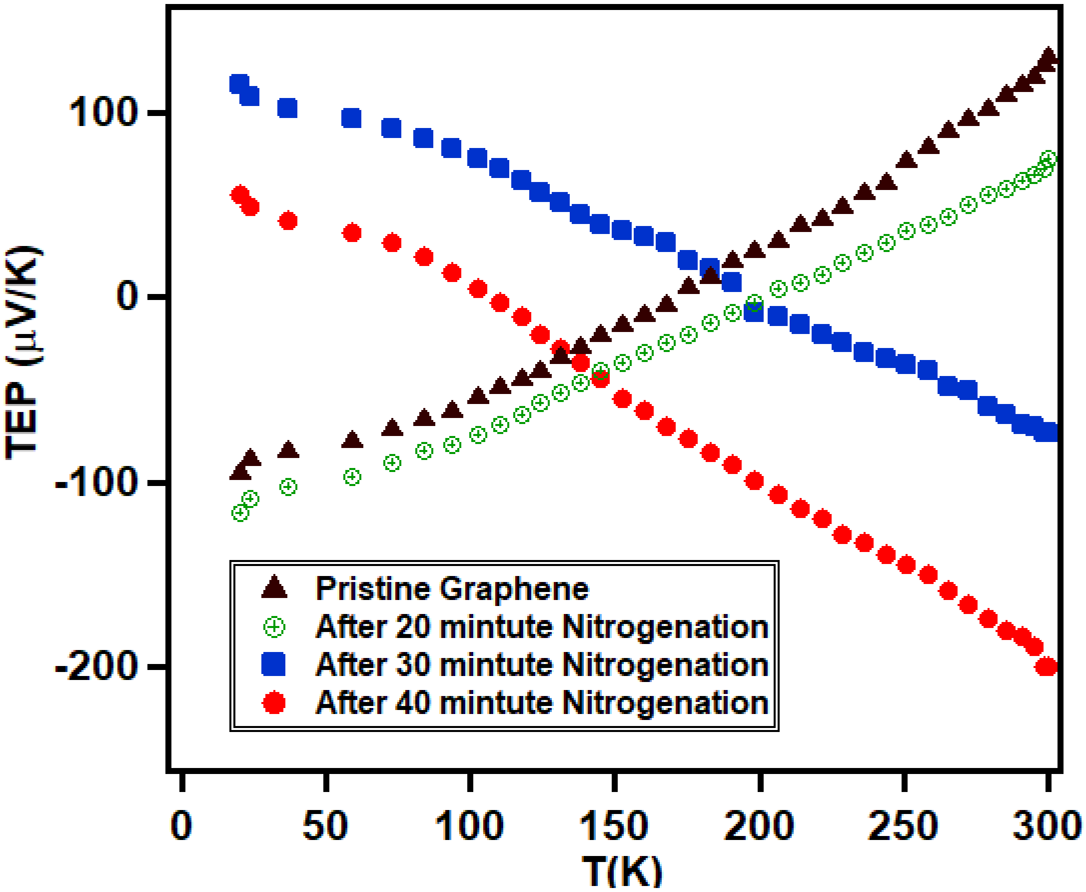

Figure 39: Thermopower of graphene as a function of temperature before and after nitrogen doping (Low temperature inset below 27K).

As it can be shown in Figure 38 and 39, as prepared graphene is p-type due to the electrochemically mediated charge transfer involving oxygen and water molecules in the ambient. In the case of nitrogen doping, we were interested in the effect of substitutional doping of graphene with nitrogen[245], which has a less profound effect on functional groups such as oxygen. To grow graphene in its pure state[246], Graphene was deposited directly on a Si/$SiO_2$ substrate using an RF-PECVD method developed in our lab. A home-built split-ring radiofrequency (13.56 MHz, maximum power 600 W) device was used to make plasma. The whole Si/SiO2 substrate must be meticulously cleaned to eliminate any pollutants before the graphene layer can be created as a thin film. Consequently, all the substrates were sonicated for 10 minutes in acetone before being dried in a nitrogen flow and inserted into the quartz reactor. Following that, the reactor was evacuated to less than 4 mTorr and progressively heated to 650 °C in an Ar/$H_2$ (40 vol percent argon, 60 vol percent $H_2$) flowing gas combination at a rate of 10 standard cubic centimeters per minute (sccm). Despite the temperature increase, the pressure stayed constant at 200 mTorr. After the heating phase was completed, a 15-minute period of hydrogen plasma at 50 W was ignited. Following the removal of the Ar/$H_2$, a flow rate of 5 sccm of pure $CH_4$ (99.8 percent) was injected into the growth chamber for 40 minutes at an 80 W plasma power. The sample was subsequently cooled to room temperature at a rate of 20°C/mi. The second, third, and fourth samples were doped with nitrogen gas (doped samples). All the parameters in these sample instances were the same as in pure graphene, except for the plasma power of 25 W and the doping duration. In the second sample, nitrogen and $CH_4$ gases were injected simultaneously for 20-40 minutes, 30-40 minutes in the third sample, and 40-40 minutes in the fourth sample. The nitrogen gas was turned off after 20, 30, and 40 minutes in three independent experiments. At room temperature, the pristine and first nitrogen doped graphene samples were p-type, but the third and fourth samples were n-type graphene. By cooling all these samples to very low temperature, S was seen to convert from its (p-type) to (n-type) state for pure graphene and 20 minutes nitrogen doped graphene[240]. However, S was changed from its (n-type) to its (p-type) for 30 and 40 minutes of nitrogen doped graphene samples[247]. As a result, the temperature dependence of the thermopower characteristics of pure graphene and three nitrogen-doped graphene was examined. S(T) in purer graphene and for 20 minutes-nitrogen-doped graphene moved from p-type to n-type, while for 30 and 40-minutes nitrogen-doped graphene changed from n-type to p-type. Nitrogen-doped graphene accounts for the increased scattering caused by nitrogen dopants, as well as the presence of localized states in the conduction band[243].

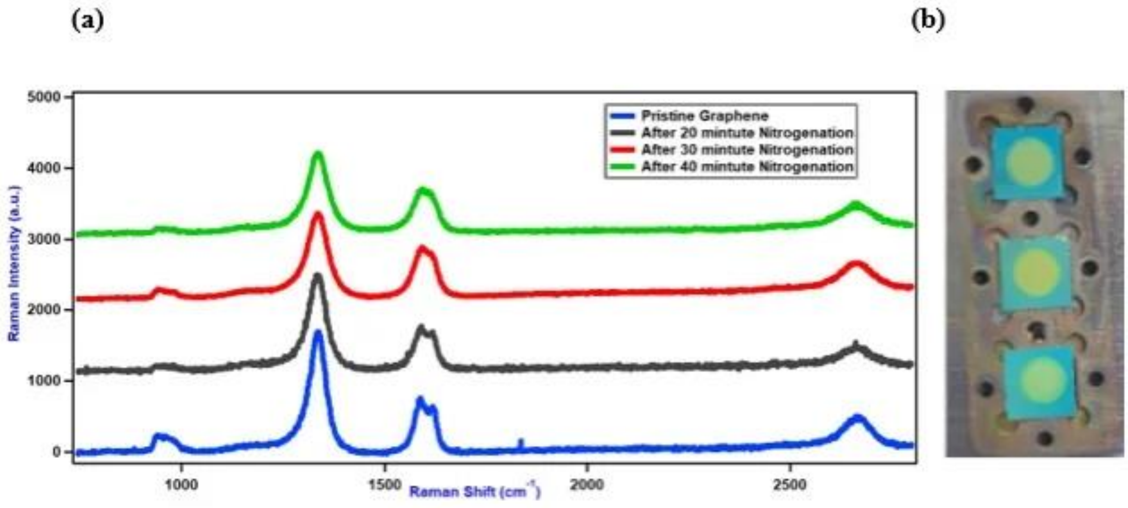

Figure 40:((a) The Raman spectra of nitrogen-doped and pristine graphene (b) Optical images of samples before making electrical measurements of TEP.

The two intense peaks, G band at 1580 cm$^{-1}$ and G′(2D) band at 2700 cm$^{-1}$, are characteristic of graphene samples due to the in-plane vibrational ($E_{2g}$) mode and two phonon intervalley double resonance scattering. The D band, which has a peak at 1340 cm$^{-1}$, is thought to connect domain boundaries and growth nucleation sites. Due to its high degree of crystallinity, pure graphene has a substantial I(G)/I(D) G-band and D-band intensity ratio, as well as a significant I(2D)/I(G) 2D band and G-band intensity ratio (G). Furthermore, the great symmetry of the 2D band suggests that the graphene sample is mostly monolayers[248]. Following nitrogen doping, the D band intensity is restored to its pre-doping state. Nitrogen-doped graphene becomes increasingly intense as phonons interact with elastically distributed photoexcited electrons generated by nitrogen atoms in the lattice[249].

Intravalley double resonance scattering mechanisms are hypothesized to be responsible for the development of the D' band in nitrogen-doped graphene[250].

### 3.8 Conclusion:

In conclusion, a closed cycle refrigerator was used to evaluate the thermopower of all four graphene samples at ambient and low temperatures. It can aid processing technology understanding by tracking doping impacts and doping throughout the specimen manufacturing phase in real time. It illustrates how changing the Fermi level above the Dirac point may affect graphene's electrical characteristics. In situ temperature measurements are essential for understanding electron doping and scattering processes. They demonstrate that raising the elastic intervalley scattering improves the weak localization of nitrogen-doped graphene by enhancing disorder with short-range potentials. To illustrate the influence of doping concentration on Raman structural information, nitrogen-doped graphene, and cooling down all the three doped samples were employed, as well as changes in thermopower signals from p-type to n-type and vice versa.

# CHAPTER 04

# DIRECT QUANTUM TUNNELING

## 4.1 Introduction:

The tunneling transport phenomenon in quantum devices offers picosecond switching speeds and hence the possibility of designing very high-speed devices[251]. Two-dimensional electron gas (2DEG) systems have played a vital role in the development of superior electronic devices[252]. However, one lesser-known device that utilized 2DEGs is a tunnel junction consisting of two such gases [253, 254], realizing 2D–2D tunneling. Previous studies of 2D–2D tunneling were conducted on coupled electron gas systems in two closely placed quantum wells in AlGaAs/GaAs heterostructures[255]. In the case of unequal doping of the 2DEGs, it has been shown experimentally that, at a voltage bias corresponding to aligned band structures of the 2D systems[256], a sharp peak in the tunnel current occurs. This peak is referred as a resonant peak in the tunneling[257]. It was claimed in the prior work that the width of this resonant peak was temperature independent (except possibly from inelastic effects)[257-260].

Presence of negative differential resistance (NDR) is characteristic of the current–voltage relationship of a resonant tunneling device[261], enabling many unique applications[262]. The existence of devices with NDR has been reported since the late 1950's in devices that contained degenerately doped p-n junctions with thin oxide barriers (tunnel diodes) and double barrier heterojunction devices where quantum tunneling effects are utilized. The

NDR in the I-V characteristics of these devices has been used in many applications[263] involving microwave/millimeter wave oscillators, high speed logic devices and switches.

With the advent of the new 2D electronic material systems, it has opened a new route for 2D–2D tunneling in such extended systems[264]. Two-dimensional(2D) materials such as graphene, hexagonal-boron nitride (h-BN), transition metal dichalcogenides (TMDCs) and phosphorene etc. have gained a vast interest due to their excellent performance in novel electronic, optoelectronic, and photovoltaic applications[265]. Graphene and h-BN have been unsuitable for electronics applications which require tunable band gap materials since graphene is metallic while h-BN being wide band gap semiconductor[266]. Strong reactivity of phosphorene, with oxygen and water and requires to be sandwiched between layers of other materials if it is to last longer than a few hours[267]. TMDCs are much slower conductors of electrons than graphene or phosphorene, even though they are semiconducting and stable. In order to evade such limitations, researchers have attempted a combination of metallic (graphene etc.), insulating (h-BN etc.) and semiconducting ($MoS_2$ etc.)[268]. Features of this approach include adding some functionality into such 2D structures[249, 269], combining into nanocomposites to optimize many inherent properties such as optical absorption etc[270]. and, stacking them vertically layer-by-layer or arrange laterally by seamlessly stitched in-plane heterojunctions[271].

Heterostructures play a vital role in semiconductor industry. The newly developed monolayer 2D materials offer a platform that allows creation of heterostructures with a variety of novel properties. Many structural, physical, and chemical properties have been explored on Van der Waals heterostructures created by monolayers of multiple 2D materials with vertically stacked layered heterojunctions[272]. Since these heterostructures utilize the Van der Walls interlayer interaction, lattice matching is no longer a significant factor. The interface is atomically sharp, and the junction can be as thin as two atomic layers to reach the ultimate limits. Such stacks are very different from the traditional 3D semiconductor heterostructures, as each layer acts simultaneously as the bulk material and the surface and thereby reducing the amount of charge displacement within each layer. In addition, these structures are flexible and stable with compatible fabrication thin-film technologies.

In recent years, there have been various studies on graphene-2D materials heterostructures demonstrating novel charge transport properties across the interface[273]. Such graphene-TMDs structures have been introduced for various device applications and, also been of particular interest in the spectroscopy community[274]. For example, many groups demonstrated the vertical tunneling transistors with high on-off ratios and large current densities that used TMDs thin layers as tunneling barriers and graphene as one or both electrodes[275].

An ideal 2D material for next generation of functional devices should meet the following important criteria. They must be (i) one-atom thick (for fastest conduction of electrons), (ii) be highly stable (even at high temperatures), (iii) possess a small and tunable band gap and, (iv) scalable in both synthesis and processing with the ability to integrate with existing technology etc.

Lithography methods in various forms are widely used in many research fields for making functional devices, including tunnel junctions. In the traditional top-down lithography technology, high-cost equipment including predesigned masks and collimated light sources are used, which also include complex and time-consuming production steps. Electron beam lithography has capability to write nanoscale patterns without using any physical mask[276], but again the expensive equipment and low patterning speed associated with it suppress its extensive applications[277]. Further, 2D materials having single or few atomic layers, are particularly sensitive to surface contaminants, including resist residues left behind by lithographical processes, which in turn modify the electrochemical potential and act as extra scattering sites. Though annealing techniques have been demonstrated to improve device mobility[278, 279], they are not well controlled and do not always yield consistent results.

However, the employment of a vertical geometry enables overcome of both (i) the lithographical limitations inherent with in-planar geometry and (ii) poor scalability still sustaining large current modulations. Thus, there has been significantly increased interest on improving bottom-up techniques of lithography-free patterning in recent years. To achieve regular nanoscale patterns without using any mask, techniques like laser interference and nanosphere lithography have been developed as alternative routes[280]. Lithography-free fabrication techniques have been reported especially for simple geometries yielding simple, inexpensive[281], and free of resist processing with increased device throughput. Most importantly, lithography free techniques can be used by anybody who doesn’t have access to clean room facility.

Chemical vapor deposition (CVD) has been found to be the best technique to synthesize uniform and large-scale graphene on metal substrates such as Copper and Nickel foils[282, 283]. However, high processing temperatures (1000-1600 °C) of thermal CVD growth of graphene[284, 285] is costly and limits its direct applications in certain devices. The graphene films grown on metals need to be separated from the metal substrates and then transferred to insulating substrates (e.g., dielectrics, insulators) for further electronic processing[286]. Currently, the most common approach to transfer graphene is the use of polymethyl-methacrylate (PMMA) or polydimethylsiloxane (PDMS)[287]. The appearance of cracks or tears, and contamination of PMMA into graphene are inevitable during such complicated transfer procedures. In this regard, plasma-enhanced CVD (PECVD) has been commonly employed to synthesize transfer-free graphene and graphene nano-walls on different substrates including both metals and insulators at lower synthesis temperature[288, 289].

Here, we experimentally investigate the possibility of using graphene/h-BN/graphene in direct quantum tunnel junctions and resonant tunneling devices[290]. With the recent advancements of synthesis of graphene and h-BN on any arbitrary substrate using PECVD and fabrication of vertically stacked electronic devices using a simple lithography free technique allows us to address this question easily and rapidly since h-BN has great potential to be used as the tunneling barrier layer in functional heterostructure devices. The combination of graphene and h-BN opens the exciting possibility of creating a new class of atomically thin multilayered heterostructures. In particular, this work focuses on the situations when the two graphene sheets have unequal doping, e.g., one is n-type (electron doped) in a single tunnel junction device and the other is p-type (hole doped). In this study, graphene and h-BN were directly deposited by radio frequency-plasma enhanced chemical vapor deposition (RF-PECVD)[291]. In the case of graphene, methane ($CH_4$) gas was used whilst ammonia borane was used for h-BN synthesis[292].

## 4.2 Experimental:

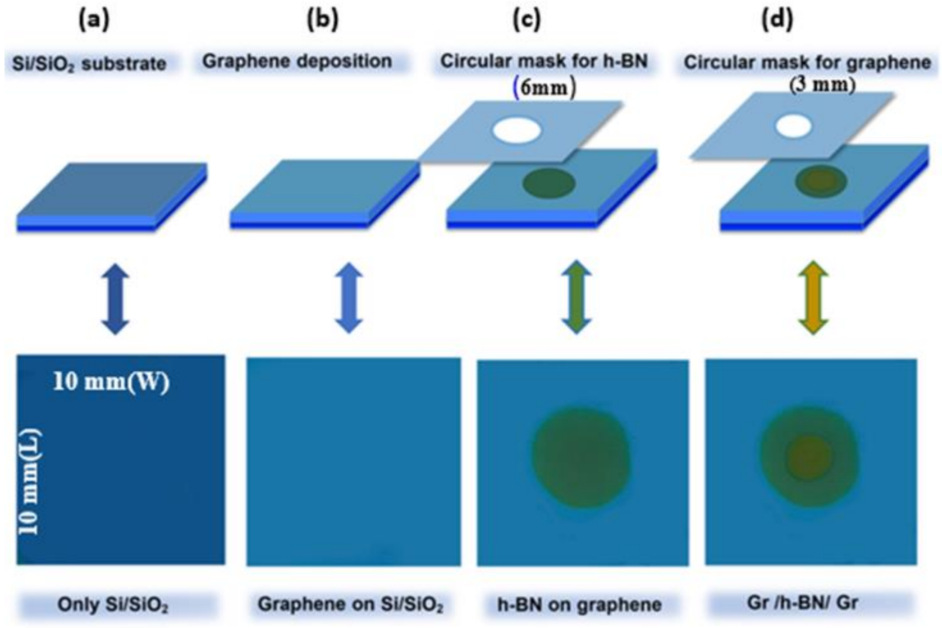

Figure 41:Single Quantum Junction (Single Barrier Junction)

Figure 41: The scheme of Graphene/h-BN/Graphene tunnel junction fabrication. The top raw represents schematic diagrams while the bottom raw show the optical images of the sample after each step. (a) bare Si/$SiO_2$ substrate (b) Si/$SiO_2$ substate completely coated with graphene (c) h-BN patch defined on the bottom graphene layer using a circular mask (6 mm diameter) (d) final graphene top layer deposited on the h-BN patch using a circular mask (3 mm diameter).

Graphene was directly deposited on Si/$SiO_2$ substrate using RF-PECVD technique developed in our laboratory[246]. A home-made split ring radiofrequency (13.56 MHz, Max. power 600 W) system was used for plasma generation. Proper cleaning of the substrate is a required to avoid any kind of contamination prior to synthesizing the graphene layer as a thin film on the entire Si/$SiO_2$ substrate. Therefore, all the substrates were sonicated in acetone for 10 min and dried in a flow of nitrogen before placing them inside the quartz reactor. Then the reactor was evacuated to a pressure lower than ~5 mTorr and gradually heated to 650 °C in a flowing gas mixture: $Ar/H_2$ (40 vol % argon, 60 vol % $H_2$) at a flow rate of ~20 standard cubic centimeter per minute (sccm). The pressure was maintained at ~200 mTorr during this temperature ramp. Hydrogen plasma was ignited at the power of 50 W for 20 minutes after the heating step. Pure $CH_4$ (99.8%) at a flow rate of ~3 sccm was introduced into the growth chamber immediately after switching off the $Ar/H_2$ and plasma power of ~80 W was maintained for 30 ~ 120 minutes. The samples were then cooled down to room temperature at a rate 25 °C/min.

Next, we prepared the sample for the deposition of h-BN using PECVD with ammonia borane (with 97% purity**)** as the source material[293]. The substrate with previously deposited graphene layer was covered with a circular shadow mask was placed inside the reactor at a desired position. Then, a ceramic boat containing borane ammonia borane was located in between the plasma reactor and the furnace. A heat belt was wrapped over the quartz tube covering the ceramic boat to sublime borane ammonia. Then the reactor was evacuated until the pressure lower than ~5 mTorr and gradually heated to 750 °C with the gas mixture: $Ar/H_2$ (40 vol % argon, 60 vol % $H_2$) at a flow rate of ~50 sccm. The ceramic boat was heated gradually from room temperature up to 180 °C and left for 45 minutes and the plasma was maintained at 100 W. The samples were then cooled down to room temperature at a rate 25 °C/min. Finally, the third graphene layer was deposited as before using another mask with a smaller opening.

As prepared graphene shows p-type behaviour. To be used in resonant tunneling devices, it was necessary to dope it  n-type by exposing to hydrazine at room temperature. The graphene sample was placed inside a reactor which was connected to a vial containing hydrazine. The reactor was pumped and hydrazine was admitted to a pressure of 10 Torr in sequence. We also synthesized n-type graphene directly by PECVD using anhydrous ammonia with $CH_4$. Same procedure as in the synthesis of p-type graphene was followed except that ammonia gas was introduced along with $CH_4$ as a dopant for 10 minutes**.** Figure 41 shows the sequential processes of fabricating graphene/h-BN/graphene-based device. The top raw in Fig. 41 represents the schematic diagrams while the bottom raw show the optical images of the sample after each step. (a) bare Si/$SiO_2$ substrate (b) Si/$SiO_2$ substate completely coated with graphene (c) h-BN patch defined on the bottom graphene layer using a circular mask (6 mm diameter) (d) final graphene top layer deposited on the h-BN patch using a circular mask (3 mm diameter)

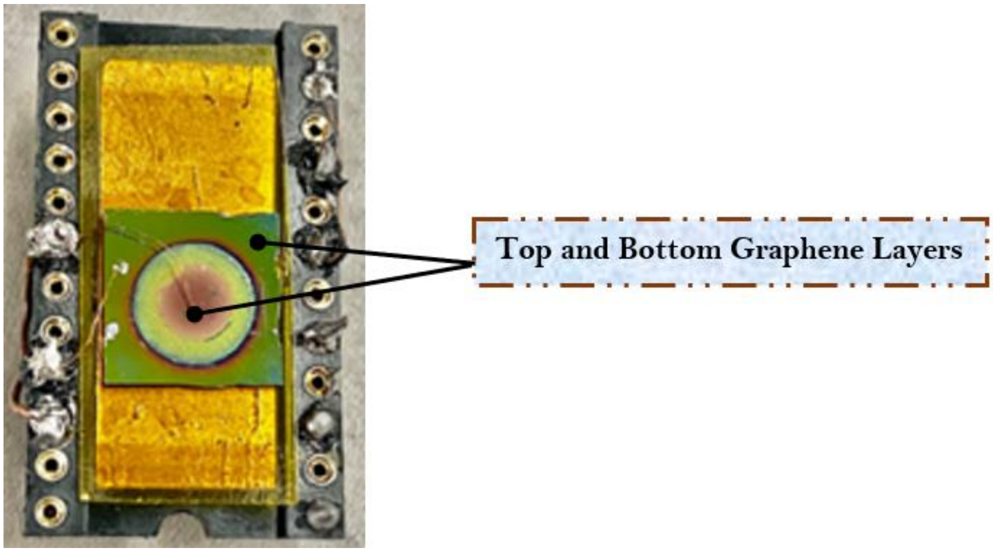

Figure 42: Three layers Sample onto the Chip Carrier with Two Copper Wires for Measurement.

## 4.3 Characterization:

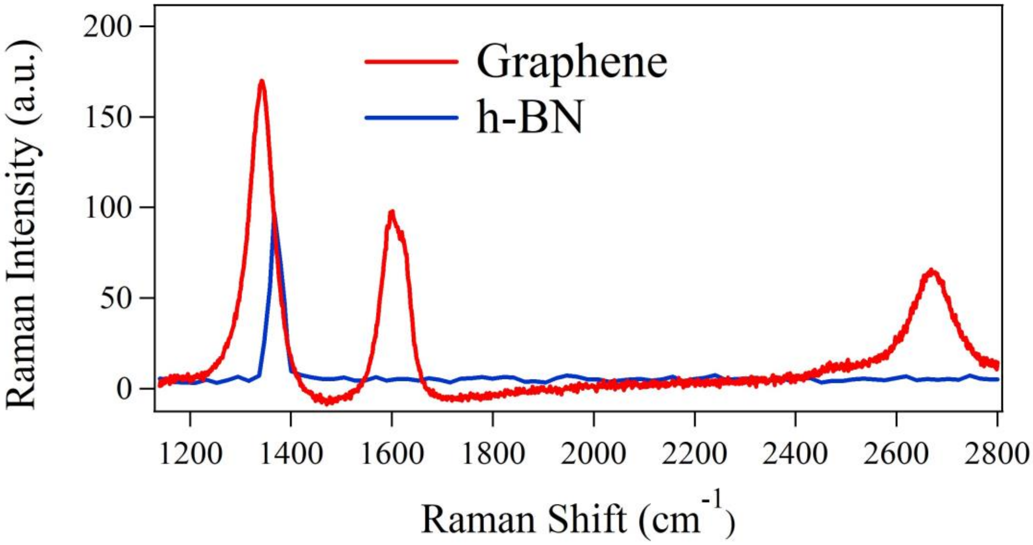

Figure 43: Raman spectra of the graphene and h-BN using 632 nm laser excitation in a Renishaw InVia Raman spectrometer**.**

Graphene and h-BN films were characterized by Raman spectroscopy with a spectral resolution better than 1 cm$^{-1}$ . A Renishaw inVia spectrometer with a grating of 1800 lines/mm, a charge-coupled device (CCD) detector was used with 632 nm laser excitation. Figures 43 shows the Raman spectrum of graphene and h-BN. The Raman peaks of graphene appearing at 1346 cm$^{-1}$, 1596 cm$^{-1}$, 1628 cm$^{-1}$, and 2677 cm$^{-1}$ are characteristic of D, G, D’, and 2D bands of graphene. The D (1346 cm$^{-1}$) band is known as the disorder band associated with the defects of graphene. G (1596 cm$^{-1}$) is a primary in-plane vibrational mode involving the sp$^2$ hybridized carbon atoms that comprises the graphene sheet. The D’-band (around 1628 cm$^{-1}$) is associated with edges and structural disorder in graphene films. 2D or G’ (2677 cm$^{-1}$), is the second-order overtone of the D band corresponding the result of a two-phonon lattice vibrational process. The full width at half maximum (FWHM) of G band and 2D band are 32 cm$^{-1}$ and 64 cm$^{-1}$respectively. The intensity ratio between G band and 2D band, $\frac{I_G}{I_{2D}}$ is 0.82. The PECVD technique allows the growth of graphene on both conductive and insulated substrates with almost the same quality. The Raman spectrum of h-BN consisting of a peak at ~1367 $cm^{-1}$ with the FWHM of 13 $cm^{-1}$which is assigned to the high-frequency vibrational mode ($E_{2g}$).

Figure 44: (a) XPS survey plot of h-BN deposited by PECVD (b) B1s peak (c) N1s peak.

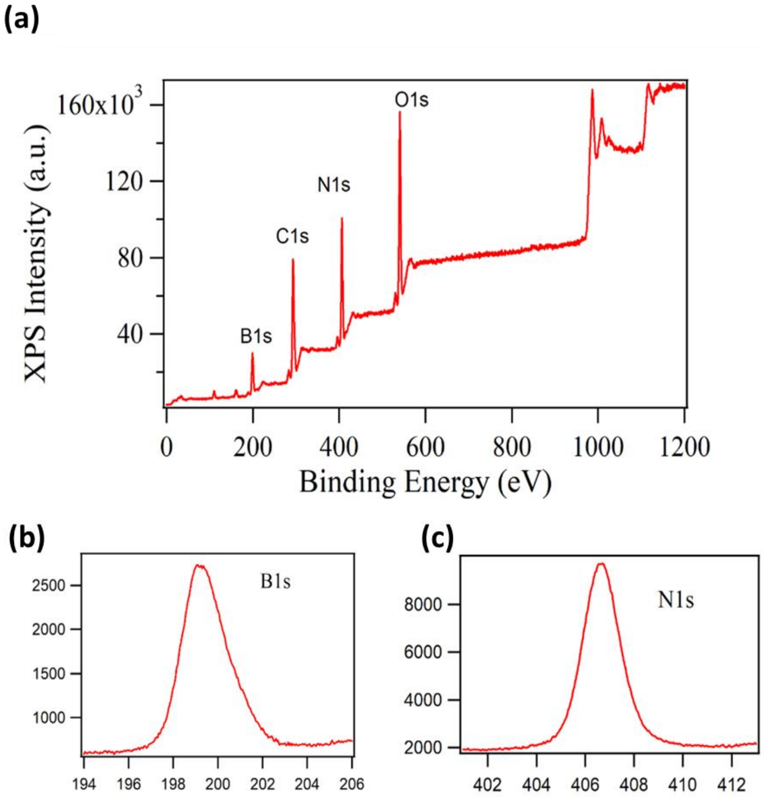

X-ray photoemission spectroscopy was also used to analyze the synthesized 2D films. XPS analysis was performed using a VG Scientific MultiLab 3000 ultra-high vacuum surface analysis system with a dual-anode (Mg/Al) x-ray source, a CLAM4 hemispherical electron energy analyzer. and at a base pressure of $10^{-9}$ Torr was used for X-ray photoelectron spectroscopy (XPS) measurements. The measurements were conducted using a non-monochromatized Al Kα x-ray radiation (hν ≈ 1486.6 eV) at a base pressure of $10^{-9}$ Torr. The C-C ($sp^2$) peak of adventitious carbon at 284.5 eV was used for the binding energy

(BE) calibration. Figure 44 shows the X-ray photo-emission spectroscopy (XPS) results of h-BN grown by PECVD. The survey spectrum shown in Figure 44(a) clearly shows the presence of boron and nitrogen with the appearance of XPS peaks corresponding to B1s and N1s core electrons. As expected, an additional peak corresponding to O1s core electrons is also present in the survey spectrum. The unexpected peak characteristic of C1s core electrons is presumably due to the carbon contamination resulting from previous synthesis of graphene in the same reactor. Figures 44 (b) and (c) show the high-resolution individual peaks, B1s and N1s at the binding energies (BE) 198.6 eV and 406.8 eV, respectively[294]. These BEs are consistent with the reported XPS characteristic values for h-BN. Stoichiometry evaluation based on B1s and N1s peak areas gives B/N ratio of 1.08, suggesting equal composition of B and N elements in h- BN.

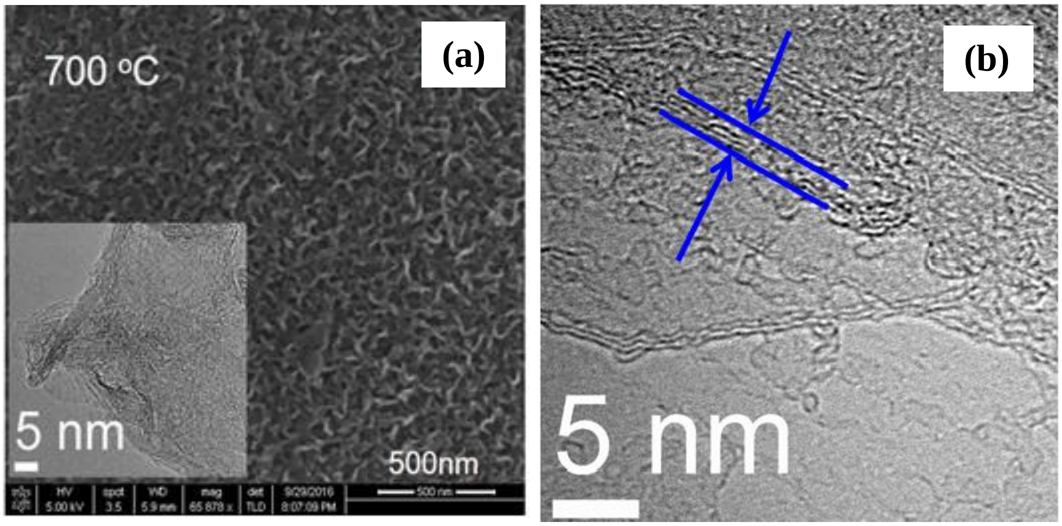

Figure 45. (a) SEM image of the graphene nanowalls directly deposited on Si/SiO2 substrate at 700 $^0$C. The inset represents the HRTEM image of the sample (b) Enlarged HRTEM of graphene nanowalls showing 4-5 graphene layers.

Plasma-enhances CVD(PECVD) usually result in vertically standing few layers graphene (graphene nanowalls). They form a self-supported network of wall structures with thicknesses ranging from single to few graphene layers depending on the growth temperature and the growth time. Figure 45(a) shows SEM image of a graphene nanowalls sample grown at 700 °C using PECVD. Figure 45 (b)shows a HRTEM of the sample showing 4-5 graphene layers.

### 4.4.1 AFM characterization:

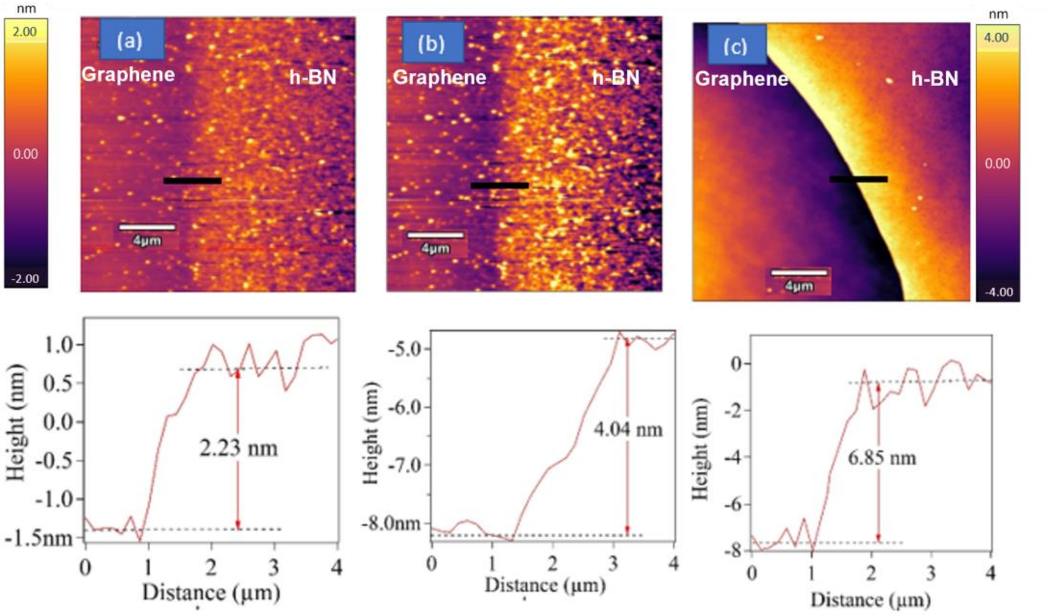

Figure 45: AFM images for the three samples with different h-BN thickness (top panel) with height profiles (bottom panel). The color map in the left represents both images (a) and (b) while the color map in the right represents the image (c).

Figure 46 shows AFM images (of the surface) and height profile of each sample taken by an Asylum Research MFP-3D-Bio atomic force microscope. The AFM topography images were obtained in tapping mode in air with the aid of Si tips with a typical tip radius of 25 nm, tip length of ∼240 µm, spring constant range 1.8−12.5 N/m, and frequency range 58−97 kHz. The average thicknesses of samples were found to be 2.23, 4.04, and 6.85 nm respectively.

### 4.4.2. I-V Characteristics of The Three Samples with Different h-BN Thickness:

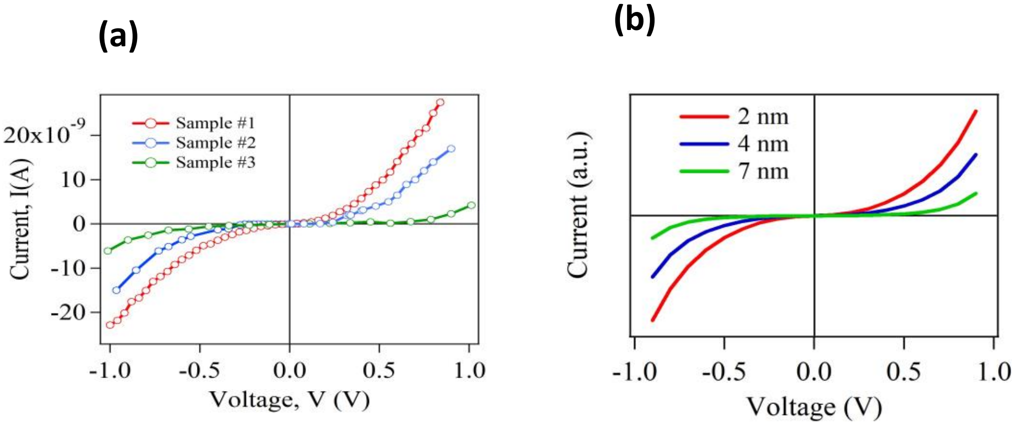

Figure 46: (a) I-V characteristics of Graphene/h-BN/Graphene tunnel junctions for varying h-BN thicknesses (b) Theoretical simulation of the tunneling current for varying barrier thicknesses.

Figure 47 shows the tunneling I-V characteristic curves of three Graphene/h-BN/Graphene based single tunnel junctions with varying h-BN thicknesses (tunnel barrier widths). All three curves show exponential dependence of the current (I) with the bias voltage (V) at higher voltages. We also calculated the slope of the linear range of each curve about V=0 to evaluate the zero-bias conductivity (ZBC). The ZBC of the samples were found to be 1.760 GΩ$^{-1}$, 0.356 GΩ$^{-1}$ and 0.025 GΩ$^{-1}$ as the h-BN barrier width increases from the thinnest to the thickest, revealing the exponential dependence of the ZBC with the barrier width[295].

We will simulate the tunneling current using the following formalism. The tunneling current, *I* can be expressed as[257]**,**

$$I = g_s g_v e \sum_{\alpha,\beta} \left\{ \frac{1}{\tau_{\alpha\beta}} f_T(E_\alpha)[1 - f_B(E_\beta)] - \frac{1}{\tau_{\beta\alpha}} f_R(E_\beta)[1 - f_T(E_\alpha)] \right\}, \qquad (1)$$

where, $\alpha$ and $\beta$ represent the top (*T*) and bottom (*B*) electrodes with energies, $E_\alpha$ and $E_\beta$ respectively, $g_s=2$ is the spin degeneracy and $g_v$ is the valley degeneracy, $\tau_{\alpha\beta}$ and $\tau_{\beta\alpha}$ are the tunneling rates for electrons tunneling from top → bottom and bottom → top respectively and $f_T$ and $f_B$ are Fermi occupation factor for the top and bottom electrodes given by,

$$f_T(E) = [1 + e^{\left[\frac{E-\mu_T}{k_B T}\right]}]^{-1} \text{ and } f_B(E) = [1 + e^{\left[\frac{E-\mu_B}{k_B T}\right]}]^{-1}. \quad (2)$$

The tunneling current can be simplified as**,**

$$I \propto \int_{\mu}^{\mu+eV} DOS_T(E)DOS_B(E-eV)T(E)[f(E)-f(E-eV)]dE \quad (3)$$

Where, *f(E)* is the Fermi distribution function, $DOS_{T(B)}(E)$ is the density of states in the top (bottom) electrode, T(E) is the transmission probability at the given energy[296]. Figure 5(b) shows the tunneling current calculated for varying h-BN thicknesses according to equation (3). In the simulation, we assumed relativistic density of states of graphene, DOS(E) ~ |E| and restricted the energy integral limits μ and μ+eV, where μ is the chemical potential. It is also assumed that there is no in-plane momentum conservation, The calculated tunneling currents qualitatively agree very well with the experimental results for appropriate h-BN thicknesses.

Figure.48. (a)Probe Station. (b)Keithley22000Semiconductor Analyzer. (c)Close Cycle Refrigerator and Sample Mount for Low Temperature Measurements with The Magnet

## 4.4. Low Temperature Measurement of Graphene and All Three Quantum Junctions:

### 4.4.1.I-V Characteristics of Graphene Sample:

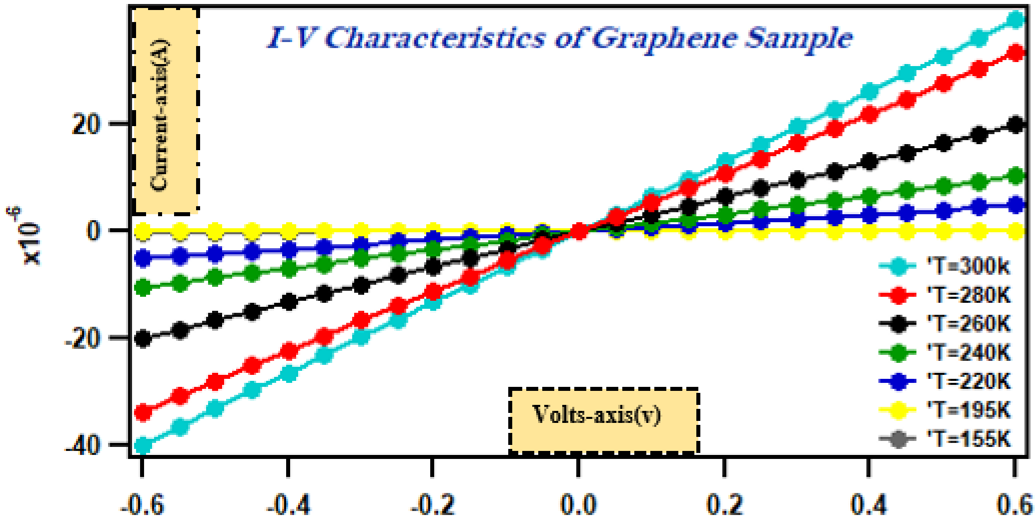

Figure 47: Pristine Graphene Sample at Various Temperature

A few layers of graphene are used to explore the temperature dependence of electrical transport experiment[297]. The temperature dependency of a temperature measurement of a few layers of graphene is shown in Figure 49. The relative difference in resistance is explained by temperature changes from 300 K to 155 K.

The electrical resistance of three or four layers of graphene as a function of temperature is shown in Figure 49. The results demonstrate that when the temperature is reduced, the graphene structure's resistance increases in a monotonic manner.

Charge impurities increase the density of localized states, causing resistance[298]. As the temperature is reduced from 300 to 155 K, the resistance of the graphene layers increases considerably. We hypothesize that these irregular electrical properties exist in graphene's unique band structure at the Fermi level due to the complexity of the few graphene layers band structure[299]. The resulting I-V curve is extremely linear and precisely depicts the influence of temperature on our graphene sample's resistance.

### 4.4.2.I-V Characteristics of Direct Quantum Tunneling of all three different Junctions:

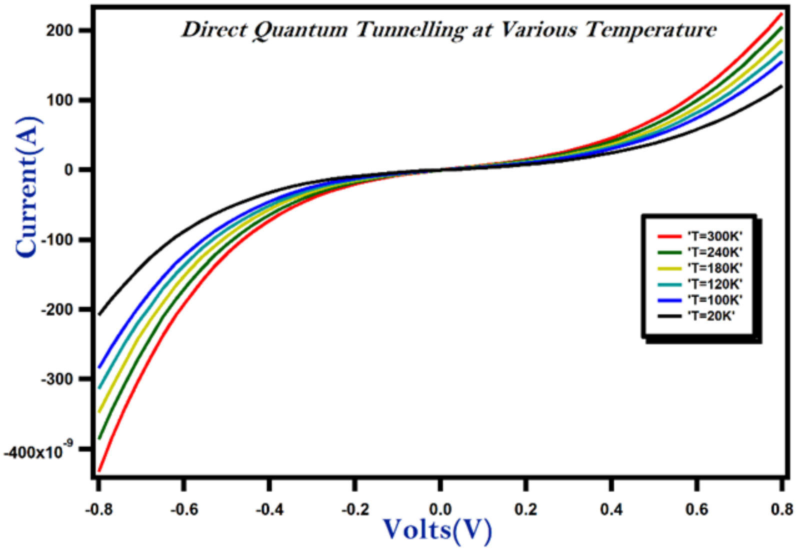

Figure 50: I-V Curve at various temperature of direct quantum junction 1.

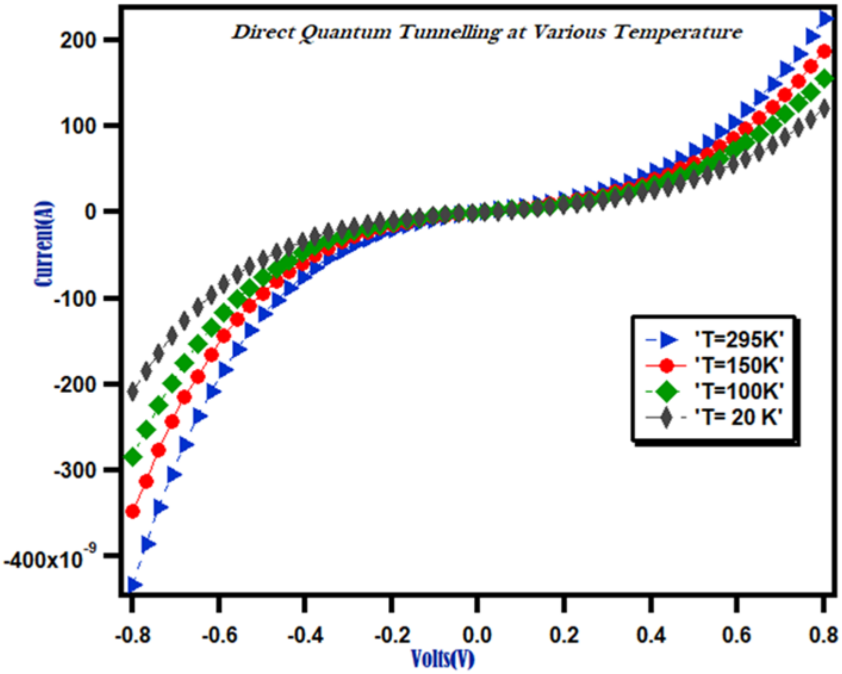

Figure 51: I-V Curve at various temperature of direct quantum junction 2.

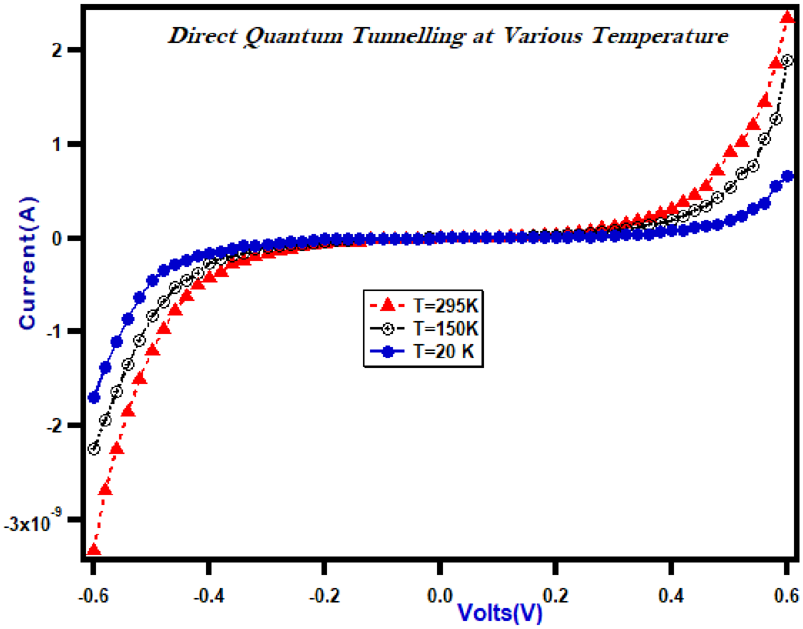

Figure 52: I-V Curve at various temperature of direct quantum junction 3.

As described in figures 50,51, and 52, in the preceding section of this chapter, three different quantum junctions with various h-BN thicknesses were synthesized, and I-V curve measurements were performed at room temperature alone (using The Keithley Semiconductor Analyzer System) for all of the manufactured junctions. As can be seen in the above figurers, three chip carriers were established for low temperature experiments by connecting the top and bottom graphene layers with two copper wires to transfer $SiO_2$ substrates with junctions to investigate I-V characteristics at various temperatures. A chip carrier carrying a single quantum junction sample was transferred to a closed cycled refrigerator (Janis Research Co. CCS-350ST-H) capable of cooling to a base temperature of 10 K for low-temperature measurement. A Lakeshore type EM4- CV 4-in. gap, Horizontal Field electromagnet surrounds the sample-containing refrigerator column, providing a magnetic field that may be swept between 1 and +1. The voltage bias was changed between ambient and extremely low temperatures to create current tunneling through the h-BN layer (very thin insulating barrier in nanoscale). To allow electrons to pass through, the thickness of the insulating layer was selected. At the nanoscale, h-BN insulating layers were fabricated as thin as possible while yet allowing an electron to pass through[300]. Modifications in plasma power and development time were applied to alter the thickness. In a single quantum junction, free carriers (electrons) can flow via the conduction channel[301]. Electrons must cross a potential barrier at the junctions when passing between two graphene layers. The variation in I-V characteristics and resistance observed when using a Helium gas compressor to cool the samples is most likely due to variations in the width of each junction's surface depletion layer, as well as the height of potential barriers produced at contacted junctions between two graphene layers[302, 303]. Since electron kinetic energy decreases when material temperature decreases, reaction time may be shortened as a result of these two reasons. When the sample was cooled from 300 Kelvin to a low temperature, data was also collected (Up to 20 Kelvin). Consequently, the I-V properties of the sample altered predictably and dramatically as it cooled.

### 4.4.3. Magnetic field dependent I-V Characteristics of Direct Quantum Tunnelling

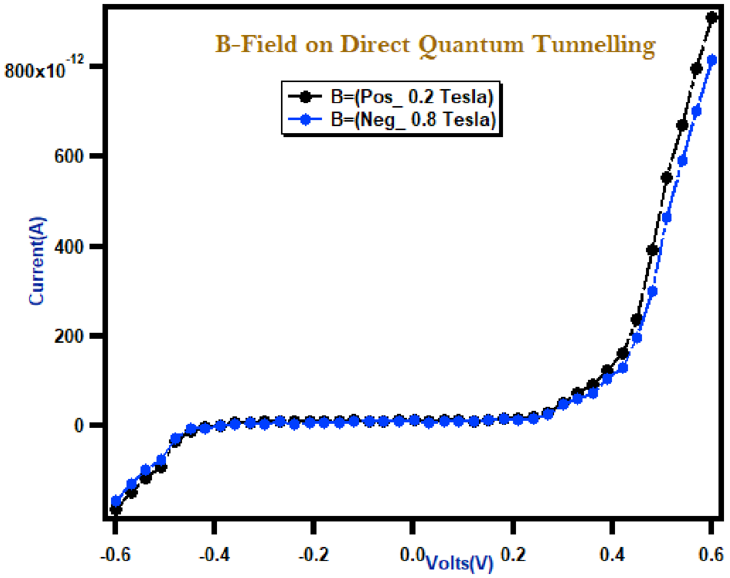

Figure 53: I-V Characteristics of Direct Quantum Tunnelling at different applied Magnetic Fields

From Figure 53. The effects of an external magnetic field on potential barriers[304] are investigated in order to evaluate the influence of external magnetic fields (from negative to positive Tesla) on the I-V properties of the GIG structure at low temperatures (20K). When the temperature went below 20 K at a given voltage, the current decreased monotonically. This is because the structure of the junction has changed, resulting in a larger junction resistance[305]. The charge carrier density dropped when the potential barrier was increased at extremely low temperatures[306]. Increased applied magnetic fields cause primarily a decrease in carrier mobility and an increase in carrier effective mass. As the effective mass grows and the current decreases, the rate of carrier penetration through the potential barrier decreases. The number of electrons flowing from the bottom to the top electrode decreases as the collision rate increases, while the resistance increases.

## Conclusion:

In conclusion, we have demonstrated a direct method for fabricating devices with atomically thin tunnel barriers by direct deposition of h-BN with graphene active electrode layers on a Si/$SiO_2$ substrate using a PECVD method. Current-voltage measurements for different BN thicknesses and equally doped graphene based single barrier tunneling shows linear I-V characteristics at low bias but shows an exponential dependence at higher bias. Our measurements of the electron tunnel current through the barrier demonstrate that the h-BN films act as a good tunnel barrier. Furthermore, the difference in I-V characteristics and resistance observed when using a Helium gas compressor to cool the samples is most likely due to differences in the width of each junction's surface depletion layer, as well as the height of potential barriers produced at contacted junctions between two graphene layers. By applying magnetic fields, a decrease in carrier mobility and an increase in carrier effective mass has been observed. As the effective mass grows and the current decreases, the rate of carrier penetration through the potential barrier decreases. The number of electrons flowing from the bottom to the top electrode decreases as the collision rate increases, while the resistance increases.

# CHAPTER 05

# RESONANT TUNNELING WITH UNEQUAL DOPING OF TOP AND BOTTOM GRAPHENE LAYERS

## 5.1 Introduction:

Here the same sequential processes were used for fabricating p-graphene/h-BN/n-graphene based device[307]. First n type graphene (n-graphene) was deposited using PECVD using $NH_3$ in addition to $CH_4$ on a $Si/SiO_2$ substrate. Next, through a mask with a circular opening, h-BN was deposited on previously deposited graphene again using PECVD with ammonia borane as described before. Finally, the third p-type graphene (p-graphene) layer was deposited using another mask with a smaller opening.

The thermopower of p and n-graphene was measured using the analog-subtraction method developed in our laboratory. Two miniature thermocouples (Chromel (KP)/ Au−7 at. % Fe (Au/Fe); 100 μm diameter) and a resistive heater were used for the measurements. The as deposited graphene was found to be p-type with the thermopower of +60 μV/K. In order to n-dope graphene, it was exposed to hydrazine.Figure 54(a) shows the thermopower response of graphene when exposed to hydrazine at room temperature. The downward arrows indicate where hydrazine was introduced to a pressure of 3, 7 and 10 Torr. After the first exposure to 3 Torr, the thermopower decreased and turned negative and eventually saturated at a value ~10 μV/K. Further exposure to the pressures of 7 Torr and 10 Torr resulted in saturating the thermopower at ~ -55 and ~-80 μV/K respectively. The n-doped graphene with ammonia shows the thermopower~-250μV.

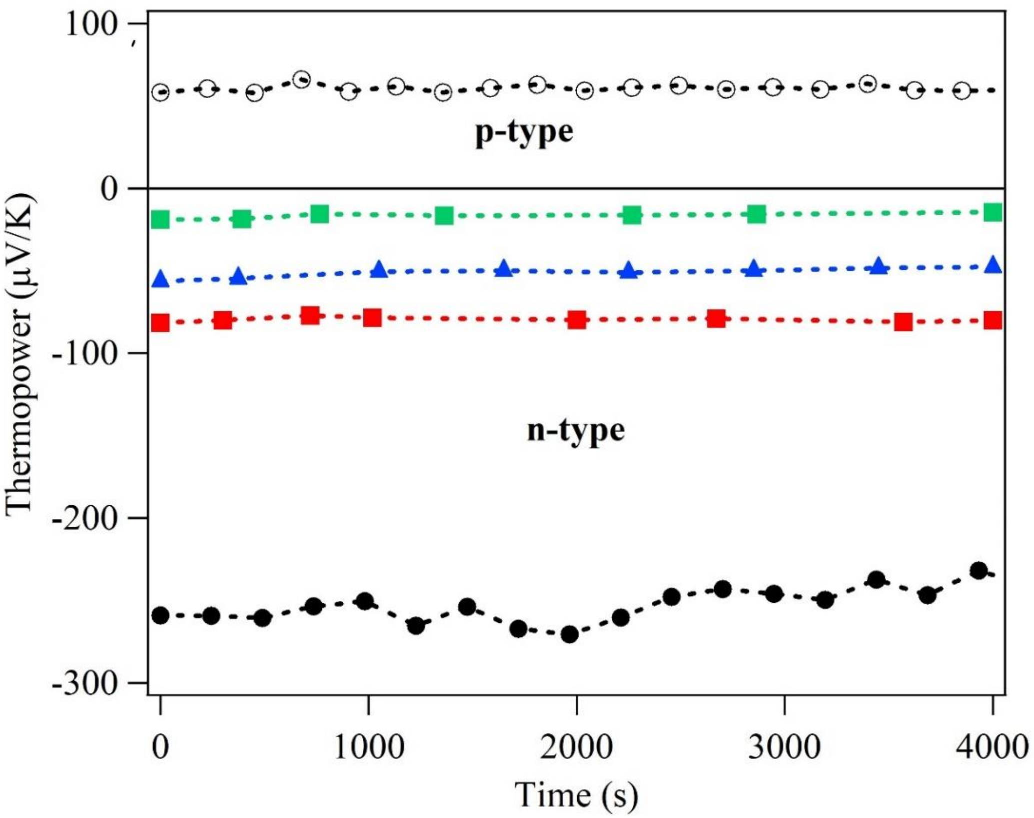

Figure 54: Thermopower of p and n-graphene (3 different degree of nitrogenation) as a function of time.

### 5.2 The loop of P-type and N-type of graphene:

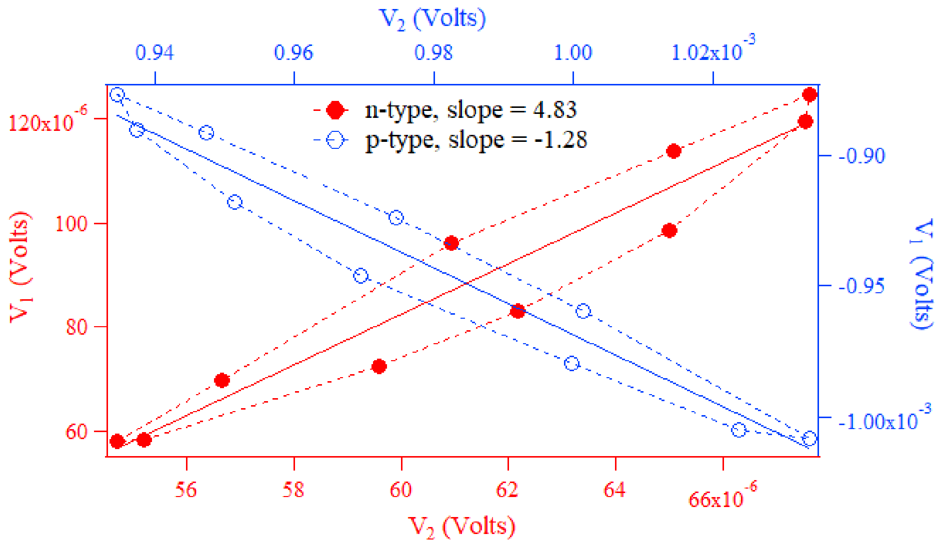

Figure 55. The loop resulting from the voltages from the analog-subtraction technique of the room temperature data of pristine (p-type) and n-doped graphene.

Figure 55. It shows both p and n-type of graphene loops with the solid line showing the linear fit. Slope was used to calculate the respective room temperature thermopower values of each sample. $V_1$ corresponds to the thermoelectric voltage ($\Delta V$) and $V_2$ corresponds to the temperature difference ($\Delta T$).

## 5.3 Results and Discussions:

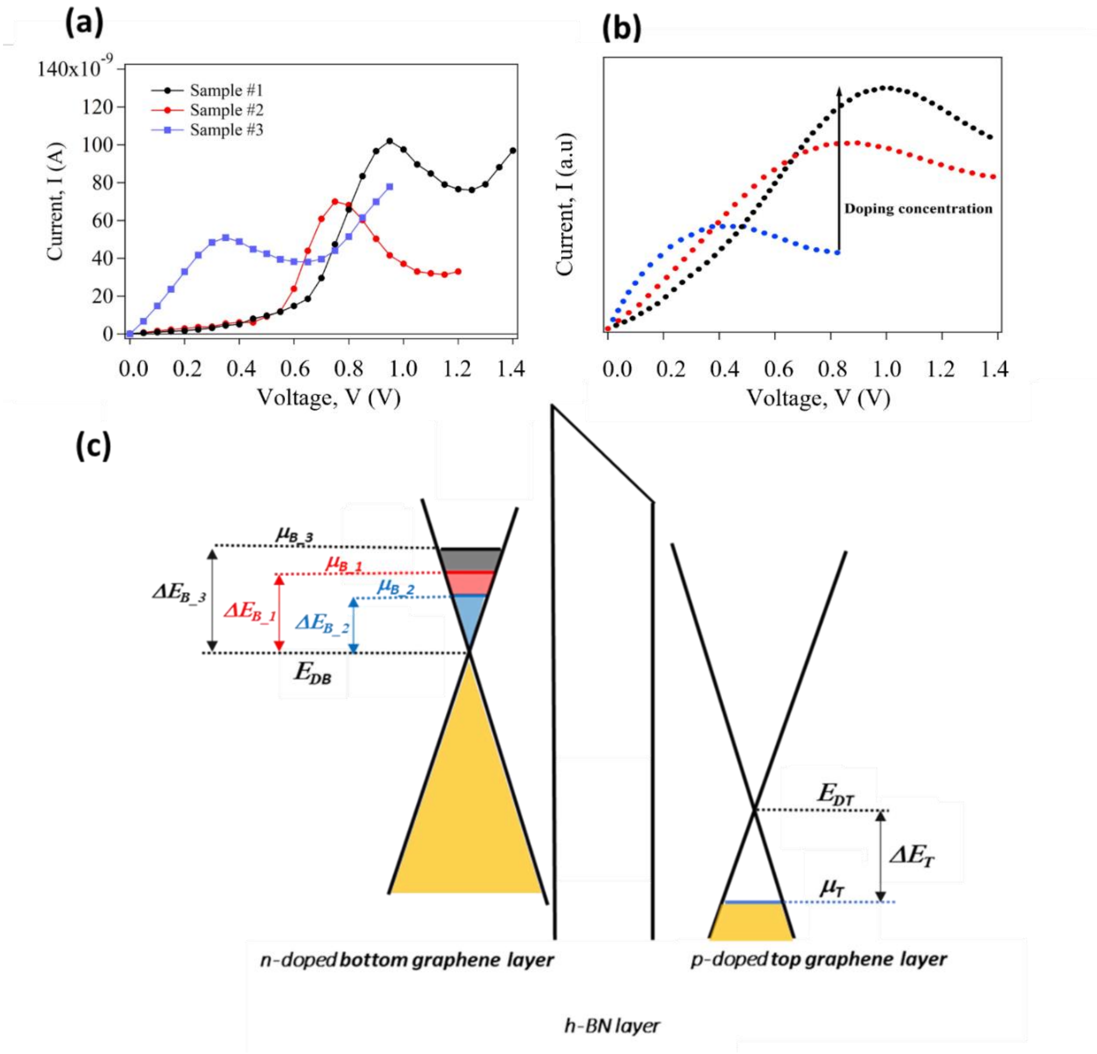

Figure 56: (a) I-V characteristics of p-Graphene/h-BN/n-Graphene tunnel samples with 3 different levels of n-doping. (b) Theoretical simulation (c) Band diagram for the resonant tunnelling junction with doped electrodes.

Figure 56 (a) shows the I-V characteristics of p-Graphene/h-BN/n-Graphene samples with 3 different levels of n-doping. The I-V curves of all three samples show the presence of a pronounced peak in the current corresponding to negative differential conductance (NDC) whose peak current value and the voltage value depend on the doping level of the n-layer.

It is assumed that the doping level of the p-layer is the same as it's due to the intrinsic doping presumably due to an electrochemically mediated charge transfer process[308] under the ambient conditions. It can be seen that the peak current and the peak voltage increase when the doping level of the n-layer increases. Figure 56(b) shows the Bardeen tunneling model including the effect of doping in both graphene electrodes. As shown in the inset to Figure 56 (c),  we assume that the top electrode is n-doped and the bottom electrode is p-doped, with chemical potentials $\mu_B = E_{DB} + \Delta E_B$ and $\mu_T = E_{DT} - \Delta E_T$ for specific $\Delta E_B$ and $\Delta E_T$ where $E_{DB}$ and $E_{DT}$ are the respective Dirac points[261, 309]. Both $\Delta E_B$ and $\Delta E_T$ depend not only on the doping of the graphene electrodes as described before, but also on the external bias voltage, V and the junction capacitance, C[310]. The resonant condition arises when $eV = \Delta E_B + \Delta E_T$. The relativistic density of states of n- and p- doped graphene, DOS(E) ~ $|E \pm (E_D - E_F)|$ respectively, was assumed, where $E_D$ is the Dirac point energy and $E_F$ is the Fermi energy as can be illustrated in figure a, b, and c.

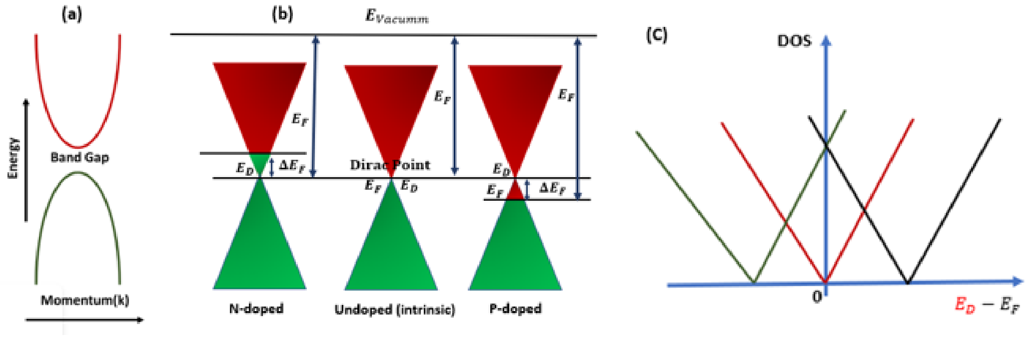

Figure 57:(a and b) as diagrams of band structures of all graphene types. (c)Density of states of n-type, undoped, and p-type graphene.

## 5.4 Conclusion:

In conclusion, a variety of devices including unequally doped graphene electrodes separated by a thin h-BN layer were also fabricated by using different doping methods of these materials for the upper and lower electrodes. The tunnelling devices consisting of unequally doped graphene with a single barrier shows resonant quantum tunneling with the presence of a pronounced peak in the current corresponding to negative differential conductance (NDC) whose peak current value and the voltage value depend on the doping levels. The results are explained according to the modified Bardeen tunneling model. According to our measurements, the electron tunnel current measured across the barrier demonstrates that h-BN films are effective tunnel barriers.

# CHAPTER 06

# DIRECT FABRICATION OF VERTICALLY STACKED DOUBLE BARRIER TUNNEL JUNCTIONS BASED ON GRAPHENE AND h-BN

## Resonant Tunneling of Double Barrier:

### 6.1 Introduction:

Due to their excellent performance in novel electronic, optoelectronic, and photovoltaic applications, two-dimensional (2D) materials such as graphene and hexagonal-boron nitride (h-BN among others, have attracted a great deal of interest[126, 311]. Because graphene is semimetal with a zero-band gap and h-BN is an insulator with a wide band gap, they both are undesirable for electronic application in their pristine forms. To overcome such constraints, researchers have attempted to stack combination of metallic (graphene, for example), insulating (h-BN, for example), and semiconducting (phosphorene and $MoS_2$ for example) 2D materials to enable functional devices[312]. This includes (I) incorporating functionality into such 2D structures, (ii) stacking them vertically or laterally, and (iii) integrating into nanocomposite to enhance efficiency and many inherent properties such as optical absorption etc[313].

It is desirable to use 2D materials in the next generation of functional devices owing to their following properties (i) only one-atom thick layers allowing faster electron conduction, (ii) stability at high temperatures[314], -layer dependent, adjustable band gap

and scalability in both synthesis and processing, enabling easy integration with existing technology etc. On the other hand, since the heterostructures are essential in the semiconductor industry, monolayers of novel 2D materials provide the foundation for design of heterostructures with a wide range of characteristics and applications. In recent years, numerous physical characteristics of van der Waals heterostructures have been investigated. Such heterostructures consist of monolayers of various 2D materials that are assembled either laterally (in-plane) or vertically (layer-by-layer)[315]. Lattice matching in these heterostructures is not that critical due to the van der Walls interlayer interaction. To achieve the maximum performances, the interface must be atomically sharp, and the junction can be as thin as two atomic layers. These vertical stacking differ significantly from typical 3D semiconductor heterostructures where each layer serves as both the bulk material and the sacrificial material with the surface, therefore lowering the amount of charge displacement inside each layer. Furthermore, using appropriate manufacturing thin-film methods, these structures can be made flexible and stable. Much research on graphene-2D materials heterostructures have been published in recent years[316], revealing new charge transport characteristics across the interface. Many groups produced vertical tunneling transistors with high on-off ratios and huge current densities using h-BN thin layers as tunneling barriers and graphene as one or both electrodes.

During standard device fabrication processes, surface impurities left behind by lithography steps, can be sensitive to 2D materials consisting of one or few atomic layers. Despite the fact that annealing methods have been shown to increase device performance, they do not always give consistent results. Lithography techniques of numerous types are frequently employed in various scientific and technological domains for the fabrication of functional devices. In traditional top-down lithography, costly equipment with predesigned masks and collimated light sources are used, resulting in expensive and time-consuming processing procedures. On the other hand, electron beam lithography defines nanoscale patterns without the use of a physical mask, but its high equipment cost and slow patterning speed limit its widespread use. In recent years, there has been a surge in the need for creating bottom-up lithography-free patterning methods. Alternative methods for producing regular nanoscale patterns without the need of a mask include laser interference and nanosphere lithography. Low-cost lithography-free manufacturing approaches have been described, for defining basic geometries without the need for resist processing, with higher device throughput. Above all, lithography-free procedures described above may be utilized by any individual who does not have access to a clean room facility.

A RF-PECVD technique was employed in this work to deposit graphene and h-BN directly on a substrate using simple shadow masks to isolate each layer. $CH_4$ gas was used as the carbon source to synthesize graphene, whereas ammonia borane was used to synthesize h-BN.

## 6.2 History of Resonant Tunneling:

Since the late 1950s, devices consisting of doped p-n junctions with thin oxide barriers (tunnel diodes) [262]and double barrier heterojunction devices based on quantum tunneling processes have been found using the negative differential resistance (NDR)[261]. Microwave/millimeter wave oscillators and high-speed logic devices/ switches have also discovered the use of NDR in their I-V characteristics. Previous research on resonant tunneling was confined to unequally doped two-dimensional electron gas (2DEG) systems based on coupled electron gas systems made up of closely spaced quantum wells made up of AlGaAs/GaAs heterostructures[317]. 2D–2D tunneling has recently been shown in graphene/insulator/graphene systems[318] due to graphene's two-dimensional structure. Here, we developed a straightforward way for constructing a quantum double barrier device using three graphene layers and two h-BN (insulation) layers layered vertically between each pair of graphene layers. The purpose of this research is to develop double barrier devices with resonant tunneling behavior from two thin layers of h-BN separating graphene layers using a lithography-free direct deposition approach. A resonant peak in tunnel current is predicted in double barrier tunneling at a voltage bias that matches the alignment of the band structures of the graphene layers[319]. Since periodic square well potentials occur in both permitted and forbidden energy zones, the traditional Kronig-Penney model predicts resonant tunneling of electrons in double barrier 2DEG systems. Within these energy ranges, electron transmission resonance may exist. The permitted energy values (minibands) in AlGaAs/GaAs superlattices created by Molecular Beam Epitaxy (MBE) have been found for device configurations with pre-defined well-widths and barrier-heights. To create comparable double-barrier structures, graphene and h-BN layers were progressively grown directly on Si/$SiO_2$ substrates using a PECVD process. Tunneling behavior was investigated by altering the thickness of the third graphene layer formed on the first h-BN layer.

### 6.3 Experiment Details and Results:

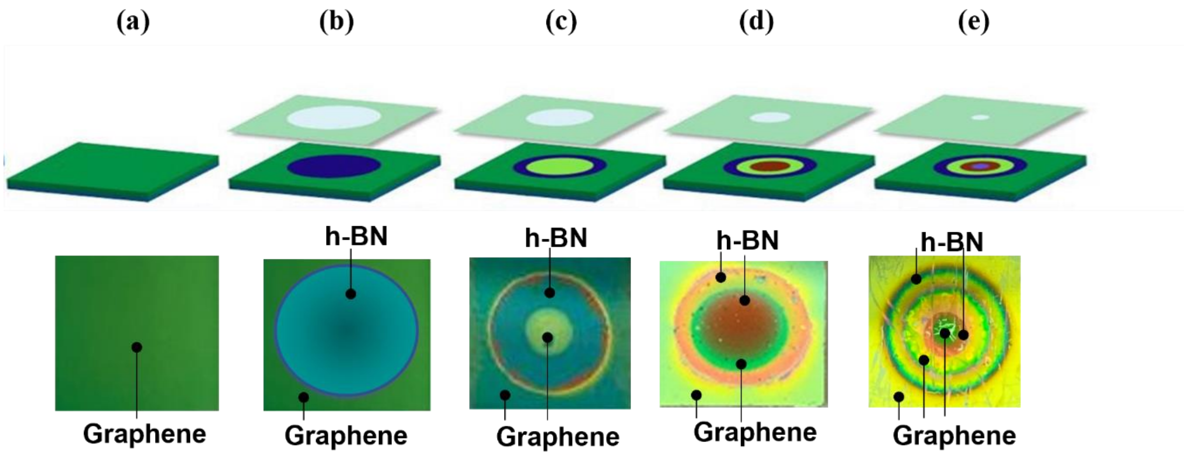

Figure 48:Double Quantum Junctions (Double Barrier)

Fig. 58 The fabrication steps of a Graphene/h-BN/Graphene tunnel junction device. The top raw depicts the schematic diagrams while the bottom represent the optical images of the sample after each step; (a) Si/SiO$_2$ substate completely coated with graphene (b) h-BN patch defined on the bottom graphene layer using a circular mask (**9** mm diameter) (c) second graphene layer deposited on the first h-BN patch using a circular mask (**6** mm diameter) (d) ) second h-BN patch defined on the second graphene layer using a circular mask (**4** mm diameter) (e) final graphene layer deposited on the second h-BN layer using a circular mask (**2**mm diameter).

Fig. 58 shows the sequential processes of fabricating graphene/h-BN/graphene/h-BN/graphene-based device. First, graphene was deposited on a Si/SiO$_2$ substrate using a PECVD technique developed in our laboratory. A custom-made split ring radiofrequency (13.56 MHz, Max. power 600 W) system was used for plasma generation. The substrates were thoroughly cleaned prior to the synthesis of the first graphene layer on the entire Si/SiO$_2$ substrate. The substrates were sonicated in acetone for 10 min and dried in nitrogen before placing inside the quartz reactor. Then the reactor was evacuated to a pressure lower than ~5 mTorr before heating the furnace to 650 °C in a flowing gas stream: Ar/$H_2$ (40 vol % argon, 60 vol % $H_2$) at a flow rate of ~20 standard cubic centimeter per minute (sccm). The pressure was maintained at ~200 mTorr using a pressure regulator during the heating. A hydrogen plasma was ignited at a power of 50 W for 20 minutes after the heating step for further reducing and cleaning of the surface. Next, ultra-pure $CH_4$ (99.9%) was introduced at a flow rate of ~3 sccm into the growth chamber immediately after switching off the Ar/$H_2$. Then the ammonia plasm was generated at a power of ~80 W and maintained for 30 ~ 120 minutes. The sample was then cooled down to room temperature at a rate of 25 °C/min.

Next, h-BN was directly deposited on the previously deposited graphene layer, again using the same PECVD technique, but with ammonia borane (with 97% purity**)** as the source material[320]. During the deposition of this h-BN layer, the substrate with previously deposited graphene layer was covered with a circular shadow mask was placed inside the reactor at a proper position inside the reactor. A ceramic boat containing solid ammonia borane was placed between the plasma reactor and the furnace. A heat belt wrapped over the quartz tube covering the ceramic boat was employed with a controlled power supply to sublime borane ammonia. As before, the reactor was evacuated to a pressure lower than ~5 mTorr and gradually heated to 750 °C in a gas stream: Ar/$H_2$ (40 vol % argon, 60 vol % $H_2$) at a flow rate of ~50 sccm. Next, the ceramic boat was heated gradually from room temperature to 180 °C and a plasma was ignited at 100 W and maintained for 45 minutes. Then the reactor was cooled down to room temperature at a rate 25 °C/min. Next, another graphene layer was deposited on the already deposited h-BN layer using $CH_4$ plasma using another mask with a smaller opening. This was followed by the subsequent h-BN layer and the final graphene layers using shadow masks with gradually deceasing openings. Fig. 58 shows each step of the device fabrication. The top raw represents schematic diagrams while the bottom raw show the optical images of the sample after each step; (a) Si/$SiO_2$ substate completely coated with graphene (b) h-BN patch defined on the bottom graphene layer using a circular mask (9 mm diameter) (c) second graphene layer deposited on the first h-BN patch using a circular mask (6 mm diameter) (d) ) second h-BN patch defined on the second graphene layer using a circular mask (4 mm diameter) (e) final graphene layer deposited on the second h-BN layer using a circular mask (2 mm diameter). We kept the thickness of the h-BN layers and the thickness of the first and the last graphene layers constant. Only the thickness of the second graphene layer was varied in order to systematically change the well width.

## 6.4Characterization:

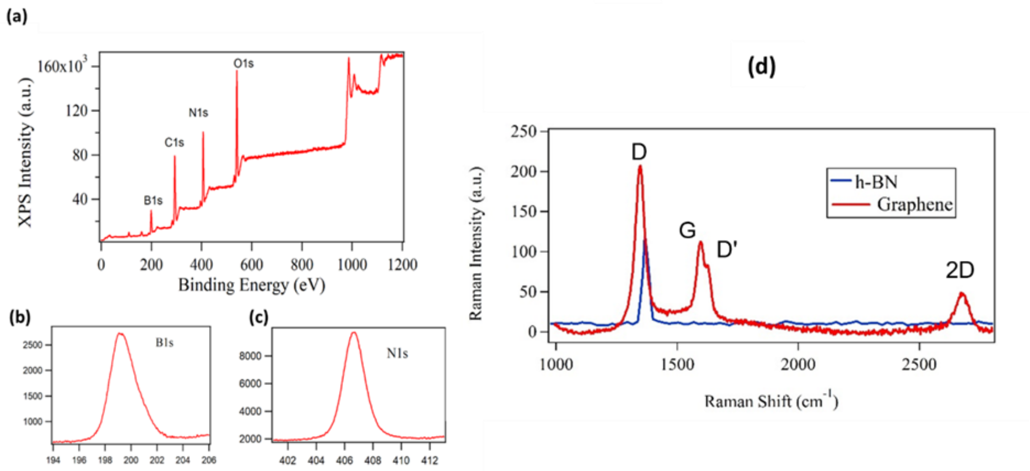

Figure 59**:** (a) PECVD-deposited h-BN XPS survey map; (b, c) XPS individual peak of B1s and N1s; and (d) graphene and h-BN Raman spectra recorded using a Renishaw InVia Raman spectrometer with a 632 nm laser excitation**.**

Using a VG scientific MultiLab 3000 ultra-high vacuum surface analysis system equipped with a twin-anode (Mg/Al) X-ray source and a CLAM4 hemispherical electron energy analyzer, the X-ray photoemission spectra (XPS) of h-BN deposited by PECVD were recorded at a base pressure of $10^{-9}$ Torr as shown in Fig. 59(a, b, c). The survey spectra in Fig. 59(a) shows peaks matches to B1s and N1s core electrons. The peaks representing C1s and O1s core electrons are also detected as expected in the spectra. C1 is primarily due to residual carbon contamination in the reactor from previously growth of graphene. As shown in Figure 59(b, c), the binding energies of the B1s and N1 are 198.6 eV and 406.8 eV respectively which is the same as the reported h-BN XPS characteristic lines. Based on XPS calculations, stoichiometry measurements reveal a B / N ratio of 1.08, indicating that the B and N components are approximately equally abundant.

A Renishaw inVia spectrometer with an 1800 line/mm grating and a charge-coupled device (CCD) detector with a 647 nm laser excitation was used to create the graphene and h-BN Raman spectra in Fig. 58 (d) with a spectral resolution of more [321]than 1 $cm^{-1}$. The D, G, D', and 2D bands of graphene have peaks of 1350 $cm^{-1}$, 1590 $cm^{-1}$, 1630 $cm^{-1}$, and 2600 $cm^{-1}$ respectively[321]. The D (1350 $cm^{-1}$) band, often refers as the disorder band, is commonly associated with defects of graphene. The G band (1590 $cm^{-1}$) is the main in-plane vibrational mode containing the sp2 hybridized carbon atoms of the graphene sheet. In graphene sheets, the D`-band (1630 $cm^{-1}$) is used to detect edge defects and structural disorders The 2D band (also known as the G' band) (~2690 $cm^{-1}$), is the second-order overtone of the D band corresponding to a two-phonon lattice vibrational process. The Raman spectrum of h-BN consisting of a peak at ~1380 $cm^{-1}$ is assigned to the high-frequency vibrational mode ($E_{2g}$) of B-N bonds.

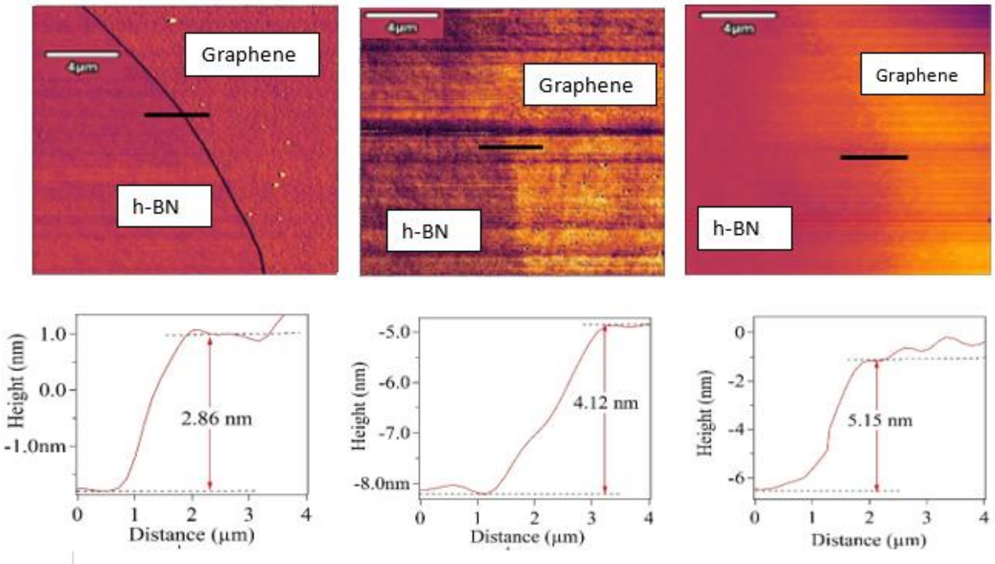

Figure 60**:** AFM surface images (top row) and height profile (bottom row) of the second graphene layer with varying thicknesses deposited on the first h-BN layer.

Fig.60 show the AFM images of the second graphene layer (with varying thickness) deposited on the first h-BN layer taken by an Asylum Research MFP-3D-Bio atomic force microscope. The AFM images were acquired in tapping mode configuration in air using Si tips with a typical tip radius of 25 nm, tip length of ∼240 µm, spring constant range 1.8−12.5 N/m, and  the frequency range of 58−97 kHz (Asylum Research probe, Model ASYELEC.01- R2). The AFM images shown in the top row of Fig.59show the surface images while the bottom row shows the height profile of each sample. The average thicknesses of the well width (second graphene layer on the first h-BN layer) of samples were found to be 2.86, 4.12, and 5.15 nm respectively.

## 6.5 Results and Discussions:

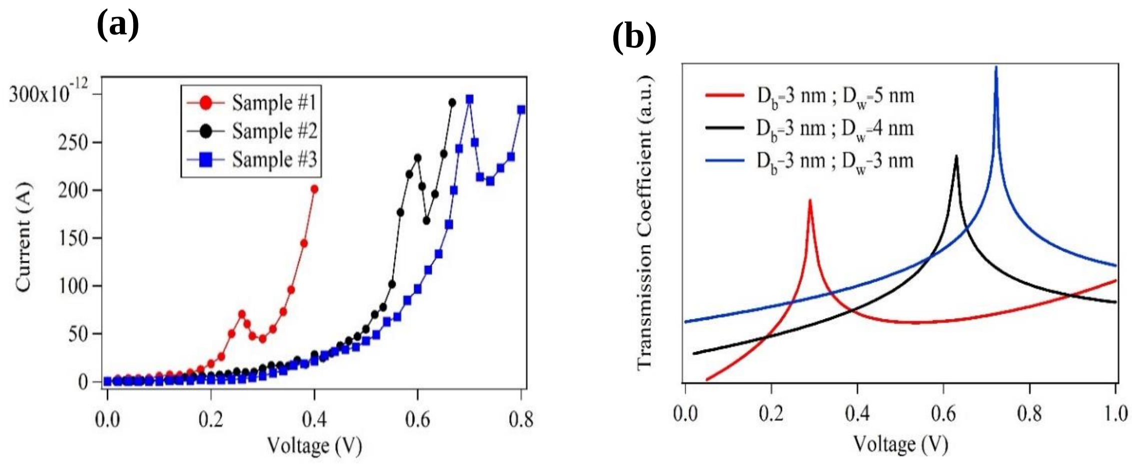

Figure 61**:** (a) I-V characteristics of double barrier tunnel junctions for varying DB well width, $D_w$ (b**)** Theoretical simulation of the transmission coefficient for the double well structure

Fig. 61 (a) Double barrier tunneling[322] intersection experiments were performed using graphene/h-BN/Graphene/h-BN/Graphene with three various DB well widths, Dw. After attaching electrical wires to the bottom and top graphene layers, the I-V characteristics were evaluated at room temperature using a Keithley 4200A-SCS Boundary Analyzer. When compared to negative differential conductance (NDC), the I-V bends in all three cases demonstrate the presence of an expanded top in the current.

## 6.6 The Diagram of The Double Barrier:

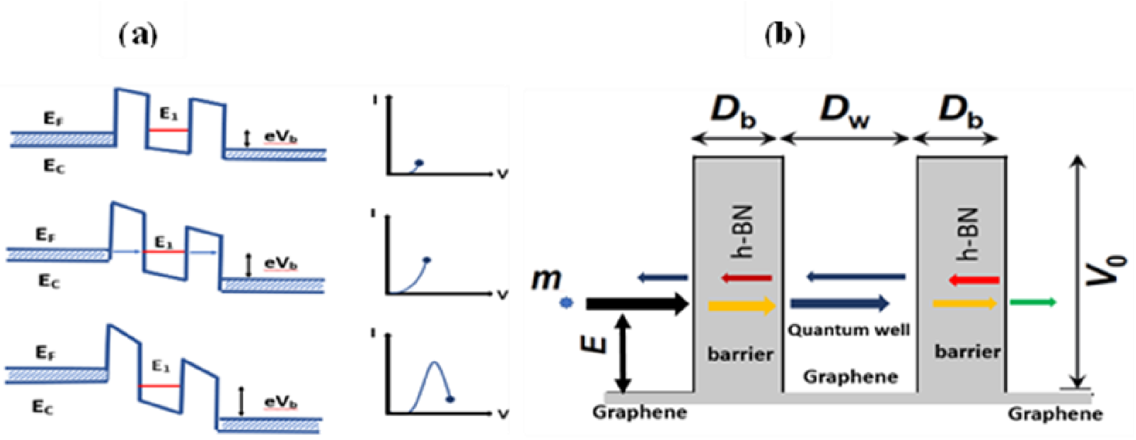

Figure 62**:** (a) The modification of the band-structure and the resulting I-V characteristics for a double –barrier structure for different voltage bias conditions **(b)** Schematic representation of the double barrier consisting of 3 graphene layers and 2 h-BN barrier layers.

The resonance behavior, as can be seen in Fig. 62, may be qualitatively explained by visualizing an electron projected onto two finite-height and-width barriers, with the incoming electron's energy, E, being lower than the barriers', $V_0$ (E< $V_0$) in Fig.62(b). The quantum mechanical ideas behind the general shape of the I-V curve of a double barrier structure may be appreciated using the schematic in Fig. 62(a). To simplify matters, the quantum well is believed to have only one limit (quasi) state energy level $E_1$. If the entire energy and momentum of the electrons in the plane of the heterojunctions are retained, only electrons with energy $E_1$ equal to $E_1$ have a reasonable chance of passing through the structure. In contrast to the electron energy level on the left, the quasi-bound level decreases when the bias voltage, $V_b$, increases from zero. The tunneling current increases as the number of electrons in the left with $E_F = E_1$ increases. When the resonant level coincides with the left-hand conduction band edge, it approaches a voltage peak. When $E_F = E_1$, no more electrons are available at higher voltages, resulting in a decrease in current and a negative differential resistance on the I-V curve (NDR). This phenomenon may be quantified using the quantum mechanical double barrier tunneling model[323]. Analytic solutions to Schrödinger's equation may be achieved with the right boundary conditions in each segment of the system seen in Fig. 62. (b). Again, consider an electron impacting with two finite-height V0 and Db barriers, where the electron's energy, E, is smaller than the barriers' energy, $V_0$, resulting in E $< V_0$. When a charged particle collides with a potential barrier, it either reflects or transmits. The transmission coefficient, t, is calculated precisely as a function of barrier height ($V_0$), barrier width ($D_b$), and well width ($D_w$). As it can be derived in section 6.7 below,

## 6.7 Transmission coefficients of Quantum Resonant double-barrier tunneling

For each region of interest, the transmission coefficients [324]are computed by matching the solutions to the one-dimensional, time independent Schrodinger equation in position space[325]:

$$\left[\frac{-\hbar^2}{2m}\frac{d^2}{dx^2} + V_{(x)}\right]\psi(x) = E\psi(x) \tag{1}$$

where h is in cgs units and m is the mass of an electron. We assume a piecewise constant potential in this model. In the places where $V_{(x)} = 0$, the equation simplifies to $V_{(x)} = 0$.

$$\frac{-\hbar^2}{2m}\frac{d^2\psi}{dx^2} = E\psi \tag{2}$$

$$\frac{d^2\psi}{dx^2} = -\frac{2mE\psi}{\hbar^2}$$

$$\frac{d^2\psi}{dx^2}=-k^2\psi$$

Where $k = \sqrt{\frac{2mE}{\hbar^2}}$ , As a result, we get a second-order differential equation with two linearly independent fully oscillatory solutions, and the general solution is $\psi(x) = A\ Sin(kx) + B\ Cos(Kx)\ or\ \psi(x) = Ae^{ikx} + Be^{-ikx}$ Schrodinger's equation is transformed into Schrodinger's equation with a nonzero constant potential of magnitude $V_0$.

$$\frac{-\hbar^2}{2m}\frac{d^2\psi}{dx^2} = (E - V_0)\psi$$

$$\frac{d^2\psi}{dx^2} = \frac{2m(V_0-E)}{\hbar^2}\psi \qquad (3)$$

So, it can be written as: $\frac{d^2\psi}{dx^2} = P^2\ \psi$

$P = \sqrt{\frac{2m(V_0-E)}{\hbar^2}}$, so, in this case, the rising and falling exponentials are two linearly independent solutions, and the general solution is $\psi(x) = Ce^{qx} + De^{-qx}$ .Then, taking into account all of the model's regions and assuming $V_0$ > E,

$$\psi(x) = Ae^{ikx} + Be^{-ikx}, \text{ x<a}$$

$$\psi(x) = Ae^{ikx} + Be^{-ikx}, \text{ x<a}$$

$$\psi(x) = Ce^{qx} + De^{-qx}, \text{a<x<b} \qquad (4)$$

$$\psi(x) = Fe^{px} + Ge^{-px}, \text{c<x<d}$$

$$\psi(x) = Re^{ikx} + He^{-ikx}, \text{ x<d}$$

Where q and p can be written as :

$$\text{(a)}\ P = \sqrt{\frac{2m(V_2 - E)}{\hbar^2}}$$

$$\text{(b)}\ q = \sqrt{\frac{2m(V_1 - E)}{\hbar^2}}$$

We must first understand the probability current before we can compute the transmission coefficients using our barrier sequence. To put it another way, when a probability flow, or current, enters or exits a certain geographical location, the probability of detecting an electron varies. It’s known as the current. As a result, the magnitudes of potential barriers on the left and right might be presented differently.

$$j_x = \frac{\hbar}{2mi}\left(\psi^* \ \frac{\partial\psi}{\partial x} - \psi \ \frac{\partial\psi^*}{\partial x}\right) \qquad (5)$$

where $\psi^*$ is the wave function's complex conjugate of the wave function $\psi$.

Last but not least, the transmission coefficient is indicated by the following formula: (T=$\dot{J}_t/j_i$). T is a ratio of the squared moduli of the relevant coefficients from the initial wavefunctions, since the potential before and after our model's sequence of barriers is the same =for both x < a and x > d-T.

Because the potential before and after the series of barriers is the same in the model $V = 0$ for both x a and x > d —T reduces to a ratio of the squared moduli of the relevant coefficients from the initial wavefunctions[326].

$T = \frac{|A|^2}{|F|^2}$ incident electrons from the left (6)

$T = \frac{|B|^2}{|K|^2}$ incident electrons from the right (7)

$$0 < E < V_0;\ k = \frac{\sqrt{2mE}}{\hbar};\ P = \frac{\sqrt{2m(V_0 - E)}}{\hbar};\ \zeta = \frac{\alpha^2 - P^2}{2\alpha\, P} \tag{8}$$

$$G = \cosh(PD_b)\cos(\alpha D_w) - \zeta \sinh(PD_b)\sin(\alpha D_w) \tag{9}$$

$S = \cosh(PD_b)\cos(\alpha D_w) + \zeta \sinh(PD_b)\sin(\alpha D_w)$ (10)

The transmission coefficient is given by, $t = \frac{1}{(2G^2-1)^2+4S^2G^2}$ (11)

Sharp peaks in the transmission coefficient, t, corresponding to certain incident energy. Figure 62(b) shows the tunneling coefficient for well widths of 3, 4, and 5 nm. In terms of quality, the theoretical results match the experimental data very well.

### 6.7 Conclusion:

To summarize, using a PECVD process, we developed a direct approach for constructing devices with atomically thin tunnel barriers by depositing h-BN barrier layers on Si/SiO2 substrates with graphene as the active electrode layers and the quantum well. Three graphene layers were separated by two thin h-BN layers in a double barrier device made with graphene and h-BN sequential deposition. Our measurements of the electron tunneling current through the two barriers show that the h-BN films operate as effective tunnel barriers. At room temperature, the I-V characteristics of various barrier widths and thicknesses ranging from 2.86 to 5.15 nm were measured. At ambient temperature, double barrier tunneling based on five-layer devices exhibits resonant quantum tunneling in the presence of NDC.A systematic behavior of the current peak values and the corresponding voltage values in I-V curves were seen to be in good agreement with the transmission coefficient calculated using a quantum mechanical model.

# CHAPTER 07

# DIRECT FABRICATION AND CHARACTERIZATION OF VERTICALLY STACKED $MgB_2$ /h-BN/ $MgB_2$ TUNNEL JUNCTIONS

## 7.1 Introduction:

### 7.1.1 The Discovery of Superconductivity:

In 1911, the Leiden Laboratory discovered superconductivity[327]. When H. Kamerlingh-Onnes investigated the temperature dependence of the electrical resistivity of mercury, he observed that the resistance of the sample went to zero at roughly 4.2 K and remained unmeasurable at all possible temperatures below T*. As the temperature decreased, the resistance dissipated instantly rather than gradually. The sample has obviously converted into a state characterized by zero electrical resistance, which has never been observed before. Superconductivity is the name for this type of phenomena. Ultimately, all's efforts to develop bulk superconductor resistance failed[328]. Based on the sensitivity of current equipment, we may assume that superconductors have zero resistivity at the level of $10^{-24}$ n cm. At 4.2 K, the resistivity of high-purity copper is $10^{-9}\Omega$–cm[329].

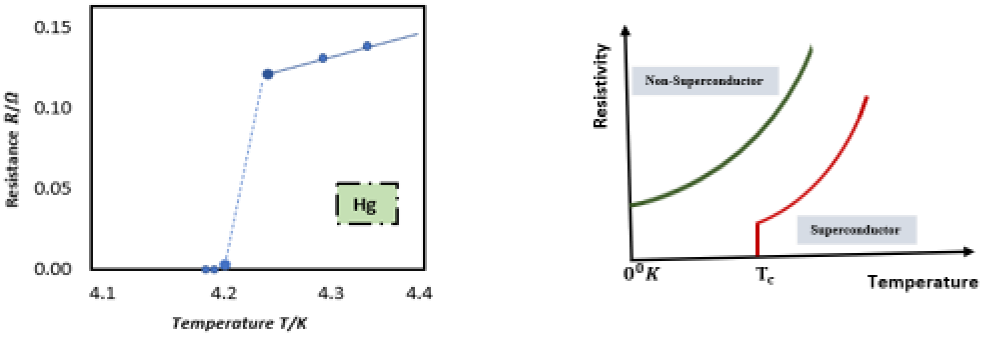

Figure1.The resistance of mercury measured by Onnes.

Figure 63: Critical Temperature of Superconductor

Not long after the discovery of mercury, superconductivity was discovered in a number of other metals such as tin, lead, indium, aluminum, niobium, and others. In addition, superconductors have been identified in a range of aluminum alloys and intermetallic combinations[110].

The critical temperature at which a normal conductor becomes superconducting is referred to as Tc. Soon after, it was discovered that not only could superconductivity be destroyed by heating the sample, but also by subjecting it to a low-level magnetic field[330]. Hem, or considerable field of bulk material, is the name of this field. In English-language literature, Hem is frequently referred to as Hcth (thermodynamic critical field).

Characteristics of superconductivity that are unique:

- There is no resistance to direct current.
- The carrying density of current is high.
- The resistance is exceedingly low at high frequencies.
- The dispersion of the signal is minimal.
- Magnetic fields have a high level of sensitivity.

- A magnetic field that has been formed intentionally is isolated from its surroundings.
- A single flux flow's quantum transmission takes only a few seconds.
- The transmission speed of a signal is the same as the speed of light.

Electric power transfer is greatly influenced by zero resistance and high current density, allowing for the employment of much smaller or stronger magnets. Low resistance at high frequencies is crucial in motors, generators, energy storage, medical equipment, and industrial separations. Microwave components, communications technology, and a range of military applications benefit from the extremely low signal dispersion and minimized downsizing issues caused by resistive (or $I^2R$) heating.

Superconductors can detect more than 1000 times more than the most advanced conventional measurement equipment due to their incredible magnetic field sensitivity. There should be a mechanism to prevent magnetic fields from penetrating into multilayla yer electronic components[331], as well as to control charged particles in the magnetic field. These materials can be employed in high-speed computing and digital electronics in ways that semiconductors cannot. All these characteristics have been extensively proved all over the world. After the discovery of the superconductivity, by cooling mercury steel to extremely low temperatures and seeing no protection from electrical current. Various additional steels and steel alloys were discovered to become superconductors at temperatures lower than 23.2 K prior to 1973, and LTS products (Reduced Temperature level Superconductor) were developed. Since the 1960s, commercial superconducting magnets have been made using a Niobium-Titanium (Ni-Ti) alloy. A tight Niobium-Tin intermetallic relationship has recently emerged as a potential possibility for intensifying the magnetic field of currents material even further. J. G. Bednorz and K. A. Müller discovered in 1986 that a set of chemical elements-located ceramic written matter hold superconducting real estate up to 35 degrees Celsius. In early 1987, C. W. Chu stated that he had developed a cuprate superconductor that could operate at temperatures higher than 77 K, the boiling point of liquid nitrogen. Other oxide-based superconductors with prospective manufacturability benefits and critical temperatures as high as 135 K have been developed since then, thanks to extensive study. A superconducting material having a critical temperature greater than 23.2 K is referred to as a High Temperature Superconductor, despite the continual necessity for cryogenic cooling in any application (HTS). Superconductor technology works best when it provides a one-of-a-kind solution to a problem, as demonstrated by forty years of research and development of LTS materials-based applications. Because superconductors are more expensive than conventional conductors in general, the system must be extremely cost effective. HTS has changed the refrigeration environment by enabling smaller, more efficient cooling systems in particular applications. Before superconductivity can deliver on its current promise of very large potential benefits and generate meaningful intended for financial gain venture into new great labor, design, addition of superconducting and supercooled electronics, evidence of plan cost provision for the future, and general stability must all be achieved. One of the most significant scientific accomplishments of the 20th century is superconductivity. Due to this extraordinary new property, certain materials lose all resistance to electricity flow at low temperatures. This state of "losslessness" allows for a wide range of new technological applications. In the twenty-first century, superconductivity is the foundation for new commercial objects that are altering our economy and everyday life.

### 7.1.2 The Meissner effect:

In 1933, Walter Meissner and Robert Ochsenfeld discovered a unique phenomenon that demonstrated superconductors interact with a perfect conductor. Assume that the ideal photographer's essential indifference functions in harmony with Tc, the superconductor's remote disinterest. They come out two together, electrically at odds, and comport themselves when they are at their most natural. The current drawing field Ba is now visible as a result of this. As a result, two of these letters are likely to be delivered simultaneously. Assume that the ideal conductor's and superconductor's critical temperatures are both greater than Tc. In other words, they are both electrically conductive and electrically resistive. After that, the Ba magnetic field is injected. As a result, the field is capable of passing through a variety of materials. The two samples are joined to produce a perfect conductor after cooling to zero resistance. The magnetic field inside the superconductor is demonstrated to be evacuated, whereas the perfect conductor's internal field remains conserved. The magnetic field must be evacuated, removing the superconductor's source of energy. This energy is produced through an exothermic superconducting transition. When the field is turned off, currents flow via the perfect conductor. The magnetic field of a superconductor fluctuates according to Lenz's law[332]. In contrast, the superconductor returns to its original condition, which is free of both internal and external magnetic forces.

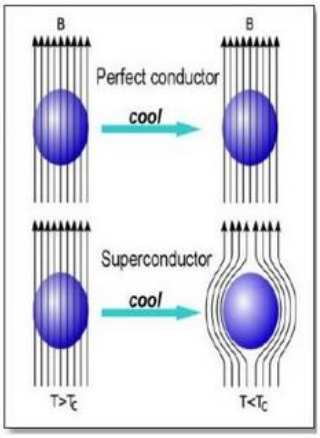

Figure 64: It shows and explains the phenomenon of Meissner effect.

### 7.1.3 Type I and II superconductors:

Superconductivity is destroyed by high magnetic fields, causing the system to return to a conducting condition. The nature of the transition distinguishes type I and type II superconductors. The intensity of the internal magnetic field, Bi, increases in direct proportion to the applied magnetic field. The internal field is found to be zero until a critical magnetic field, Bc, is reached, at which time the condition changes fast to normal (as predicted by the Meissner effect). As a result, the applied field may be able to penetrate the inside. Type I superconductors quickly revert to their original state after being subjected to a magnetic field. Type I superconductors make up the vast bulk of pure elements. When Type II superconductors are exposed to a magnetic field, they behave differently (see Figure 65).

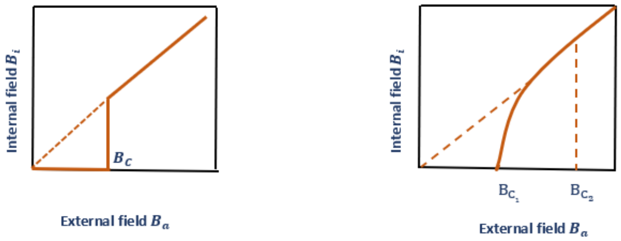

**Figure (1). Type-I superconductor behaviour.**

**Figure (2). Type-II superconductor behaviour.**

Figure 65: Type of Superconductors

From zero, a rising field produces two critical fields, $B_{C_1}$ and $B_{C_2}$. The applied field penetrates the superconductor's core at $B_{C_1}$. In contrast, superconductivity has stayed constant. Superconductivity is terminated at the second and considerably higher critical field, $B_{C_2}$. The Meissner effect is incomplete because applied fields between $B_{C_1}$ and $B_{C_2}$ can only partly permeate the superconductor. As a result, the superconductor has the ability to endure extremely high magnetic fields.

High field electromagnets built of superconducting wire are the most technologically beneficial because the second critical field of type II superconductors may be rather enormous. Figure 65 depicts a broad range of type II superconductors. In theory, niobium-tin (Nb3Sn) wires have a $B_{c_2}$ of up to 24.5 Tesla, but in fact, it is significantly lower. As a result, they are suited for applications requiring high magnetic fields, such as MRI scanners. Superconducting electromagnets have the advantage of only transporting current down the wires once before shutting down, allowing the current (and field) to continue indefinitely as long as the superconductor's temperature remains below its critical value. In other words, the external power supply can be turned off. In comparison, the most powerful permanent magnets on the market today may be capable of producing a field of around 1

Tesla. A niobium–tin superconductor has a potential energy of 24.5 Tesla. "Type II," according to some non-experts, refers to the high-temperature superconductors discovered[109, 333] in the late 1980s. Many of the previously discovered superconductors were type II superconductors as well.

### 7.1.4 BCS theory and Cooper pairs:

Phonons are collisions between free electrons and crystal lattice vibrations that contribute for a minor fraction of a metal's resistance, according to classical physics. Electron scattering from impurities or imperfections in the wire also contributes to the resistance. The topic of why superconductors do not show this behavior arose as a result. The BCS theory[111], a microscopic theory of superconductivity, was discovered in 1957 by John Bardeen, Leon Cooper, and J. Robert Schrieffer. If two electrons in a superconductor make an attractive contact, they can create a bonded pair known as a Cooper pair[334], according to the BCS theory. At first glance, this theory looks strange because electrons repel each other due to their identical charges. Figure 66 depicts this, which may be read as follows[306]:

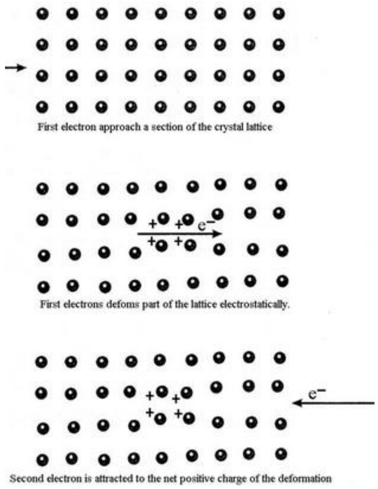

Figure 66: Classical description of the coupling of a Cooper pair.

Positive ions are pushed across the lattice by an electron, changing their nominal locations. The second electron (the Cooper pair partner) [306]is drawn to the displaced ions once it arrives. Only if the second electron gets close enough to the ions before they return to their equilibrium locations can it be pulled to the lattice deformation. As a result, the two electrons are drawn closer together, delaying their arrival. Because its duration is too short to allow it to propagate across the lattice like a wave, this short-lived lattice deformation is sometimes referred to as a virtual phonon. According to BCS theory, the total linear momentum of a Cooper pair must be zero. Figure 66 depicts their journey in several directions. The hypothetical distance (known as the coherence length) between Cooper pairs can also range from hundreds to thousands of ions! Several textbooks have misrepresented this significant distance. Electrostatic (coulomb) repulsion will be significantly greater than lattice deformation attraction if electrons in a Cooper pair are too close together, such as a few atomic spacings apart, and they will resist each other. As a result, superconductivity will cease to exist. Because a current passing through a superconductor only slightly alters the total moment from zero, one electron in a cooper pair has a little bigger momentum magnitude on average than its pair. However, they continue to move in opposite directions A Cooper pairs's connection is transient. The process is repeated with the freshly formed Cooper pair, with each electron forming a Cooper pair with another electron. As a result, each electron in the solid is attracted to each other, forming a dense network of connections. To collide with and scatter from atoms in the lattice, the complete network of electrons must clash with it, consuming energy. Collisions with the lattice are avoided by the collective activity of the electrons in the solid. Nature seeks situations that require as little effort as possible. In this situation, avoiding collisions with the lattice is the most energy-efficient option. To destroy the superconducting state and return it to normal, a minimal amount of energy is required. This amount of energy is known as the energy gap. Even though a classical description of Cooper pairs is presented here, the formal technique of the BCS theory is quantum mechanical. Electron activity is depicted as a wave function that spans the material and overlaps with other electrons' wave functions. As a result, the entire network of electrons behaves as if it were a single wave function, resulting in coherent collective motion. Each electron spins and possesses linear momentum. Surprisingly, this property is known as spin. This does not always imply that the electron is spinning, but it appears to be. The spins of a Cooper pair must face opposite directions, according to the BCS theory. BCS theory explains both the Cooper pair explanation and the graphical depiction presented here. Current HSC textbooks, on the other hand, tend to distort this image by enforcing artificial assumptions such as the Cooper pair being within one or two atomic spacings of each other and moving in the same direction, which are both false.

### 7.1.5 High – Tc superconductors:

For a long time, superconductivity researchers have been hunting for a material that can become a superconductor at room temperature[333]. A discovery [335]of this size will have far-reaching consequences for current technology, including power transmission and storage, communication, transportation, and even the type of computers we create. All of these developments will be faster, less costly, and use less energy. At the time, this is a work in progress. In 1986, Bednorz and Müller identified a class of materials that led to the development of superconductors, which we now utilize on a benchtop and chill using liquid nitrogen. Bednorz and Müller were awarded the Nobel Prize in Literature in 1987 (the Nobel committee's first acknowledgement). The most prevalent tabletop material is Yttrium, Barium, Copper Oxide (YBa2Cu3O7)[336]. The 1-2-3 superconductor is classed as a Tc superconductor (high temperature). Figure 67 depicts the critical temperature of numerous high-Tc superconductors. It's crucial to keep the temperature between 135 and 135 K. Even though it is not at room temperature, liquid nitrogen (with a boiling point of 77 K) has made superconductivity experiments more accessible to a larger range of individuals. Cooling liquid helium superconductors was previously expensive and time-consuming. Furthermore, the maximal critical magnetic field of superconductors, $B_{C_2}$, is expected to be around 200 Tesla, which is a big number! The crystal lattice structure of YBa2Cu3O7 is shown in Figure 67. On contrast to prior superconductors, conduction occurs mostly in the planes containing copper oxide. The critical temperature has been shown to be highly dependent on the average amount of oxygen atoms present, which fluctuates. Consequently, the 1-2-3 superconductor formula is usually written as YBa2Cu3O7-, where is a number between 0 and 1. In these superconductors, the nominal distance between cooper pairs (coherence length) can be as tiny as one or two atomic spacings. As a result, at these distances, the coulomb repulsion force typically wins, resulting in electrons being repelled rather than linked. As a result, it is commonly considered that Cooper pairs in these materials are created by the type of magnetism present (known as Anti ferromagnetism) in the copper oxide layers rather than by lattice deformation. As a result, the BCS theory, which depends on lattice deformation to allow electron pair coupling, is unable to account for high–Tc superconductors. The technique by which these materials become superconducting is being explored at the moment.

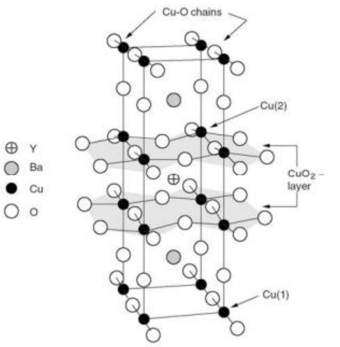

Figure 67: Crystal lattice structure of the high-Tc superconductor, YB$\mathbf{a_2}$C$\mathbf{u_3}$$\mathbf{O_7}$.

## 7.2 The Josephson Junction:

Only superconductors have the Josephson Junction, which operates as a switch. Only a little amount of current can travel across a weak connection between two superconductors when there is no voltage drop or energy loss. The junction activates when the current hits the critical current, resulting in a single flux quantum (SFQ). The switching time is measured in picoseconds[337], a fraction of a second quicker than a silicon transistor. Furthermore, the needed switching energy is hundreds of times lower. Superconducting logic circuits have been utilized to achieve hundreds of gigahertz. The energy required per computation has been greatly lowered as a consequence of advancements in SFQ logic circuits.

Despite their low energy consumption, passive transmission lines can be employed to connect superconducting circuit elements. Pulses composed of a single or multiple flux quanta travel at nearly one-third the speed of light in a vacuum, making these connections very fast.

Computers, too, require memory[338]. A compact superconductor loop can only carry a finite number of flux quanta. In digital logic, the absence of flux quanta in the loop is represented by a '0.' It has been challenging to create tiny loops with sufficient inductance, but this difficulty may be overcome by utilizing approaches that have previously proved effective in the manufacture of smaller-scale semiconductor circuits. Other memory or inductive components that are only possible because of superconductivity are also being researched, which might lead to increased physical density.

Revolutionary logic, interconnects[339], and memory with features that differ significantly from current technology will enable revolutionary computer architectures and capabilities. The development of superconducting computers has begun. The IARPA Cryogenic Computing Complexity (C3) project, for example, is seeking to develop the necessary technologies before merging them into a superconducting computer. In this image, a future superconducting computer is seen beside a regular supercomputer.

Another potential application for superconductivity is quantum computing, but this is still a long way off. Quantum bits, in contrast to traditional digital data bits, which can only have one of two states—'1' or'0,' can have a range of states and can be utilized to solve some problems quicker than traditional digital computers. Superconducting computer technology will require people with both innovative ideas and the capacity to put them into action.

### 7.2.2 Josephson effect:

A supercurrent can flow between two superconductors that are separated by a narrow restricting zone, a normal region, a high resistance insulating barrier, or any combination of these qualities. The Josephson effect is what it's called (B. Josephson, 1962)[340]. The current is influenced by the phase difference between the two superconductors. Weak connections are what they're called. The phase difference can cause the current to change in a range of methods. The conductance of the link influences both the shape of this dependency and the maximum supercurrent: The dependency approaches a fundamental sinusoidal form as the conductance decreases.

A supercurrent is a graphical representation of phase consistency, an essential property shared by two superconductors separated by a thin interface.

### 7.2.3 Josephson Junctions:

In a Josephson junction, two superconductors are sandwiched between two non-superconductors (insulating layer), allowing electrons to tunnel through. The coherence of a superconductor's wave function creates DC or AC currents. The phase difference between the two superconductors determines the DC Josephson current. The frequency f of the alternating current Josephson current is determined by the voltage V applied across the junction $= {}^{2eV}/_{h}$ .

To equalize voltage, frequency can now be employed. A valid voltage of $10^{-10}$can be achieved with a Josephson junction standard. By serially connecting thousands of connections, the volt regime produces a standard. Magnetic flux ($10^{-14}$ T) is extraordinarily sensitive in a superconducting loop with two Josephson junctions in each arm (SQUID, superconducting quantum interference device).

## 7.3. Current Commercial Applications:

All the fundamental commercial applications of superconductivity outlined above in the medical diagnostic, research, and industrial processing sectors require the use of LTS materials and relatively high field magnets. Without superconducting technology, the majority of these applications would be difficult to accomplish. Several modest applications based on LTS materials, such as research magnets and magnetoencephalography, have also been proposed (MEG). To understand and detect the brain's weak magnetic fields, the latter uses Superconducting Quantum Interference Device (SQUID) technology. Electronic filters used in wireless base stations are the most recent major commercial products that utilize HTS materials. So far, 10,000 devices have been installed in wireless networks throughout the world. The sections that follow go into further depth on these applications.

### 7.4. Magnesium-diboride:

From 1911 until 1973, when superconductivity was discovered[341], the highest known transition temperature (Tc) increased at a modest average rate of 0.3 K per year, from 4 K in Hg to 23 K in $Nb_3Ge$. The microscopic underpinnings of superconductivity, based on electron–phonon interactions and explained by the immensely powerful BCS theory, were well known at the time. In the early 1980s, it was commonly anticipated that this matching strategy would not result in a significant increase in Tc. The discovery of superconductivity [342]in $MgB_2$, a typical binary molecule, came as a pleasant surprise in 2001, at a time when science had mostly settled down. $MgB_2$ was discovered to be more comparable to low Tc superconductors (LTS) than oxide superconductors (then called as high temperature SCs or High Temperature Superconductors) (HTS). The finding of a substantial boron (B) isotope effect demonstrated that $MgB_2$ superconductivity is phonon-mediated, and comprehensive experimental evidence supported the s-wave symmetry of the order parameter. Tc 39 K, on the other hand, directly contradicted the widely held opinion that $Nb_3Ge$'s Tc represented the upper limit for this process, revealing $MgB_2$'s uniqueness and requiring us to reconsider some of our earlier assumptions. Although $MgB_2$ was discovered in the 1950s, it was not investigated or utilized as a conventional superconductor until 2001. $MgB_2$ has the highest critical temperature of any known intermetallic compound, with a temperature of 39 Kelvin. In this chapter, we'll look at the crystal structure of $MgB_2$, the origins of superconductivity, and manufacturing procedures. This section will discuss what distinguishes this superconductor from others.

### 7.4.1 Crystal and Electronic Structure of $MgB_2$:

$MgB_2$ outperforms other conventional superconductors in terms of critical temperature (Nb, for example). The transition temperature of 39K is three times lower than the transition temperature of mercury-based high-Tc superconducting cuprates, which is 130K. At liquid nitrogen temperatures, copper oxide with a high Tc has also been demonstrated to operate. Because of manufacturing issues and the substantial residual resistance generated by the weak link effect, these unconventional superconductors are only appropriate for SRF holes. Let's start with the crystal and electrical structures[343] of $MgB_2$, then go on to the intriguing features that make it a candidate superconductor material[344].

### 7.4.2 Superconductivity of $MgB_2$:

The discovery of the unusually high superconducting temperature (T_C = 39 K) in magnesium diboride ($MgB_2$) by Akimitsu in 2001 [341]and the prospects to use nanoengineering techniques to enhance the transition temperature (T_C), flux pinning, critical current (J_c), and upper critical field (H_c) in such a simple structure continues to generate much interest in the scientific research community. Different types of substitutional doping, namely electron and hole doping, co-doping of electrons and holes, isovalent substitutions and magnetic substitutions have been attempted[112, 113]. Such substitution in $MgB_2$ can modify the electronic structure and density of states (DOS) and introduce defects in the structure. Here we use thin films of $MgB_2$ with 2-dimensional h-BN as an insulating barrier to realize a Josephson junction.

### 7.4.3 Synthesis of $MgB_2$ Film:

A HPCVD setup was used for the synthesis of $MgB_2$ thin film, Briefly, it consists of a reactor consisting of a 4-way stainless cross and a resistively heated substrate holder located in the center of the reactor. The sample holder has a groove close to the outer edge, where high purity Mg pieces are placed, while the substrate is placed in the center. The deposition takes place at approximately 740 °C in high purity $H_2$ gas, and the thermal evaporation of Mg provides a high enough Mg partial pressure for the phase stability of $MgB_2$. The $MgB_2$ growth is initiated by introducing $B_2H_6$ gas into the reactor as the B source[345].

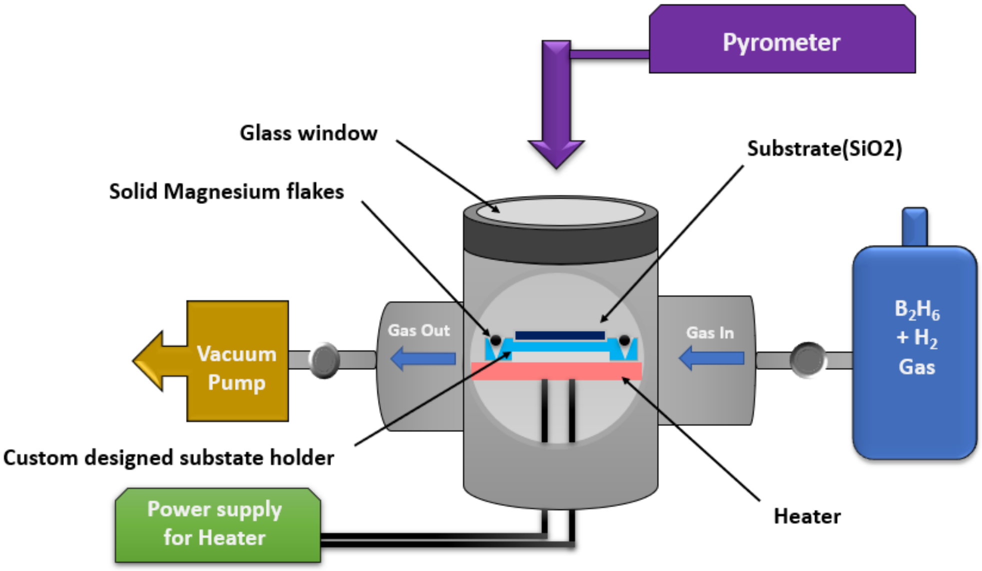

Figure 68 Schematics of $MgB_2$ synthesis using hybrid physical chemical vapor deposition (HPCVD) technique

A pyrometer was used to measure the substrate temperature. Mg vapor was generated by sublimation. The Mg vapor pressure at 470 °C is about $10^{-2}$ Torr and is within the phase stability window of $MgB_2$ according to the Mg-B thermodynamic phase diagram. It is desirable for the temperature to be lower at the center of the substrate to drive the Mg vapor towards it, therefore we limited the heating to only at the edge of the substrate holder. However, Cu has a high thermal conductivity and the temperature at the surface of the Cu disc is expected to be mostly uniform. To compensate for the potential lack of a temperature gradient, we added a Mo cap to the rim of the sample holder so that the Mg vapor was

Figure 49. Synthesis of **$MgB_2$** using HPCVD technique

directed towards the center. Figure 69shows a photograph of the sample holder containing a 2-inch Cu disc and 99.99% pure Mg pellets placed on the heating element, the sample holder with the Mo cap on and a photograph of a regular HPCVD setup for small substrates is shown for comparison. During the film deposition on the Cu disc, the process pressure was 10 Torr, the $H_2$ carrier gas flow rate was 400 standard cubic centimeters per minute (sccm), and the flow rate of 5% $B_2H_6$ in $H_2$ mixture was 20 (sccm).

### 7.5.3 Characterization of $MgB_2$:

#### 7.5.3.1. EDS and SEM Measurement:

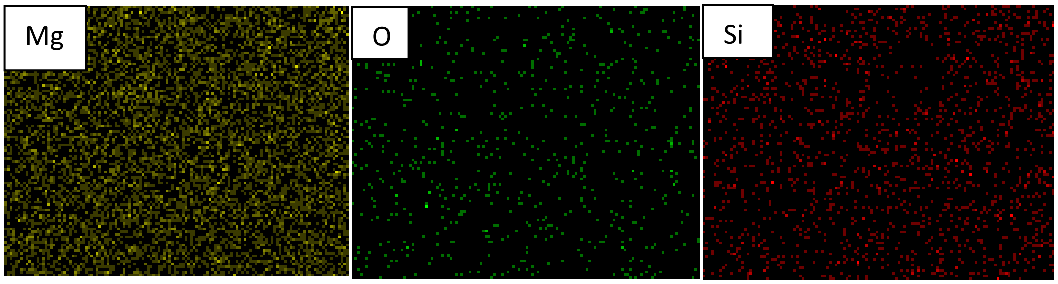

Figure 70: EDS results of $MgB_2$ film grown on Si/$SiO_2$ substrate showing the Mg, O and Si maps.

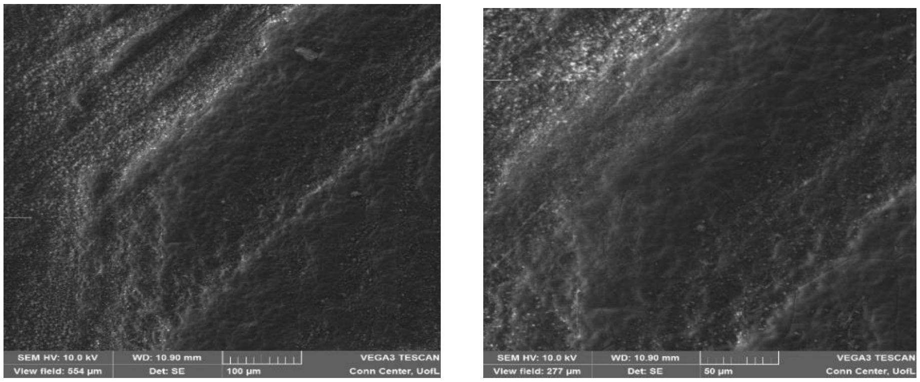

Figure 71: SEM images of the surface of $MgB_2$ film grown on $Si/SiO_2$ substrate

Figure 70 shows the EDAX mapping of the $MgB_2$ with clear signature of Mg in addition to Si and oxygen. EDAX is not capable of detecting B. Fig. 71 shows the SEM images of the surfaces of the $MgB_2$ films.

### 7.5.3.2 Raman Measurement of $MgB_2$:

The published Raman spectra of $MgB_2$ samples both polycrystalline and small single crystals contain mainly the broad bands extending from 300 to 1600 $cm^{-1}$. The main peak [346]at ~ 600 $cm^{-1}$ is generally associated with the $E_{2g}$ mode, but its unusually broad width (~ 270 $cm^{-1}$), as well as the presence of other broad peaks in the spectra make the assignment difficult. The presence of impurity phases such as elemental Mg, MgO, $B_2O_3$ Mg (OH)2, $MgCO_3$ and $MgB_4$ are also present in the Raman spectra[346].

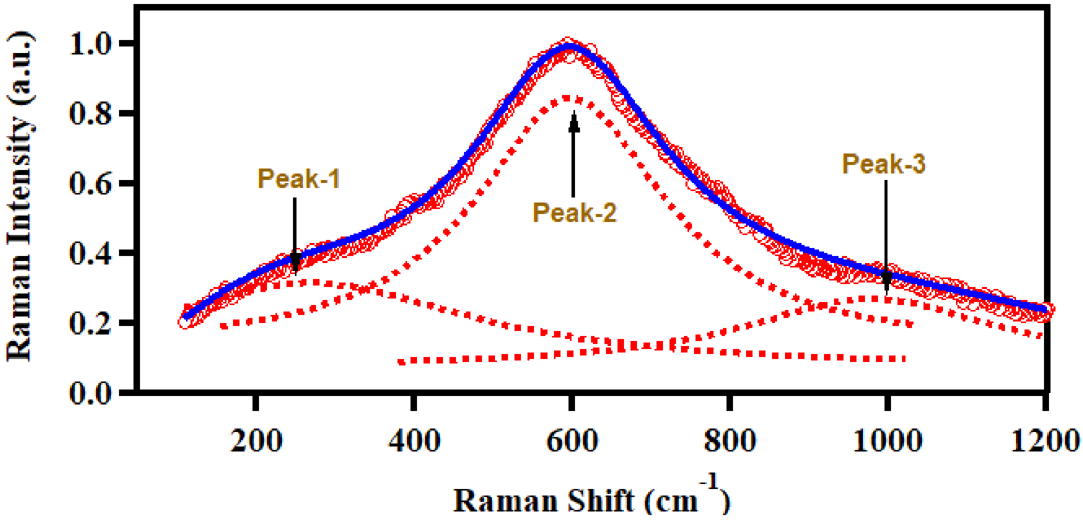

Figure 72: Raman Spectrum of MgB2.

## 7.6. Results and Discussions:

### 7.6.1. Electrical Measurement of thermoelectric power and resistance:

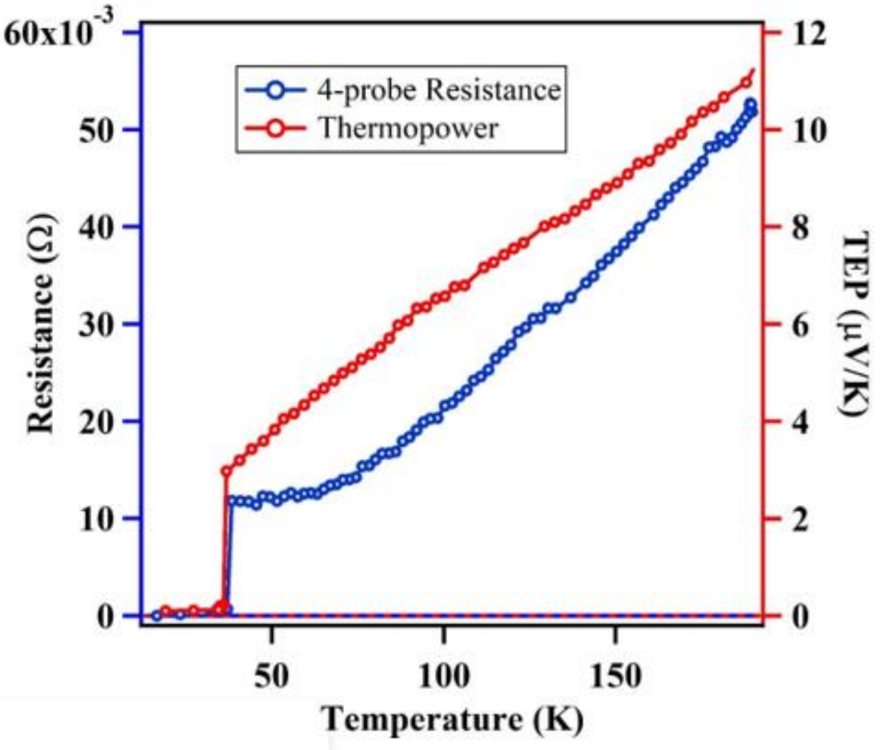

Figure 73: Temperature-dependence of the 4-probe resistance and the Thermopower of the $MgB_2$

The resistivity and the Seebeck coefficient of the $MgB_2$ films were measured in a four-probe configuration and analog subtraction method respectively. The sample deposited on a $Si/SiO_2$ substrate was mounted on a Kapton (polyimide) tape fixed to a block of oxygen-free high-conductivity copper attached to a chip carrier. Two miniature Chromel/Au–Fe thermocouples and two additional copper wires were mounted at the edges of the sample with silver epoxy. The chip carrier was attached to the cold head of a closed-cycle refrigerator using Stycast epoxy to ensure proper thermal contact between the cold head and the sample. In order to measure the four-probe resistivity in a van der Pauw configuration, an excitation current (using a Keithley 2400 source meter) was applied through the two current leads and the voltage across the two thermocouple wires was measured using a Keithley Nanovoltmeter. One of the thermocouples was used to measure the sample temperature. The resistivity of the $MgB_2$ and $MgB_2$-SWCNT composites were measured over a wide temperature range (300 K to 20 K). Fig. y shows the four-probe resistance and the thermopower of a $MgB_2$ film grown by hybrid CVD method. Both data show the onset of TC at ~ 37 K.

### 7.7 Josephson Tunneling:

A Josephson junction is made up of two superconductors separated by a thin insulating (non- superconducting) layer such that cooper-pairs of the superconductors can tunnel through the barrier. The coherence of the wave function in the superconductor leads to DC or AC currents. The DC Josephson current is proportional to the phase difference between the two superconductors. The frequency f of the AC Josephson current is proportional to the voltage V applied across the junction, f=2eV/h. This allows for a voltage normal based on a frequency. A Josephson junction standard can realize a voltage with an accuracy of $10^{-10}$. For a standard in the volt regime several thousand junctions are put in series. A superconducting loop with two Josephson junctions in either arm is very sensitive ($10^{-14}$ T) to the magnetic flux enclosed (SQUID, superconducting quantum interference device). A Josephson junction (JJ) made of two weakly coupled superconductors, $S_1$ and $S_2$ separated by a very thin insulating barrier, as shown in Fig. 74.

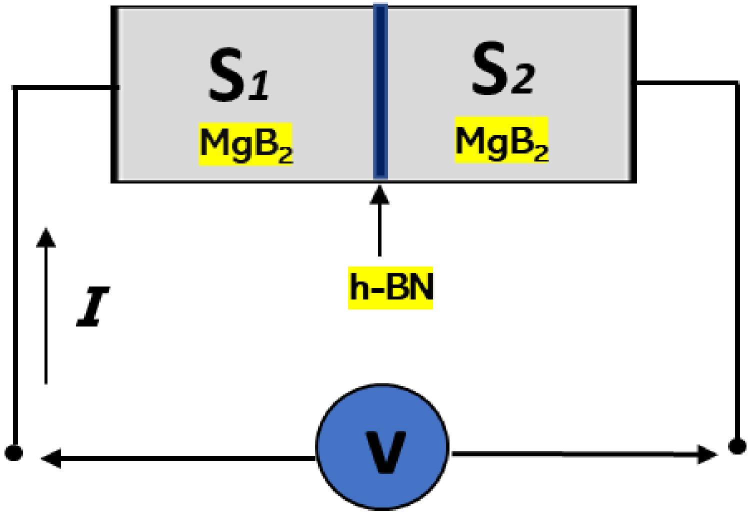

Figure 74 Schematic representation of a Josephson junction consisting of two superconductors, $S_1$ and $S_2$, separated by a very thin insulator

By denoting the superconducting wave-functions in the superconductors $S_1$ and $S_2$ as $\psi_1$ and $\psi_2$ respectively, we can set

$\psi_{1=\sqrt{n_1}}e^{-i\theta_1}$ and $\psi_{2=\sqrt{n_2}}e^{-i\theta_2}$ (1.1) where $n_i$ is the number density of Cooper pairs and $\theta_i$ is the superconducting phase of the $i$th electrode ($i$= 1, 2). When both wave-functions, $\psi_1$ and $\psi_2$, do not depend on position, we can take $n_i$ to be the number of Cooper pairs so that

$\psi_1^{*^2}+\ \psi_2^{*^2}=n_1+n_2$

If K is the coupling energy constant between the superconductors $S_1$ and $S_2$

$$i\hbar\frac{\partial}{\partial t}\psi_1 = \frac{qv}{2}\psi_1+k\psi_2$$

$$i\hbar\frac{\partial}{\partial t}\psi_2 = -\frac{qv}{2}\psi_2+k\psi_1$$

using

$$\psi_1 = \sqrt{n_1}\, e^{i\theta_1}$$

$$\psi_2 = \sqrt{n_2}\, e^{i\theta_2}$$

$$\boxed{\begin{aligned} &\frac{i\hbar}{2\sqrt{n_1}}\,\dot{n}_1 e^{i\theta 1} \_\, \hbar\sqrt{n_1}\,\dot{\theta}_1 e^{i\theta 1} = \frac{qV}{2}\sqrt{n_1}\; e^{i\theta 1} + k\sqrt{n_2}\, e^{i\theta 2} \\ &\frac{i\hbar}{2\sqrt{n2}}\,\dot{n}_2 e^{i\theta 2} \_\, \hbar\sqrt{n_2}\dot{\theta}_2 e^{i\theta 2} = -\frac{qV}{2}\sqrt{n_2}\, e^{i\theta 2} + k\sqrt{n_1}\; e^{i\theta_1} \end{aligned}}$$

$$\frac{dn_1}{dt} = \frac{2k}{\hbar}\sqrt{n_1}n_2 \sin\delta$$

$$\frac{dn_2}{dt} = -\frac{2k}{\hbar}\sqrt{n_1}n_2 \sin\delta$$

$$\frac{d\delta}{dt} = \frac{qv}{\hbar} + \left(K\sqrt{\frac{n_2}{n_1}} - \sqrt{\frac{n_1}{n_2}}\right)Cos\delta$$

$$\delta = \theta_2 - \theta_2$$

$$J = \frac{2qk}{\hbar}\sqrt{n_1 n_2}\sin\delta$$

$$= J_o \sin\delta$$

### 7.7.1. I-V tunneling characteristics Measurements:

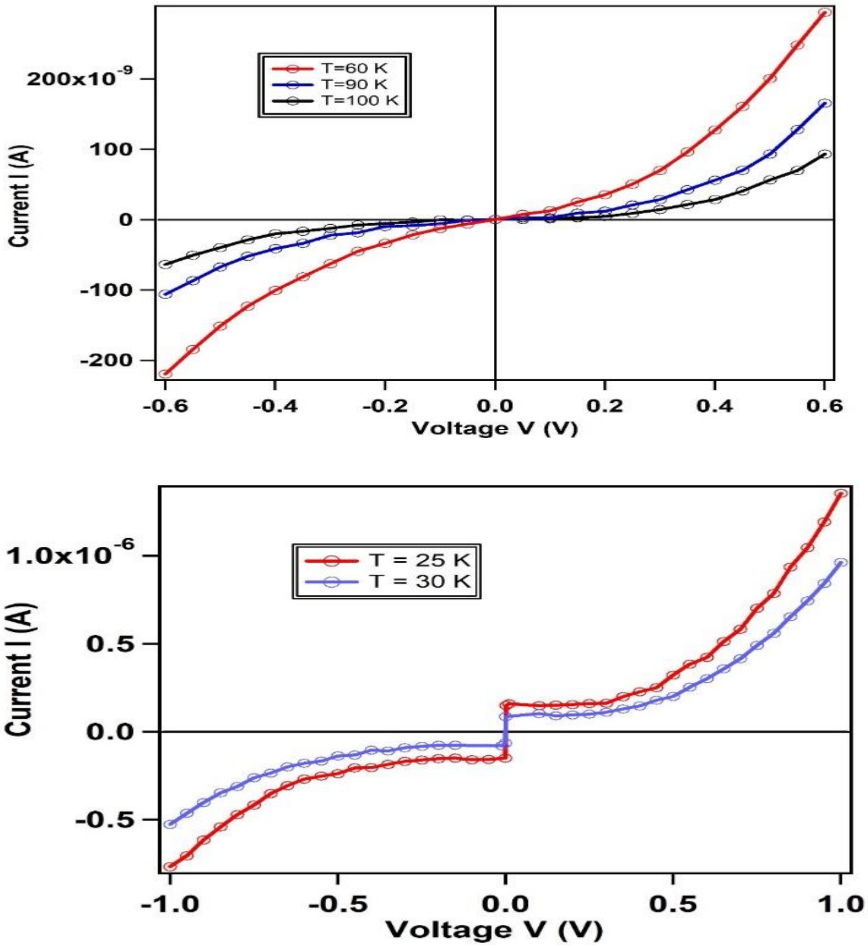

Figure 75 I-V tunneling characteristics of $MgB_2$/h-BN/ $MgB_2$ structure (top) above Tc (bottom) below Tc

Figure 75 shows the I-V tunneling characteristics of $MgB_2$/h-BN/ $MgB_2$ structure above and below the transition temperature Tc (~ 37 K). Above $T_c$, it shows typical quantum tunneling behavior. However, below $T_c$ it exhibits a substantial super current which increase with lowering of the temperature.

## 7.8 Conclusion:

In conclusion, we developed a direct technique for fabricating devices with atomically thin tunnel barriers by merging h-BN with magnesium diboride active electrode layers on a Si/$SiO_2$ substrate using a PECVD (for h-BN) and an HPCVD (for $MgB_2$ thin film synthesis) approach. Using current-voltage measurements and thermoelectric power for $MgB_2$, the temperature-dependence of the 4-probe resistance and the thermopower of the $MgB_2$ film were confirmed to be in agreement. For Josephson junction, above and below the transition temperature Tc, the I-V tunneling properties of the $MgB_2$/h-BN/ $MgB_2$ structure (37 K). It works properly over Tc in terms of quantum tunneling. It does, however, have a significant supercurrent below Tc, which increases as the temperature decreases.

# REFERENCES

1. Chang, C.; Chen, W.; Chen, Y.; Chen, Y.; Chen, Y.; Ding, F.; Fan, C.; Fan, H. J.; Fan, Z.; Gong, C. J. A. P.-C. S., Recent progress on two-dimensional materials. 2021, *37* (12), 2108017.

2. Sun, L.; Wang, W.; Yang, H. J. A. I. S., Recent progress in synaptic devices based on 2D materials. 2020, *2* (5), 1900167.

3. Yu, J. H.; Lee, H. R.; Hong, S. S.; Kong, D.; Lee, H.-W.; Wang, H.; Xiong, F.; Wang, S.; Cui, Y. J. N. l., Vertical heterostructure of two-dimensional MoS2 and WSe2 with vertically aligned layers. 2015, *15* (2), 1031-1035.

4. Zhang, J.; Xie, W.; Zhao, J.; Zhang, S. J. D. M., Band alignment of two-dimensional lateral heterostructures. 2016, *4* (1), 015038.

5. Rudner, M. S.; Lindner, N. H. J. N. r. p., Band structure engineering and non-equilibrium dynamics in Floquet topological insulators. 2020, *2* (5), 229-244.

6. Brown, E.; Zhang, W.-D.; Growden, T.; Fakhimi, P.; Berger, P. J. P. R. A., Electroluminescence in Unipolar-Doped In 0.53 Ga 0.47 As/Al As Resonant-Tunneling Diodes: A Competition between Interband Tunneling and Impact Ionization. 2021, *16* (5), 054008.

7. Su, J.; Li, G. D.; Li, X. H.; Chen, J. S. J. A. S., 2D/2D heterojunctions for catalysis. 2019, *6* (7), 1801702.

8. Wang, P.; Jia, C.; Huang, Y.; Duan, X. J. M., Van der Waals Heterostructures by Design: From 1D and 2D to 3D. 2021, *4* (2), 552-581.

9. Gobbi, M.; Orgiu, E.; Samorì, P. J. A. M., When 2D materials meet molecules: opportunities and challenges of hybrid organic/inorganic van der Waals heterostructures. 2018, *30* (18), 1706103.

10. Gao, M.-R.; Xu, Y.-F.; Jiang, J.; Yu, S.-H. J. C. S. R., Nanostructured metal chalcogenides: synthesis, modification, and applications in energy conversion and storage devices. 2013, *42* (7), 2986-3017.

11. Kufer, D.; Konstantatos, G. J. A. P., Photo-FETs: Phototransistors enabled by 2D and 0D nanomaterials. 2016, *3* (12), 2197-2210.

12. Qu, X.; Alvarez, P. J.; Li, Q. J. W. r., Applications of nanotechnology in water and wastewater treatment. 2013, *47* (12), 3931-3946.

13. Peng, X.; Chen, J.; Misewich, J. A.; Wong, S. S. J. C. S. R., Carbon nanotube–nanocrystal heterostructures. 2009, *38* (4), 1076-1098.

14. Wang, H.; Liu, F.; Fu, W.; Fang, Z.; Zhou, W.; Liu, Z. J. N., Two-dimensional heterostructures: fabrication, characterization, and application. 2014, *6* (21), 12250-12272.

15. Li, M.; Liu, D.; Wei, D.; Song, X.; Wei, D.; Wee, A. T. S. J. A. S., Controllable synthesis of graphene by plasma-enhanced chemical vapor deposition and its related applications. 2016, *3* (11), 1600003.

16. Sengupta, K.; Nagatsuma, T.; Mittleman, D. M. J. N. E., Terahertz integrated electronic and hybrid electronic–photonic systems. 2018, *1* (12), 622-635.

17. Bai, X.; Li, S.; Das, S.; Du, L.; Dai, Y.; Yao, L.; Raju, R.; Du, M.; Lipsanen, H.; Sun, Z. J. N., Single-step chemical vapour deposition of anti-pyramid MoS 2/WS 2 vertical heterostructures. 2021, *13* (8), 4537-4542.

18. Gong, C.; Zhang, H.; Wang, W.; Colombo, L.; Wallace, R. M.; Cho, K. J. A. P. L., Band alignment of two-dimensional transition metal dichalcogenides: Application in tunnel field effect transistors. 2013, *103* (5), 053513.

19. Ma, Z.; Wang, Y.; Wei, Y.; Li, C.; Zhang, X.; Wang, F. J. P. C. C. P., A type-II C 2 N/α-Te van der Waals heterojunction with improved optical properties by external perturbation. 2019, *21* (39), 21753-21760.

20. He, C.; Zhang, J.; Zhang, W.; Li, T. J. T. j. o. p. c. l., Type-II InSe/g-C3N4 heterostructure as a high-efficiency oxygen evolution reaction catalyst for photoelectrochemical water splitting. 2019, *10* (11), 3122-3128.

21. Fan, Y.; Ma, X.; Liu, X.; Wang, J.; Ai, H.; Zhao, M. J. T. J. o. P. C. C., Theoretical design of an InSe/GaTe vdW heterobilayer: a potential visible-light photocatalyst for water splitting. 2018, *122* (49), 27803-27810.

22. Horade, M.; Yamada, K.; Yamawaki, T.; Yashima, M. J. J. o. M.; Microengineering, Research on fabrication method for floating structures using general photolithography with high versatility. 2021, *31* (12), 125004.

23. Uhlig, M. R.; Martin-Jimenez, D.; Garcia, R. J. N. c., Atomic-scale mapping of hydrophobic layers on graphene and few-layer MoS2 and WSe2 in water. 2019, *10* (1), 1-7.

24. Bianco, A.; Cheng, H.-M.; Enoki, T.; Gogotsi, Y.; Hurt, R. H.; Koratkar, N.; Kyotani, T.; Monthioux, M.; Park, C. R.; Tascon, J. M. J. C., All in the graphene family–A recommended nomenclature for two-dimensional carbon materials. Elsevier: 2013; Vol. 65, pp 1-6.

25. Zhang, L. L.; Zhou, R.; Zhao, X. J. J. o. M. C., Graphene-based materials as supercapacitor electrodes. 2010, *20* (29), 5983-5992.

26. Kaul, A. B. J. J. o. M. R., Two-dimensional layered materials: Structure, properties, and prospects for device applications. 2014, *29* (3), 348-361.

27. Yang, X.; Zhang, R.; Pu, J.; He, Z.; Xiong, L. J. C. R., 2D graphene and h-BN layers application in protective coatings. 2021, *39* (2), 93-107.

28. Manzeli, S.; Ovchinnikov, D.; Pasquier, D.; Yazyev, O. V.; Kis, A. J. N. R. M., 2D transition metal dichalcogenides. 2017, *2* (8), 1-15.

29. Ataca, C.; Sahin, H.; Ciraci, S. J. T. J. o. P. C. C., Stable, single-layer MX2 transition-metal oxides and dichalcogenides in a honeycomb-like structure. 2012, *116* (16), 8983-8999.

30. Chhowalla, M.; Shin, H. S.; Eda, G.; Li, L.-J.; Loh, K. P.; Zhang, H. J. N. c., The chemistry of two-dimensional layered transition metal dichalcogenide nanosheets. 2013, *5* (4), 263-275.

31. Fu, Q.; Han, J.; Wang, X.; Xu, P.; Yao, T.; Zhong, J.; Zhong, W.; Liu, S.; Gao, T.; Zhang, Z. J. A. M., 2D transition metal dichalcogenides: Design, modulation, and challenges in electrocatalysis. 2021, *33* (6), 1907818.

32. Xiao, Y.; Tan, M.; Li, Z.; He, L.; Gao, B.; Chen, Y.; Zheng, Y.; Lin, B. J. I. J. o. H. E., Ethylenediamine-assisted phase engineering of 1T/2H–MoS2/graphene for efficient and stable electrocatalytic hydrogen evolution. 2021, *46* (21), 11688-11700.

33. Cong, C.; Shang, J.; Wang, Y.; Yu, T. J. A. O. M., Optical properties of 2D semiconductor WS2. 2018, *6* (1), 1700767.

34. Tareen, A. K.; Khan, K.; Rehman, S.; Iqbal, M.; Yu, J.; Zhou, Z.; Yin, J.; Zhang, H. J. P. i. S. S. C., Recent development in emerging phosphorene based novel materials: Progress, challenges, prospects and their fascinating sensing applications. 2021, 100336.

35. Sorkin, V.; Pan, H.; Shi, H.; Quek, S.; Zhang, Y. J. C. r. i. s. s.; sciences, m., Nanoscale transition metal dichalcogenides: structures, properties, and applications. 2014, *39* (5), 319-367.

36. An, S.-J.; Kim, Y. H.; Lee, C.; Park, D. Y.; Jeong, M. S. J. S. r., Exfoliation of transition metal dichalcogenides by a high-power femtosecond laser. 2018, *8* (1), 1-6.

37. Li, R.; Cheng, Y.; Huang, W. J. S., Recent progress of Janus 2D transition metal chalcogenides: from theory to experiments. 2018, *14* (45), 1802091.

38. Mendes, R. G.; Pang, J.; Bachmatiuk, A.; Ta, H. Q.; Zhao, L.; Gemming, T.; Fu, L.; Liu, Z.; Rümmeli, M. H. J. A. n., Electron-driven in situ transmission electron microscopy of 2D transition metal dichalcogenides and their 2D heterostructures. 2019, *13* (2), 978-995.

39. Lv, R.; Robinson, J. A.; Schaak, R. E.; Sun, D.; Sun, Y.; Mallouk, T. E.; Terrones, M. J. A. o. c. r., Transition metal dichalcogenides and beyond: synthesis, properties, and applications of single-and few-layer nanosheets. 2015, *48* (1), 56-64.

40. Zhao, W.; Ribeiro, R. M.; Eda, G. J. A. o. c. r., Electronic structure and optical signatures of semiconducting transition metal dichalcogenide nanosheets. 2015, *48* (1), 91-99.

41. Taghinejad, H.; Taghinejad, M.; Eftekhar, A. A.; Li, Z.; West, M. P.; Javani, M. H.; Abdollahramezani, S.; Zhang, X.; Tian, M.; Johnson-Averette, T. J. A. N., Synthetic

engineering of morphology and electronic band gap in lateral heterostructures of monolayer transition metal dichalcogenides. 2020, *14* (5), 6323-6330.

42. Van Thanh, V.; Van, N. D.; Saito, R.; Hung, N. T. J. A. S. S., First-principles study of mechanical, electronic and optical properties of Janus structure in transition metal dichalcogenides. 2020, *526*, 146730.

43. Choi, C. L.; Feng, J.; Li, Y.; Wu, J.; Zak, A.; Tenne, R.; Dai, H. J. N. R., WS2 nanoflakes from nanotubes for electrocatalysis. 2013, *6* (12), 921-928.

44. Walsh, L. A.; Hinkle, C. L. J. A. M. T., van der Waals epitaxy: 2D materials and topological insulators. 2017, *9*, 504-515.

45. Choi, W.; Choudhary, N.; Han, G. H.; Park, J.; Akinwande, D.; Lee, Y. H. J. M. T., Recent development of two-dimensional transition metal dichalcogenides and their applications. 2017, *20* (3), 116-130.

46. Di Bartolomeo, A. J. N., Emerging 2D materials and their van der Waals heterostructures. Multidisciplinary Digital Publishing Institute: 2020; Vol. 10, p 579.

47. Hong, M.-K.; Hyun, S.-H.; Jang, H.-S.; An, B.-S.; Jang, H.-C.; Hwang, H.-S.; Kim, S.-I.; Moon, J.-Y.; Sattari-Esfahlan, S. M.; Lee, S.-Y. J. A. S. S., Controlled growth of in-plane graphene/h-BN heterostructure on a single crystal Ge substrate. 2021, *554*, 149655.

48. Gao, S.; Wang, Z.; Wang, H.; Meng, F.; Wang, P.; Chen, S.; Zeng, Y.; Zhao, J.; Hu, H.; Cao, R. J. A. M. I., Graphene/MoS2/Graphene Vertical Heterostructure-Based Broadband Photodetector with High Performance. 2021, *8* (3), 2001730.

49. Ebnonnasir, A.; Narayanan, B.; Kodambaka, S.; Ciobanu, C. V. J. A. P. L., Tunable MoS2 bandgap in MoS2-graphene heterostructures. 2014, *105* (3), 031603.

50. Fu, C.-F.; Li, X.; Yang, J. J. C. s., A rationally designed two-dimensional MoSe 2/Ti 2 CO 2 heterojunction for photocatalytic overall water splitting: simultaneously suppressing electron–hole recombination and photocorrosion. 2021, *12* (8), 2863-2869.

51. Iannaccone, G.; Bonaccorso, F.; Colombo, L.; Fiori, G. J. N. n., Quantum engineering of transistors based on 2D materials heterostructures. 2018, *13* (3), 183-191.

52. Butler, S. Z.; Hollen, S. M.; Cao, L.; Cui, Y.; Gupta, J. A.; Gutiérrez, H. R.; Heinz, T. F.; Hong, S. S.; Huang, J.; Ismach, A. F. J. A. n., Progress, challenges, and opportunities in two-dimensional materials beyond graphene. 2013, *7* (4), 2898-2926.

53. Da Silva, J. F.; Williams, R. J. P., *The biological chemistry of the elements: the inorganic chemistry of life*. Oxford University Press: 2001.

54. See, C. H.; Harris, A. T. J. I.; research, e. c., A review of carbon nanotube synthesis via fluidized-bed chemical vapor deposition. 2007, *46* (4), 997-1012.

55. Falcao, E. H.; Wudl, F. J. J. o. C. T.; Biotechnology: International Research in Process, E.; Technology, C., Carbon allotropes: beyond graphite and diamond. 2007, *82* (6), 524-531.

56. Li, K.; Liu, Q.; Cheng, H.; Hu, M.; Zhang, S. J. S. A. P. A. M.; Spectroscopy, B., Classification and carbon structural transformation from anthracite to natural coaly graphite by XRD, Raman spectroscopy, and HRTEM. 2021, *249*, 119286.

57. Lian, P.; Zhu, X.; Liang, S.; Li, Z.; Yang, W.; Wang, H. J. E. A., Large reversible capacity of high quality graphene sheets as an anode material for lithium-ion batteries. 2010, *55* (12), 3909-3914.

58. Neto, A. C.; Guinea, F.; Peres, N. M. J. P. w., Drawing conclusions from graphene. 2006, *19* (11), 33.

59. Randviir, E. P.; Brownson, D. A.; Banks, C. E. J. M. T., A decade of graphene research: production, applications and outlook. 2014, *17* (9), 426-432.

60. Usachov, D.; Fedorov, A.; Otrokov, M. M.; Chikina, A.; Vilkov, O.; Petukhov, A.; Rybkin, A. G.; Koroteev, Y. M.; Chulkov, E. V.; Adamchuk, V. K. J. N. l., Observation of single-spin Dirac fermions at the graphene/ferromagnet interface. 2015, *15* (4), 2396-2401.

61. Ghahari Kermani, F. Interaction Effects on Electric and Thermoelectric Transport in Graphene. Columbia University, 2014.

62. Xie, X.; Zhou, Y.; Bi, H.; Yin, K.; Wan, S.; Sun, L. J. S. r., Large-range control of the microstructures and properties of three-dimensional porous graphene. 2013, *3* (1), 1-6.

63. Gong, C.; Lee, G.; Shan, B.; Vogel, E. M.; Wallace, R. M.; Cho, K. J. J. o. A. P., First-principles study of metal–graphene interfaces. 2010, *108* (12), 123711.

64. Moon, P.; Koshino, M. J. P. R. B., Electronic properties of graphene/hexagonal-boron-nitride moiré superlattice. 2014, *90* (15), 155406.

65. Marsden, A. J.; Brommer, P.; Mudd, J. J.; Dyson, M. A.; Cook, R.; Asensio, M.; Avila, J.; Levy, A.; Sloan, J.; Quigley, D. J. N. R., Effect of oxygen and nitrogen functionalization on the physical and electronic structure of graphene. 2015, *8* (8), 2620-2635.

66. Neto, A. C.; Guinea, F.; Peres, N. M.; Novoselov, K. S.; Geim, A. K. J. R. o. m. p., The electronic properties of graphene. 2009, *81* (1), 109.

67. Petersen, R.; Pedersen, T. G.; Jauho, A.-P. J. A. N., Clar sextet analysis of triangular, rectangular, and honeycomb graphene antidot lattices. 2011, *5* (1), 523-529.

68. Nam, N. N.; Koshino, M. J. P. R. B., Lattice relaxation and energy band modulation in twisted bilayer graphene. 2017, *96* (7), 075311.

69. Ho, S.-T.; Le, H. A.; Nguyen, V. D.; Do, V.-N. J. T. E. P. J. B., Electronic properties of slid bilayer graphene: effective models in low energy range. 2020, *93* (10), 1-9.

70. Belenkov, M. E.; Chernov, V. M. J. H. ф., химия, математика, Dependence of the electronic and crystal structure of a functionalized graphene on the concentration of chemically adsorbed fluorine. 2020, *11* (6), 685-689.

71. Kalesaki, E.; Delerue, C.; Smith, C. M.; Beugeling, W.; Allan, G.; Vanmaekelbergh, D. J. P. r. x., Dirac cones, topological edge states, and nontrivial flat bands in two-dimensional semiconductors with a honeycomb nanogeometry. 2014, *4* (1), 011010.

72. Papageorgiou, D. G.; Kinloch, I. A.; Young, R. J. J. P. i. M. S., Mechanical properties of graphene and graphene-based nanocomposites. 2017, *90*, 75-127.

73. Lee, C.; Wei, X.; Kysar, J. W.; Hone, J. J. s., Measurement of the elastic properties and intrinsic strength of monolayer graphene. 2008, *321* (5887), 385-388.

74. Novoselov, K.; Morozov, S.; Mohinddin, T.; Ponomarenko, L.; Elias, D.; Yang, R.; Barbolina, I.; Blake, P.; Booth, T.; Jiang, D. J. p. s. s., Electronic properties of graphene. 2007, *244* (11), 4106-4111.

75. Du, X.; Skachko, I.; Barker, A.; Andrei, E. Y. J. N. n., Approaching ballistic transport in suspended graphene. 2008, *3* (8), 491-495.

76. Xiong, F.; Zhang, J.; Zhu, Z.; Yuan, X.; Qin, S. J. S. r., Ultrabroadband, more than one order absorption enhancement in graphene with plasmonic light trapping. 2015, *5* (1), 1-8.

77. Nika, D. In *Phonon thermal conductivity in graphene*, Central and Eastern European Conference on Thermal Analysis and Calorimetry, 2017; pp 56-56.

78. Wei, D.; Liu, Y. J. A. M., Controllable synthesis of graphene and its applications. 2010, *22* (30), 3225-3241.

79. Lancellotti, L.; Polichetti, T.; Ricciardella, F.; Tari, O.; Gnanapragasam, S.; Daliento, S.; Di Francia, G. J. T. S. F., Graphene applications in Schottky barrier solar cells. 2012, *522*, 390-394.

80. Kwak, Y. H.; Choi, D. S.; Kim, Y. N.; Kim, H.; Yoon, D. H.; Ahn, S.-S.; Yang, J.-W.; Yang, W. S.; Seo, S. J. B.; Bioelectronics, Flexible glucose sensor using CVD-grown graphene-based field effect transistor. 2012, *37* (1), 82-87.

81. Sun, L.; Li, S.; Ding, W.; Yao, Y.; Yang, X.; Yao, C. J. J. o. M. C. B., Fluorescence detection of cholesterol using a nitrogen-doped graphene quantum dot/chromium picolinate complex-based sensor. 2017, *5* (45), 9006-9014.

82. Sharma, A. K.; Gupta, J. J. O. F. T., Graphene based chalcogenide fiber-optic evanescent wave sensor for detection of hemoglobin in human blood. 2018, *41*, 125-130.

83. Shen, H.; Zhang, L.; Liu, M.; Zhang, Z. J. T., Biomedical applications of graphene. 2012, *2* (3), 283.

84. Guo, S.; Chen, J.; Zhang, Y.; Liu, J. J. N., Graphene-Based Films: Fabrication, Interfacial Modification, and Applications. 2021, *11* (10), 2539.

85. Zhang, X.; Rajaraman, B. R.; Liu, H.; Ramakrishna, S. J. R. A., Graphene's potential in materials science and engineering. 2014, *4* (55), 28987-29011.

86. ElMekawy, A.; Hegab, H. M.; Losic, D.; Saint, C. P.; Pant, D. J. R.; Reviews, S. E., Applications of graphene in microbial fuel cells: the gap between promise and reality. 2017, *72*, 1389-1403.

87. Wang, J.; Sun, J.; Wang, J.; Liu, H.; Xue, J.; Nie, Z. J. C. C., Hexagonal boron nitride nanosheets as a multifunctional background-free matrix to detect small molecules and complicated samples by MALDI mass spectrometry. 2017, *53* (58), 8114-8117.

88. Bernard, S.; Miele, P. J. M., Polymer-derived boron nitride: A review on the chemistry, shaping and ceramic conversion of borazine derivatives. 2014, *7* (11), 7436-7459.

89. Shuaibu, A.; Adeyemi, O. J.; Ushiekpan, U. R.; Olowomofe, O. G.; Akinade, B. J.; Kafayat, O. A. J. A. J. o. C. M. P., First Principle Study of Structural, Elastic and Electronic Properties of Hexagonal Boron Nitride (hex-BN) Single Layer. 2019, *9* (1), 1-5.

90. Juma, I. G.; Kim, G.; Jariwala, D.; Behura, S. K. J. I., Direct growth of hexagonal boron nitride on non-metallic substrates and its heterostructures with graphene. 2021, *24* (11), 103374.

91. Maqbool, M., *Growth, characterization and luminescence and optical properties of rare-earth elements and transition metals doped in wide bandgap nitride semiconductors*. Ohio University: 2005.

92. Zheng, Z.; Cox, M.; Li, B. J. J. o. M. S., Surface modification of hexagonal boron nitride nanomaterials: a review. 2018, *53* (1), 66-99.

93. Alruqi, A., 2D materials based heterostructures: a lithography free method. 2019.

94. Topsakal, M.; Aktürk, E.; Ciraci, S. J. P. R. B., First-principles study of two-and one-dimensional honeycomb structures of boron nitride. 2009, *79* (11), 115442.

95. Lin, Y.; Connell, J. W. J. N., Advances in 2D boron nitride nanostructures: nanosheets, nanoribbons, nanomeshes, and hybrids with graphene. 2012, *4* (22), 6908-6939.

96. Hibino, H.; Wang, S.; Orofeo, C.; Kageshima, H. J. P. i. C. G.; Materials, C. o., Growth and low-energy electron microscopy characterizations of graphene and hexagonal boron nitride. 2016, *62* (2), 155-176.

97. Mali, K. S.; Greenwood, J.; Adisoejoso, J.; Phillipson, R.; De Feyter, S. J. N., Nanostructuring graphene for controlled and reproducible functionalization. 2015, *7* (5), 1566-1585.

98. Bhimanapati, G. R.; Lin, Z.; Meunier, V.; Jung, Y.; Cha, J.; Das, S.; Xiao, D.; Son, Y.; Strano, M. S.; Cooper, V. R. J. A. n., Recent advances in two-dimensional materials beyond graphene. 2015, *9* (12), 11509-11539.

99. Han, W., Two-Dimensional Materials for Electronic Applications., in Department of Electrical Engineering and Computer Science. 2013, Massachusetts Institute of Technology. . p. 232.

100. Xu, M.; Liang, T.; Shi, M.; Chen, H. J. C. r., Graphene-like two-dimensional materials. 2013, *113* (5), 3766-3798.

101. Akhtar, M.; Anderson, G.; Zhao, R.; Alruqi, A.; Mroczkowska, J. E.; Sumanasekera, G.; Jasinski, J. B. J. n. D. M.; Applications, Recent advances in synthesis, properties, and applications of phosphorene. 2017, *1* (1), 1-13.

102. Akinwande, D.; Huyghebaert, C.; Wang, C.-H.; Serna, M. I.; Goossens, S.; Li, L.-J.; Wong, H.-S. P.; Koppens, F. H. J. N., Graphene and two-dimensional materials for silicon technology. 2019, *573* (7775), 507-518.

103. Fang, X.; Fan, L.-W.; Ding, Q.; Yao, X.-L.; Wu, Y.-Y.; Hou, J.-F.; Wang, X.; Yu, Z.-T.; Cheng, G.-H.; Hu, Y.-C. J. E. c.; management, Thermal energy storage performance of paraffin-based composite phase change materials filled with hexagonal boron nitride nanosheets. 2014, *80*, 103-109.

104. Dankert, A.; Karpiak, B.; Dash, S. P. J. S. r., Hall sensors batch-fabricated on all-CVD h-BN/graphene/h-BN heterostructures. 2017, *7* (1), 1-7.

105. Pattison, P.; Tsao, J.; Brainard, G.; Bugbee, B. J. N., LEDs for photons, physiology and food. 2018, *563* (7732), 493-500.

106. Pisek, E.; Rajagopal, S.; Abu-Surra, S. In *Gigabit rate mobile connectivity through visible light communication*, 2012 IEEE International Conference on Communications (ICC), IEEE: 2012; pp 3122-3127.

107. Moustakas, T. D.; Paiella, R. J. R. o. P. i. P., Optoelectronic device physics and technology of nitride semiconductors from the UV to the terahertz. 2017, *80* (10), 106501.

108. Moustakas, T. D.; Liao, Y.; Kao, C.-k.; Thomidis, C.; Bhattacharyya, A.; Bhattarai, D.; Moldawer, A. In *Deep UV-LEDs with high IQE based on AlGaN alloys with strong band structure potential fluctuations*, Light-Emitting Diodes: Materials, Devices, and Applications for Solid State Lighting XVI, International Society for Optics and Photonics: 2012; p 82780L.

109. Ginzburg, V., Bill Little and high temperature superconductivity. In *From High-Temperature Superconductivity to Microminiature Refrigeration*, Springer: 1996; pp 277-285.

110. Yakhmi, J. V. J. S. M.; Applications, T., Introduction to superconductivity, superconducting materials and their usefulness.

111. Hirsch, J. J. P. S., BCS theory of superconductivity: it is time to question its validity. 2009, *80* (3), 035702.

112. Pešić, J. R. J. У. у. Б., Investigation of superconductivity in graphene and related materials using AB-initio methods. 2017.

113. Bud'Ko, S.; Lapertot, G.; Petrovic, C.; Cunningham, C.; Anderson, N.; Canfield, P. J. P. R. L., Boron isotope effect in superconducting MgB 2. 2001, *86* (9), 1877.

114. Slusky, J.; Rogado, N.; Regan, K.; Hayward, M.; Khalifah, P.; He, T.; Inumaru, K.; Loureiro, S.; Haas, M.; Zandbergen, H. J. N., Loss of superconductivity with the addition of Al to MgB2 and a structural transition in Mg1-x AlxB2. 2001, *410* (6826), 343-345.

115. Canfield, P. C.; Crabtree, G. W. J. P. T., Magnesium diboride: better late than never. 2003, *56* (3), 34-40.

116. Zeng, X.; Pogrebnyakov, A. V.; Kotcharov, A.; Jones, J. E.; Xi, X.; Lysczek, E. M.; Redwing, J. M.; Xu, S.; Li, Q.; Lettieri, J. J. N. m., In situ epitaxial MgB2 thin films for superconducting electronics. 2002, *1* (1), 35-38.

117. Berkinbayeva, A. S.; Alipbaev, A. N.; Mussina, Z. M. In *PREPARATION OF SUPERCONDUCTING MAGNESIUM DIBORIDE BASED ON MAGNESIUM-*

*THERMAL BORON OXIDE*, Actual Questions and Innovations in Science 2, 2019; pp 162-164.

118. Varshney, D. J. S. S.; Technology, Impurity, phonon and electron contributions to the electrical resistivity of single-crystal MgB2. 2006, *19* (8), 685.

119. Zhang, X.; Qiao, X.-F.; Shi, W.; Wu, J.-B.; Jiang, D.-S.; Tan, P.-H. J. C. S. R., Phonon and Raman scattering of two-dimensional transition metal dichalcogenides from monolayer, multilayer to bulk material. 2015, *44* (9), 2757-2785.

120. Dong, R.; Zhang, T.; Feng, X. J. C. r., Interface-assisted synthesis of 2D materials: trend and challenges. 2018, *118* (13), 6189-6235.

121. You, J.; Hossain, M. D.; Luo, Z. J. N. C., Synthesis of 2D transition metal dichalcogenides by chemical vapor deposition with controlled layer number and morphology. 2018, *5* (1), 1-13.

122. Mahyavanshi, R. D.; Kalita, G.; Sharma, K. P.; Kondo, M.; Dewa, T.; Kawahara, T.; Tanemura, M. J. A. S. S., Synthesis of MoS2 ribbons and their branched structures by chemical vapor deposition in sulfur-enriched environment. 2017, *409*, 396-402.

123. Hernandez Ruiz, K.; Wang, Z.; Ciprian, M.; Zhu, M.; Tu, R.; Zhang, L.; Luo, W.; Fan, Y.; Jiang, W. J. S. S., Chemical Vapor Deposition Mediated Phase Engineering for 2D Transition Metal Dichalcogenides: Strategies and Applications. 2022, *2* (1), 2100047.

124. Song, X.; Guo, Z.; Zhang, Q.; Zhou, P.; Bao, W.; Zhang, D. W. J. S., Progress of Large-Scale Synthesis and Electronic Device Application of Two-Dimensional Transition Metal Dichalcogenides. 2017, *13* (35), 1700098.

125. Nan, Z. Electronic properties of MoS2/MoSe2 van der Waals heterostructures. INSA/University of Toulouse, 2020.

126. Anderson, G., Synthesis, characterization, and electronic properties of novel 2D materials: transition metal dichalcogenides and phosphorene. 2016.

127. Chen, Y.; Li, L.; Guo, L. J. C., Two-Dimensional Metal-Containing Nanomaterials for Battery Anode Applications. 2020, *7* (15), 3193-3210.

128. Gor, G. Y.; Cannarella, J.; Leng, C. Z.; Vishnyakov, A.; Arnold, C. B. J. J. o. P. S., Swelling and softening of lithium-ion battery separators in electrolyte solvents. 2015, *294*, 167-172.

129. Utschig, T.; Corradini, M. J. F. T. I., University of Wisconsin report UWFDM-, Computer modeling for lithium safety in fusion systems: LINT and MELCOR. 1999.

130. Pointing, S. B. J. F. d., Qualitative methods for the determination of lignocellulolytic enzyme production by tropical fungi. 1999.

131. Shillcock, J. C.; Lipowsky, R. J. T. J. o. c. p., Equilibrium structure and lateral stress distribution of amphiphilic bilayers from dissipative particle dynamics simulations. 2002, *117* (10), 5048-5061.

132. Brownson, D. A.; Banks, C. E. J. A., Graphene electrochemistry: an overview of potential applications. 2010, *135* (11), 2768-2778.

133. Kalita, G.; Tanemura, M. J. G. M.-A. A., Fundamentals of chemical vapor deposited graphene and emerging applications. 2017, 30-35.

134. Britnell, L.; Gorbachev, R.; Jalil, R.; Belle, B.; Schedin, F.; Mishchenko, A.; Georgiou, T.; Katsnelson, M.; Eaves, L.; Morozov, S. J. S., Field-effect tunneling transistor based on vertical graphene heterostructures. 2012, *335* (6071), 947-950.

135. Novoselov, K. S.; Geim, A. K.; Morozov, S. V.; Jiang, D.-e.; Zhang, Y.; Dubonos, S. V.; Grigorieva, I. V.; Firsov, A. A. J. s., Electric field effect in atomically thin carbon films. 2004, *306* (5696), 666-669.

136. Yi, M.; Shen, Z. J. J. o. M. C. A., A review on mechanical exfoliation for the scalable production of graphene. 2015, *3* (22), 11700-11715.

137. Wu, Z.-S.; Ren, W.; Gao, L.; Liu, B.; Zhao, J.; Cheng, H.-M. J. N. R., Efficient synthesis of graphene nanoribbons sonochemically cut from graphene sheets. 2010, *3* (1), 16-22.

138. Thayer, G.; Hannon, J.; Tromp, R. J. N. M., Shape and stability of self-assembled surface domains. 2004, *3* (2), 95-98.

139. Zhang, Y.; Small, J. P.; Pontius, W. V.; Kim, P. J. A. P. L., Fabrication and electric-field-dependent transport measurements of mesoscopic graphite devices. 2005, *86* (7), 073104.

140. Ci, L.; Song, L.; Jariwala, D.; Elías, A. L.; Gao, W.; Terrones, M.; Ajayan, P. M. J. A. M., Graphene shape control by multistage cutting and transfer. 2009, *21* (44), 4487-4491.

141. Liang, X.; Fu, Z.; Chou, S. Y. J. N. l., Graphene transistors fabricated via transfer-printing in device active-areas on large wafer. 2007, *7* (12), 3840-3844.

142. Sinclair, R. C.; Suter, J. L.; Coveney, P. V. J. P. C. C. P., Micromechanical exfoliation of graphene on the atomistic scale. 2019, *21* (10), 5716-5722.

143. Johal, S. Chemical Exfoliation of graphene and other 2D-materials. The University of Manchester (United Kingdom), 2013.

144. Coleman, J. N. J. A. o. c. r., Liquid exfoliation of defect-free graphene. 2013, *46* (1), 14-22.

145. Güler, Ö.; Tekeli, M.; Taşkın, M.; Güler, S. H.; Yahia, I. J. C. I., The production of graphene by direct liquid phase exfoliation of graphite at moderate sonication power by using low boiling liquid media: The effect of liquid media on yield and optimization. 2021, *47* (1), 521-533.

146. Hamilton, C. E.; Lomeda, J. R.; Sun, Z.; Tour, J. M.; Barron, A. R. J. N. l., High-yield organic dispersions of unfunctionalized graphene. 2009, *9* (10), 3460-3462.

147. Singh, R.; Kumar, D.; Tripathi, C. J. P. C. S., Concentration enhancement of liquid phase exfoliated graphene with addition of organic salts. 2015, *70*, 565-571.

148. Petrone, N.; Dean, C. R.; Meric, I.; Van Der Zande, A. M.; Huang, P. Y.; Wang, L.; Muller, D.; Shepard, K. L.; Hone, J. J. N. l., Chemical vapor deposition-derived graphene with electrical performance of exfoliated graphene. 2012, *12* (6), 2751-2756.

149. Gambhir, S.; Jalili, R.; Officer, D. L.; Wallace, G. G. J. N. A. M., Chemically converted graphene: scalable chemistries to enable processing and fabrication. 2015, *7* (6), e186-e186.

150. Liu, X.; Zheng, M.; Xiao, K.; Xiao, Y.; He, C.; Dong, H.; Lei, B.; Liu, Y. J. N., Simple, green and high-yield production of single-or few-layer graphene by hydrothermal exfoliation of graphite. 2014, *6* (9), 4598-4603.

151. Hadi, A.; Karimi-Sabet, J.; Moosavian, S. M. A.; Ghorbanian, S. J. T. J. o. S. F., Optimization of graphene production by exfoliation of graphite in supercritical ethanol: A response surface methodology approach. 2016, *107*, 92-105.

152. Berger, C.; Song, Z.; Li, X.; Wu, X.; Brown, N.; Naud, C.; Mayou, D.; Li, T.; Hass, J.; Marchenkov, A. N. J. S., Electronic confinement and coherence in patterned epitaxial graphene. 2006, *312* (5777), 1191-1196.

153. Al-Gaashani, R.; Najjar, A.; Zakaria, Y.; Mansour, S.; Atieh, M. J. C. I., XPS and structural studies of high quality graphene oxide and reduced graphene oxide prepared by different chemical oxidation methods. 2019, *45* (11), 14439-14448.

154. Obraztsov, A. N. J. N. n., Making graphene on a large scale. 2009, *4* (4), 212-213.

155. Zhang, M.; Hou, C.; Halder, A.; Wang, H.; Chi, Q. J. M. C. F., Graphene papers: smart architecture and specific functionalization for biomimetics, electrocatalytic sensing and energy storage. 2017, *1* (1), 37-60.

156. Duffy, E. Carbonaceous nanoparticles and carbon on carbon composite materials: preparation, properties and application in adsorption. University of Tasmania, 2015.

157. Huang, H.; Chen, S.; Wee, A.; Chen, W., Epitaxial growth of graphene on silicon carbide (SiC). In *Graphene*, Elsevier: 2014; pp 177-198.

158. Kotsakidis, J. C.; Currie, M.; Grubišić-Čabo, A.; Tadich, A.; Myers-Ward, R. L.; DeJarld, M.; Daniels, K. M.; Liu, C.; Edmonds, M. T.; Vázquez de Parga, A. L. J. A. M. I., Increasing the Rate of Magnesium Intercalation Underneath Epitaxial Graphene on 6H-SiC (0001). 2021, *8* (23), 2101598.

159. Juang, Z.-Y.; Wu, C.-Y.; Lo, C.-W.; Chen, W.-Y.; Huang, C.-F.; Hwang, J.-C.; Chen, F.-R.; Leou, K.-C.; Tsai, C.-H. J. C., Synthesis of graphene on silicon carbide substrates at low temperature. 2009, *47* (8), 2026-2031.

160. Zhang, J.; Tan, B.; Zhang, X.; Gao, F.; Hu, Y.; Wang, L.; Duan, X.; Yang, Z.; Hu, P. J. A. M., Atomically thin hexagonal boron nitride and its heterostructures. 2021, *33* (6), 2000769.

161. Chatterjee, S.; Luo, Z.; Acerce, M.; Yates, D. M.; Johnson, A. C.; Sneddon, L. G. J. C. o. m., Chemical vapor deposition of boron nitride nanosheets on metallic substrates via decaborane/ammonia reactions. 2011, *23* (20), 4414-4416.

162. Mohammadi, F. M., *Chemical Vapour Deposition Growth of Graphene and Hexagonal Boron Nitride, and a Study of the Electronic and Corrosion Inhibiting Properties of Hexagonal Boron Nitride*. McGill University (Canada): 2018.

163. Warner, J. H.; Rummeli, M. H.; Bachmatiuk, A.; Buchner, B. J. A. n., Atomic resolution imaging and topography of boron nitride sheets produced by chemical exfoliation. 2010, *4* (3), 1299-1304.

164. Shen, J.; He, Y.; Wu, J.; Gao, C.; Keyshar, K.; Zhang, X.; Yang, Y.; Ye, M.; Vajtai, R.; Lou, J. J. N. l., Liquid phase exfoliation of two-dimensional materials by directly probing and matching surface tension components. 2015, *15* (8), 5449-5454.

165. Wen, Y.; Shang, X.; Dong, J.; Xu, K.; He, J.; Jiang, C. J. N., Ultraclean and large-area monolayer hexagonal boron nitride on Cu foil using chemical vapor deposition. 2015, *26* (27), 275601.

166. Babenko, V.; Lane, G.; Koos, A. A.; Murdock, A. T.; So, K.; Britton, J.; Meysami, S. S.; Moffat, J.; Grobert, N. J. S. r., Time dependent decomposition of ammonia borane for the controlled production of 2D hexagonal boron nitride. 2017, *7* (1), 1-12.

167. Bouvron, S. Gate-controlled scanning tunneling spectroscopy of CoPc molecules on graphene. 2014.

168. Camilli, L.; Sutter, E.; Sutter, P. J. D. M., Growth of two-dimensional materials on non-catalytic substrates: h-BN/Au (111). 2014, *1* (2), 025003.

169. Acacia, N.; Fazio, E.; Neri, F.; Ossi, P. M.; Trusso, S.; Santo, N. J. R. E.; Solids, D. i., Pulsed laser deposition of boron nitride thin films. 2008, *163* (4-6), 293-298.

170. Glavin, N. R.; Jespersen, M. L.; Check, M. H.; Hu, J.; Hilton, A. M.; Fisher, T. S.; Voevodin, A. A. *Synthesis of Few-Layer, Large Area Hexagonal-Boron Nitride by Pulsed Laser Deposition (POSTPRINT)*; AIR FORCE RESEARCH LAB WRIGHT-PATTERSON AFB OH FUNCTIONAL MATERIALS DIV: 2014.

171. Li, C.; Cao, Q.; Wang, F.; Xiao, Y.; Li, Y.; Delaunay, J.-J.; Zhu, H. J. C. S. R., Engineering graphene and TMDs based van der Waals heterostructures for photovoltaic and photoelectrochemical solar energy conversion. 2018, *47* (13), 4981-5037.

172. Foley, B. M.; Hernández, S. C.; Duda, J. C.; Robinson, J. T.; Walton, S. G.; Hopkins, P. E. J. N. l., Modifying surface energy of graphene via plasma-based chemical functionalization to tune thermal and electrical transport at metal interfaces. 2015, *15* (8), 4876-4882.

173. Perrozzi, F.; Emamjomeh, S. M.; Paolucci, V.; Taglieri, G.; Ottaviano, L.; Cantalini, C. J. S.; Chemical, A. B., Thermal stability of WS2 flakes and gas sensing properties of WS2/WO3 composite to H2, NH3 and NO2. 2017, *243*, 812-822.

174. Capasso, F. J. S., Band-gap engineering: from physics and materials to new semiconductor devices. 1987, *235* (4785), 172-176.

175. Wang, Q. H.; Kalantar-Zadeh, K.; Kis, A.; Coleman, J. N.; Strano, M. S. J. N. n., Electronics and optoelectronics of two-dimensional transition metal dichalcogenides. 2012, *7* (11), 699-712.

176. Zhu, H.; Gan, X.; McCreary, A.; Lv, R.; Lin, Z.; Terrones, M. J. N. T., Heteroatom doping of two-dimensional materials: from graphene to chalcogenides. 2020, *30*, 100829.

177. Swarnkar, A.; Mir, W. J.; Nag, A. J. A. E. L., Can B-site doping or alloying improve thermal-and phase-stability of all-inorganic CsPbX3 (X= Cl, Br, I) perovskites? 2018, *3* (2), 286-289.

178. Lin, Y. C.; Dumcenco, D. O.; Komsa, H. P.; Niimi, Y.; Krasheninnikov, A. V.; Huang, Y. S.; Suenaga, K. J. A. m., Properties of individual dopant atoms in single-layer MoS2: atomic structure, migration, and enhanced reactivity. 2014, *26* (18), 2857-2861.

179. Armitage, N.; Ronning, F.; Lu, D.; Kim, C.; Damascelli, A.; Shen, K.; Feng, D.; Eisaki, H.; Shen, Z.-X.; Mang, P. J. P. R. L., Doping dependence of an n-type cuprate superconductor investigated by angle-resolved photoemission spectroscopy. 2002, *88* (25), 257001.

180. Tikhonenko, F.; Kozikov, A.; Savchenko, A.; Gorbachev, R. J. P. R. L., Transition between electron localization and antilocalization in graphene. 2009, *103* (22), 226801.

181. Liu, W.; Sarkar, D.; Kang, J.; Cao, W.; Banerjee, K. J. A. N., Impact of contact on the operation and performance of back-gated monolayer MoS2 field-effect-transistors. 2015, *9* (8), 7904-7912.

182. Usachov, D. Y.; Fedorov, A.; Vilkov, O. Y.; Senkovskiy, B.; Adamchuk, V.; Andryushechkin, B.; Vyalikh, D. J. P. o. t. S. S., Synthesis and electronic structure of nitrogen-doped graphene. 2013, *55* (6), 1325-1332.

183. Tsai, H.-S.; Lai, C.-C.; Hsiao, C.-H.; Medina, H.; Su, T.-Y.; Ouyang, H.; Chen, T.-H.; Liang, J.-H.; Chueh, Y.-L. J. A. a. m.; interfaces, Plasma-assisted synthesis of high-mobility atomically layered violet phosphorus. 2015, *7* (25), 13723-13727.

184. Rani, P.; Jindal, V. J. R. a., Designing band gap of graphene by B and N dopant atoms. 2013, *3* (3), 802-812.

185. Coey, J.; Chambers, S. J. M. b., Oxide dilute magnetic semiconductors—fact or fiction? 2008, *33* (11), 1053-1058.

186. Wei, D.; Wu, B.; Guo, Y.; Yu, G.; Liu, Y. J. A. o. c. r., Controllable chemical vapor deposition growth of few layer graphene for electronic devices. 2013, *46* (1), 106-115.

187. Zhan, Y.; Liu, Z.; Najmaei, S.; Ajayan, P. M.; Lou, J. J. s., Large-area vapor-phase growth and characterization of MoS2 atomic layers on a SiO2 substrate. 2012, *8* (7), 966-971.

188. Alferov, Z. I. J. S., The history and future of semiconductor heterostructures. 1998, *32* (1), 1-14.

189. Tartakovskii, A. J. N. R. P., Excitons in 2D heterostructures. 2020, *2* (1), 8-9.

190. Thompson, A.; Stall, R.; Kroll, W.; Armour, E.; Beckham, C.; Zawadzki, P.; Aina, L.; Siepel, K. J. J. o. c. g., Large scale manufacturing of compound semiconductors by MOVPE. 1997, *170* (1-4), 92-96.

191. Hamedani, Y.; Macha, P.; Bunning, T. J.; Naik, R. R.; Vasudev, M. C. J. C. V. D.-R. A.; Applications in Optical, S. C.; Devices, S. S., Plasma-enhanced chemical vapor deposition: Where we are and the outlook for the future. 2016, *4*, 243-280.

192. Charitidis, C. J. I. J. o. R. M.; Materials, H., Nanomechanical and nanotribological properties of carbon-based thin films: a review. 2010, *28* (1), 51-70.

193. Sun, J.; Zhang, Y.; Liu, Z. J. C., Direct chemical vapor deposition growth of graphene on insulating substrates. 2016, *2* (1), 9-18.

194. Bo, Z.; Yang, Y.; Chen, J.; Yu, K.; Yan, J.; Cen, K. J. N., Plasma-enhanced chemical vapor deposition synthesis of vertically oriented graphene nanosheets. 2013, *5* (12), 5180-5204.

195. Meyyappan, M. J. J. o. P. D. A. P., Plasma nanotechnology: past, present and future. 2011, *44* (17), 174002.

196. Hummel, R. E., Electrical properties of materials. In *Understanding Materials Science*, Springer: 1998; pp 180-216.

197. Keimer, B.; Moore, J. J. N. P., The physics of quantum materials. 2017, *13* (11), 1045-1055.

198. Cramer, A.; Varshney, K.; Gundrum, T.; Gerbeth, G. J. F. m.; instrumentation, Experimental study on the sensitivity and accuracy of electric potential local flow measurements. 2006, *17* (1), 1-11.

199. Nekoofar, M.; Ghandi, M.; Hayes, S.; Dummer, P. J. I. e. j., The fundamental operating principles of electronic root canal length measurement devices. 2006, *39* (8), 595-609.

200. Smith, R.; Liang, C.; Landry, M.; Nelson, J.; Schadler, L. J. I. T. o. D.; Insulation, E., The mechanisms leading to the useful electrical properties of polymer nanodielectrics. 2008, *15* (1), 187-196.

201. Mozer, A. J.; Dennler, G.; Sariciftci, N. S.; Westerling, M.; Pivrikas, A.; Österbacka, R.; Juška, G. J. P. R. B., Time-dependent mobility and recombination of the photoinduced charge carriers in conjugated polymer/fullerene bulk heterojunction solar cells. 2005, *72* (3), 035217.

202. Zhao, R., Plasma based synthesis and surface modification of graphene. 2018.

203. Kaiser, A. B.; Skakalova, V. J. C. S. R., Electronic conduction in polymers, carbon nanotubes and graphene. 2011, *40* (7), 3786-3801.

204. Isenberg, J.; Biro, D.; Warta, W. J. P. i. P. R.; Applications, Fast, contactless and spatially resolved measurement of sheet resistance by an infrared method. 2004, *12* (7), 539-552.

205. Miccoli, I.; Edler, F.; Pfnür, H.; Tegenkamp, C. J. J. o. P. C. M., The 100th anniversary of the four-point probe technique: the role of probe geometries in isotropic and anisotropic systems. 2015, *27* (22), 223201.

206. Acar, B.; Tarhan, L. J. R. i. S. E., Effects of cooperative learning on students' understanding of metallic bonding. 2008, *38* (4), 401-420.

207. Sidorov, A. N.; Sherehiy, A.; Jayasinghe, R.; Stallard, R.; Benjamin, D. K.; Yu, Q.; Liu, Z.; Wu, W.; Cao, H.; Chen, Y. P. J. A. P. L., Thermoelectric power of graphene as surface charge doping indicator. 2011, *99* (1), 013115.

208. Rosi, F. J. S.-S. E., Thermoelectricity and thermoelectric power generation. 1968, *11* (9), 833-868.

209. Bougrine, H.; Ausloos, M., Highly Sensitive Method for Simultaneous Measurements of Thermal-Conductivity and Thermoelectric-Power - Fe and Al Examples. *Rev Sci Instrum* 1995, *66* (1), 199-206.

210. Kettler, W. H.; Wernhardt, R.; Rosenberg, M., Differential Ac Method of Thermopower Measurement. *Rev Sci Instrum* 1986, *57* (12), 3053-3058.

211. Sumanasekera, G. U.; Grigorian, L.; Eklund, P. C., Low-temperature thermoelectrical power measurements using analogue subtraction. *Meas Sci Technol* 2000, *11* (3), 273-277.

212. Sumanasekera, G.; Grigorian, L.; Eklund, P. J. M. S.; Technology, Low-temperature thermoelectrical power measurements using analogue subtraction. 2000, *11* (3), 273.

213. Neuville, D. R.; De Ligny, D.; Henderson, G. S. J. R. i. M.; Geochemistry, Advances in Raman spectroscopy applied to earth and material sciences. 2014, *78* (1), 509-541.

214. Lupoi, J. S.; Gjersing, E.; Davis, M. F. J. F. i. b.; biotechnology, Evaluating lignocellulosic biomass, its derivatives, and downstream products with Raman spectroscopy. 2015, *3*, 50.

215. Auner, G. W.; Koya, S. K.; Huang, C.; Broadbent, B.; Trexler, M.; Auner, Z.; Elias, A.; Mehne, K. C.; Brusatori, M. A. J. C.; Reviews, M., Applications of Raman spectroscopy in cancer diagnosis. 2018, *37* (4), 691-717.

216. Caira, M. R., Crystalline polymorphism of organic compounds. In *Design of Organic Solids*, Springer: 1998; pp 163-208.

217. Popov, V. N.; Henrard, L.; Lambin, P. J. C., Resonant Raman spectra of graphene with point defects. 2009, *47* (10), 2448-2455.

218. Rao, R.; Podila, R.; Tsuchikawa, R.; Katoch, J.; Tishler, D.; Rao, A. M.; Ishigami, M. J. A. n., Effects of layer stacking on the combination Raman modes in graphene. 2011, *5* (3), 1594-1599.

219. Das, A.; Chakraborty, B.; Sood, A. J. B. o. M. S., Raman spectroscopy of graphene on different substrates and influence of defects. 2008, *31* (3), 579-584.

220. Feng, Y.; Trainer, D. J.; Peng, H.; Liu, Y.; Chen, K. J. J. o. M. S.; Technology, Safe growth of graphene from non-flammable gas mixtures via chemical vapor deposition. 2017, *33* (3), 285-290.

221. Wang, Y. Y.; Ni, Z. H.; Yu, T.; Shen, Z. X.; Wang, H. M.; Wu, Y. H.; Chen, W.; Shen Wee, A. T. J. T. J. o. P. C. C., Raman studies of monolayer graphene: the substrate effect. 2008, *112* (29), 10637-10640.

222. Tonndorf, P.; Schmidt, R.; Böttger, P.; Zhang, X.; Börner, J.; Liebig, A.; Albrecht, M.; Kloc, C.; Gordan, O.; Zahn, D. R. J. O. e., Photoluminescence emission and Raman response of monolayer MoS 2, MoSe 2, and WSe 2. 2013, *21* (4), 4908-4916.

223. O'Brien, M.; McEvoy, N.; Hallam, T.; Kim, H.-Y.; Berner, N. C.; Hanlon, D.; Lee, K.; Coleman, J. N.; Duesberg, G. S. J. S. r., Transition metal dichalcogenide growth via close proximity precursor supply. 2014, *4* (1), 1-7.

224. Berkdemir, A.; Gutiérrez, H. R.; Botello-Méndez, A. R.; Perea-López, N.; Elías, A. L.; Chia, C.-I.; Wang, B.; Crespi, V. H.; López-Urías, F.; Charlier, J.-C. J. S. r., Identification of individual and few layers of WS2 using Raman Spectroscopy. 2013, *3* (1), 1-8.

225. Sánchez-Portal, D.; Hernandez, E. J. P. R. B., Vibrational properties of single-wall nanotubes and monolayers of hexagonal BN. 2002, *66* (23), 235415.

226. Thripuranthaka, M.; Rout, C. S.; Late, D. J. J. M. R. E., MoS2 nanoparticles and h-BN nanosheets from direct exfoliation of bulk powder: one-step synthesis method. 2014, *1* (3), 035038.

227. Zeng, H.; Liu, G.-B.; Dai, J.; Yan, Y.; Zhu, B.; He, R.; Xie, L.; Xu, S.; Chen, X.; Yao, W. J. S. r., Optical signature of symmetry variations and spin-valley coupling in atomically thin tungsten dichalcogenides. 2013, *3* (1), 1-5.

228. Laleyan, D. A.; Mengle, K.; Zhao, S.; Wang, Y.; Kioupakis, E.; Mi, Z. J. O. e., Effect of growth temperature on the structural and optical properties of few-layer hexagonal boron nitride by molecular beam epitaxy. 2018, *26* (18), 23031-23039.

229. Postek, M. T., The scanning electron microscope. 1997.

230. Andrade, J. D., X-ray photoelectron spectroscopy (XPS). In *Surface and interfacial aspects of biomedical polymers*, Springer: 1985; pp 105-195.

231. Hu, Y. Two-dimensional (2D) functional molecular networks. UCL (University College London), 2016.

232. Hepburn, J. W. J. C. S. R., Photoelectron spectroscopy in a new light: zero kinetic energy (ZEKE) photoelectron spectrosocopy with coherent vacuum ultraviolet light. 1996, *25* (4), 281-287.

233. Zhang, F.-Y.; Advani, S. G.; Prasad, A. K.; Boggs, M. E.; Sullivan, S. P.; Beebe Jr, T. P. J. E. A., Quantitative characterization of catalyst layer degradation in PEM fuel cells by X-ray photoelectron spectroscopy. 2009, *54* (16), 4025-4030.

234. Binnig, G.; Quate, C. F.; Gerber, C. J. P. r. l., Atomic force microscope. 1986, *56* (9), 930.

235. Park, J.; Kim, M. S.; Cha, E.; Kim, J.; Choi, W. J. S. R., Synthesis of uniform single layer WS2 for tunable photoluminescence. 2017, *7* (1), 1-8.

236. Park, S.; Hu, Y.; Hwang, J. O.; Lee, E.-S.; Casabianca, L. B.; Cai, W.; Potts, J. R.; Ha, H.-W.; Chen, S.; Oh, J. J. N. c., Chemical structures of hydrazine-treated graphene oxide and generation of aromatic nitrogen doping. 2012, *3* (1), 1-8.

237. Wang, H.; Maiyalagan, T.; Wang, X., Review on Recent Progress in Nitrogen-Doped Graphene: Synthesis, 2 Characterization, and Its Potential Applications. 2019.

238. Guo, B.; Fang, L.; Zhang, B.; Gong, J. R. J. I. J., Graphene doping: a review. 2011, *1* (2), 80-89.

239. Singh, R. K.; Nalajala, N.; Kar, T.; Schechter, A. J. S. E. o. G., Functionalization of Graphene—A Critical Overview of its Improved Physical, Chemical and Electrochemical Properties. 2019, 139-173.

240. Lv, R.; Chen, G.; Li, Q.; McCreary, A.; Botello-Méndez, A.; Morozov, S.; Liang, L.; Declerck, X.; Perea-López, N.; Cullen, D. A. J. P. o. t. N. A. o. S., Ultrasensitive gas detection of large-area boron-doped graphene. 2015, *112* (47), 14527-14532.

241. Xu, H.; Ma, L.; Jin, Z. J. J. o. E. C., Nitrogen-doped graphene: Synthesis, characterizations and energy applications. 2018, *27* (1), 146-160.

242. Shao, Y.; Zhang, S.; Engelhard, M. H.; Li, G.; Shao, G.; Wang, Y.; Liu, J.; Aksay, I. A.; Lin, Y. J. J. o. M. C., Nitrogen-doped graphene and its electrochemical applications. 2010, *20* (35), 7491-7496.

243. Zhao, R.; Afaneh, T.; Dharmasena, R.; Jasinski, J.; Sumanasekera, G.; Henner, V. J. P. B. C. M., Study of nitrogen doping of graphene via in-situ transport measurements. 2016, *490*, 21-24.

244. Xiong, J.; Jiang, F.; Shi, H.; Xu, J.; Liu, C.; Zhou, W.; Jiang, Q.; Zhu, Z.; Hu, Y. J. A. a. m.; interfaces, Liquid exfoliated graphene as dopant for improving the thermoelectric power factor of conductive PEDOT: PSS nanofilm with hydrazine treatment. 2015, *7* (27), 14917-14925.

245. Cress, C. D.; Schmucker, S. W.; Friedman, A. L.; Dev, P.; Culbertson, J. C.; Lyding, J. W.; Robinson, J. T. J. A. n., Nitrogen-doped graphene and twisted bilayer graphene via hyperthermal ion implantation with depth control. 2016, *10* (3), 3714-3722.

246. Zhao, R.; Ahktar, M.; Alruqi, A.; Dharmasena, R.; Jasinski, J. B.; Thantirige, R. M.; Sumanasekera, G. U. J. M. R. E., Electrical transport properties of graphene nanowalls grown at low temperature using plasma enhanced chemical vapor deposition. 2017, *4* (5), 055007.

247. Wang, C.; Zhou, Y.; He, L.; Ng, T.-W.; Hong, G.; Wu, Q.-H.; Gao, F.; Lee, C.-S.; Zhang, W. J. N., In situ nitrogen-doped graphene grown from polydimethylsiloxane by plasma enhanced chemical vapor deposition. 2013, *5* (2), 600-605.

248. Berciaud, S.; Ryu, S.; Brus, L. E.; Heinz, T. F. J. N. l., Probing the intrinsic properties of exfoliated graphene: Raman spectroscopy of free-standing monolayers. 2009, *9* (1), 346-352.

249. Zhao, R.; Jayasingha, R.; Sherehiy, A.; Dharmasena, R.; Akhtar, M.; Jasinski, J. B.; Wu, S.-Y.; Henner, V.; Sumanasekera, G. U. J. T. J. o. P. C. C., In situ transport measurements and band gap formation of fluorinated graphene. 2015, *119* (34), 20150-20155.

250. Joucken, F.; Henrard, L.; Lagoute, J. J. P. R. M., Electronic properties of chemically doped graphene. 2019, *3* (11), 110301.

251. Mazumder, P.; Kulkarni, S.; Bhattacharya, M.; Sun, J. P.; Haddad, G. I. J. P. o. t. I., Digital circuit applications of resonant tunneling devices. 1998, *86* (4), 664-686.

252. Su, M.; Chen, C.; Rajan, S. J. S. S.; Technology, Prospects for the application of GaN power devices in hybrid electric vehicle drive systems. 2013, *28* (7), 074012.

253. Zheng, L.; Fertig, H. A., Wigner-Crystal States for the 2-Dimensional Electron-Gas in a Double-Quantum-Well System. *Phys Rev B* 1995, *52* (16), 12282-12290.

254. Yang, C. L.; Zhang, J.; Du, R. R.; Simmons, J. A.; Reno, J. L., Zener tunneling between Landau orbits in a high-mobility two-dimensional electron gas. *Phys Rev Lett* 2002, *89* (7).

255. Lo, Y.; Kolbas, R. J. A. p. l., Phonon-assisted stimulated emission in thin (< 55 Å) AlGaAs-GaAs-AlGaAs single quantum wells. 1988, *53* (23), 2266-2268.

256. Eisentein, J.; Gramila, T.; Pfeiffer, L.; West, K. J. S. s., Resonant tunneling in GaAs/AlGaAs double quantum wells. 1992, *267* (1-3), 377-382.

257. Feenstra, R. M.; Jena, D.; Gu, G. J. J. o. A. P., Single-particle tunneling in doped graphene-insulator-graphene junctions. 2012, *111* (4), 043711.

258. Van Hoof, C.; Genoe, J.; Portal, J.; Borghs, G. J. P. R. B., Charge accumulation in the two-dimensional electron gas emitter of a resonant-tunneling diode. 1995, *52* (3), 1516.

259. Lake, R.; Klimeck, G.; Datta, S. J. P. R. B., Rate equations from the Keldysh formalism applied to the phonon peak in resonant-tunneling diodes. 1993, *47* (11), 6427.

260. Roy, T.; Liu, L.; De La Barrera, S.; Chakrabarti, B.; Hesabi, Z.; Joiner, C.; Feenstra, R. M.; Gu, G.; Vogel, E. J. A. P. L., Tunneling characteristics in chemical vapor deposited graphene–hexagonal boron nitride–graphene junctions. 2014, *104* (12), 123506.

261. Britnell, L.; Gorbachev, R.; Geim, A.; Ponomarenko, L.; Mishchenko, A.; Greenaway, M.; Fromhold, T.; Novoselov, K.; Eaves, L. J. N. c., Resonant tunnelling and negative differential conductance in graphene transistors. 2013, *4* (1), 1-5.

262. Lin, Y.-C.; Ghosh, R. K.; Addou, R.; Lu, N.; Eichfeld, S. M.; Zhu, H.; Li, M.-Y.; Peng, X.; Kim, M. J.; Li, L.-J. J. N. c., Atomically thin resonant tunnel diodes built from synthetic van der Waals heterostructures. 2015, *6* (1), 1-6.

263. Cornescu, A. C. High efficiency and high frequency resonant tunneling diode sources. University of Glasgow, 2019.

264. Wang, S.; Tan, L. Z.; Wang, W.; Louie, S. G.; Lin, N. J. P. R. L., Manipulation and characterization of aperiodical graphene structures created in a two-dimensional electron gas. 2014, *113* (19), 196803.

265. Feng, S.; Liu, C.; Zhu, Q.; Su, X.; Qian, W.; Sun, Y.; Wang, C.; Li, B.; Chen, M.; Chen, L. J. N. C., An ultrasensitive molybdenum-based double-heterojunction phototransistor. 2021, *12* (1), 1-8.

266. Cai, Z.; Liu, B.; Zou, X.; Cheng, H.-M. J. C. r., Chemical vapor deposition growth and applications of two-dimensional materials and their heterostructures. 2018, *118* (13), 6091-6133.

267. Island, J. O.; Steele, G. A.; van der Zant, H. S.; Castellanos-Gomez, A. J. D. M., Environmental instability of few-layer black phosphorus. 2015, *2* (1), 011002.

268. Alruqi, A.; Zhao, R.; Jasinski, J.; Sumanasekera, G. J. N., Graphene-WS2 heterostructures by a lithography free method: their electrical properties. 2019, *30* (27), 275704.

269. Jayasingha, R.; Sherehiy, A.; Wu, S.-Y.; Sumanasekera, G. J. N. l., In situ study of hydrogenation of graphene and new phases of localization between metal–insulator transitions. 2013, *13* (11), 5098-5105.

270. Eksik, O.; Gao, J.; Shojaee, S. A.; Thomas, A.; Chow, P.; Bartolucci, S. F.; Lucca, D. A.; Koratkar, N. J. A. n., Epoxy nanocomposites with two-dimensional transition metal dichalcogenide additives. 2014, *8* (5), 5282-5289.

271. Novoselov, K.; Mishchenko, o. A.; Carvalho, o. A.; Castro Neto, A. J. S., 2D materials and van der Waals heterostructures. 2016, *353* (6298), aac9439.

272. Gannett, W.; Regan, W.; Watanabe, K.; Taniguchi, T.; Crommie, M.; Zettl, A. J. A. P. L., Boron nitride substrates for high mobility chemical vapor deposited graphene. 2011, *98* (24), 242105.

273. Georgiou, T.; Jalil, R.; Belle, B. D.; Britnell, L.; Gorbachev, R. V.; Morozov, S. V.; Kim, Y.-J.; Gholinia, A.; Haigh, S. J.; Makarovsky, O. J. N. n., Vertical field-effect transistor based on graphene–WS 2 heterostructures for flexible and transparent electronics. 2013, *8* (2), 100-103.

274. Lan, C.; Li, C.; Wang, S.; He, T.; Zhou, Z.; Wei, D.; Guo, H.; Yang, H.; Liu, Y. J. J. o. M. C. C., Highly responsive and broadband photodetectors based on WS 2–graphene van der Waals epitaxial heterostructures. 2017, *5* (6), 1494-1500.

275. Lin, Y.-F.; Li, W.; Li, S.-L.; Xu, Y.; Aparecido-Ferreira, A.; Komatsu, K.; Sun, H.; Nakaharai, S.; Tsukagoshi, K. J. N., Barrier inhomogeneities at vertically stacked graphene-based heterostructures. 2014, *6* (2), 795-799.

276. Watt, F.; Bettiol, A.; Van Kan, J.; Teo, E. J.; Breese, M. J. I. J. o. N., Ion beam lithography and nanofabrication: a review. 2005, *4* (03), 269-286.

277. Wang, H.; Wu, T. J. N. r. l., A general lithography-free method of microscale/nanoscale fabrication and patterning on Si and Ge surfaces. 2012, *7* (1), 1-7.

278. Bao, W.; Liu, G.; Zhao, Z.; Zhang, H.; Yan, D.; Deshpande, A.; LeRoy, B.; Lau, C. N. J. N. R., Lithography-free fabrication of high quality substrate-supported and freestanding graphene devices. 2010, *3* (2), 98-102.

279. Cho, S.; Lee, K.; Yuen, J.; Wang, G.; Moses, D.; Heeger, A. J.; Surin, M.; Lazzaroni, R. J. J. o. a. p., Thermal annealing-induced enhancement of the field-effect mobility of regioregular poly (3-hexylthiophene) films. 2006, *100* (11), 114503.

280. Seo, J.-H.; Park, J. H.; Kim, S.-I.; Park, B. J.; Ma, Z.; Choi, J.; Ju, B.-K. J. J. o. n.; nanotechnology, Nanopatterning by laser interference lithography: applications to optical devices. 2014, *14* (2), 1521-1532.

281. Khadpekar, A. J.; Khan, M.; Sose, A.; Majumder, A. J. S. r., Low Cost and Lithography-free stamp fabrication for Microcontact printing. 2019, *9* (1), 1-8.

282. Wood, J. D.; Schmucker, S. W.; Lyons, A. S.; Pop, E.; Lyding, J. W. J. N. l., Effects of polycrystalline Cu substrate on graphene growth by chemical vapor deposition. 2011, *11* (11), 4547-4554.

283. Zhang, Y.; Gomez, L.; Ishikawa, F. N.; Madaria, A.; Ryu, K.; Wang, C.; Badmaev, A.; Zhou, C. J. T. J. o. P. C. L., Comparison of graphene growth on single-crystalline and polycrystalline Ni by chemical vapor deposition. 2010, *1* (20), 3101-3107.

284. Yao, Y.; Li, Z.; Lin, Z.; Moon, K.-S.; Agar, J.; Wong, C. J. T. J. o. P. C. C., Controlled growth of multilayer, few-layer, and single-layer graphene on metal substrates. 2011, *115* (13), 5232-5238.

285. Dong, X.; Wang, P.; Fang, W.; Su, C.-Y.; Chen, Y.-H.; Li, L.-J.; Huang, W.; Chen, P. J. C., Growth of large-sized graphene thin-films by liquid precursor-based chemical vapor deposition under atmospheric pressure. 2011, *49* (11), 3672-3678.

286. Yu, Q.; Lian, J.; Siriponglert, S.; Li, H.; Chen, Y. P.; Pei, S.-S. J. A. p. l., Graphene segregated on Ni surfaces and transferred to insulators. 2008, *93* (11), 113103.

287. Mrlík, M.; Ilčíková, M.; Cvek, M.; Urbánek, P.; Pavlínek, V.; Mosnáček, J. In *Controllable reduction of graphene oxide/poly (Butyl acrylate) hybrids under ATRP conditions*, 8th International Conference on Nanomaterials-Research & Application (NANOCON 2016), TANGER Ltd.: 2016.

288. Malesevic, A.; Vitchev, R.; Schouteden, K.; Volodin, A.; Zhang, L.; Van Tendeloo, G.; Vanhulsel, A.; Van Haesendonck, C. J. N., Synthesis of few-layer graphene via microwave plasma-enhanced chemical vapour deposition. 2008, *19* (30), 305604.

289. Sun, J.; Chen, Y.; Cai, X.; Ma, B.; Chen, Z.; Priydarshi, M. K.; Chen, K.; Gao, T.; Song, X.; Ji, Q. J. N. R., Direct low-temperature synthesis of graphene on various glasses by plasma-enhanced chemical vapor deposition for versatile, cost-effective electrodes. 2015, *8* (11), 3496-3504.

290. Britnell, L.; Gorbachev, R. V.; Jalil, R.; Belle, B. D.; Schedin, F.; Katsnelson, M. I.; Eaves, L.; Morozov, S. V.; Mayorov, A. S.; Peres, N. M. J. N. l., Electron tunneling through ultrathin boron nitride crystalline barriers. 2012, *12* (3), 1707-1710.

291. Qian, F.; Deng, J.; Xiong, F.; Dong, Y.; Hu, L.; Pan, G.; Wang, Q.; Xie, Y.; Sun, J.; Xu, C. J. O. M. E., Direct growth of high quality graphene nanowalls on dielectric surfaces by plasma-enhanced chemical vapor deposition for photo detection. 2020, *10* (11), 2909-2918.

292. Han, T.; Liu, H.; Chen, S.; Chen, Y.; Wang, S.; Li, Z. J. M., Fabrication and Characterization of MoS2/h-BN and WS2/h-BN Heterostructures. 2020, *11* (12), 1114.

293. Koepke, J. C.; Wood, J. D.; Chen, Y.; Schmucker, S. W.; Liu, X.; Chang, N. N.; Nienhaus, L.; Do, J. W.; Carrion, E. A.; Hewaparakrama, J. J. C. o. M., Role of pressure in the growth of hexagonal boron nitride thin films from ammonia-borane. 2016, *28* (12), 4169-4179.

294. Alruqi, A.; Khan Musa, M. R.; Zhao, R.; Zhang, C.; Jasinski, J. B.; Yu, M.; Sumanasekera, G. J. T. J. o. P. C. C., Layer-dependent hydrazine adsorption properties in few-layer Ws2. 2019, *123* (20), 13167-13173.

295. Seiro, S. S. Scanning tunneling spectroscopy across the insulator-to-metal transition in strained manganite films. University of Geneva, 2008.

296. Sirohi, A.; SanthiBhushan, B.; Srivastava, A. J. J. o. M. M., Charge transport in polythiophene molecular device: DFT analysis. 2021, *27* (3), 1-10.

297. Gonnelli, R.; Paolucci, F.; Piatti, E.; Sharda, K.; Sola, A.; Tortello, M.; Nair, J. R.; Gerbaldi, C.; Bruna, M.; Borini, S. J. S. R., Temperature dependence of electric transport in few-layer graphene under large charge doping induced by electrochemical gating. 2015, *5* (1), 1-8.

298. Chen, X.; Wu, Z.; Xu, S.; Wang, L.; Huang, R.; Han, Y.; Ye, W.; Xiong, W.; Han, T.; Long, G. J. N. c., Probing the electron states and metal-insulator transition mechanisms in molybdenum disulphide vertical heterostructures. 2015, *6* (1), 1-8.

299. Jariwala, D.; Srivastava, A.; Ajayan, P. M. J. J. o. n.; nanotechnology, Graphene synthesis and band gap opening. 2011, *11* (8), 6621-6641.

300. Shi, Y.; Liang, X.; Yuan, B.; Chen, V.; Li, H.; Hui, F.; Yu, Z.; Yuan, F.; Pop, E.; Wong, H.-S. P. J. N. E., Electronic synapses made of layered two-dimensional materials. 2018, *1* (8), 458-465.

301. Paur, M.; Molina-Mendoza, A. J.; Polyushkin, D.; de Vasconcellos, S. M.; Bratschitsch, R.; Mueller, T. J. D. M., Resonant photocurrent from a single quantum emitter in tungsten diselenide. 2020, *7* (4), 045021.

302. Fralaide, M. O., *Electrical transport and photoconduction in ambipolar tungsten diselenide and n-type indium selenide*. Southern Illinois University at Carbondale: 2015.

303. Balestra, F.; Ghibaudo, G. J. S.-s. e., Brief review of the MOS device physics for low temperature electronics. 1994, *37* (12), 1967-1975.

304. Aktas, S.; Boz, F. K.; Dalgic, S. S. J. P. E. L.-d. S.; Nanostructures, Electric and magnetic field effects on the binding energy of a hydrogenic donor impurity in a coaxial quantum well wire. 2005, *28* (1), 96-105.

305. Xia, F.; Perebeinos, V.; Lin, Y.-m.; Wu, Y.; Avouris, P. J. N. n., The origins and limits of metal–graphene junction resistance. 2011, *6* (3), 179-184.

306. Lundstrom, M. J. I. E. D. L., Elementary scattering theory of the Si MOSFET. 1997, *18* (7), 361-363.

307. Marahatta, A. B. J. I. J. o. P. S.; Technologies, Effect of n-Type Dopant Nitrogen in the Structure and Atomic Charges Distribution of Monolayer Graphene Sheet: A DFT Analysis. 2019, *16* (2), 01-13.

308. Chakrapani, V.; Angus, J. C.; Anderson, A. B.; Wolter, S. D.; Stoner, B. R.; Sumanasekera, G. U. J. s., Charge transfer equilibria between diamond and an aqueous oxygen electrochemical redox couple. 2007, *318* (5855), 1424-1430.

309. Mishchenko, A.; Tu, J.; Cao, Y.; Gorbachev, R. V.; Wallbank, J.; Greenaway, M.; Morozov, V.; Morozov, S.; Zhu, M.; Wong, S. J. N. n., Twist-controlled resonant tunnelling in graphene/boron nitride/graphene heterostructures. 2014, *9* (10), 808-813.

310. Kang, H.; Yun, Y.; Park, J.; Kim, J.; Truong, T. K.; Kim, J.-G.; Park, N.; Yun, H.; Lee, S. W.; Lee, Y. H. J. N., Quantum Hall conductance of graphene combined with charge-trap memory operation. 2015, *26* (34), 345202.

311. Jiayi, L.; Yi, D.; Zhang, D. W.; Peng, Z. J. A. P.-C. S., Photodetectors based on two-dimensional materials and their van der Waals heterostructures. 2019, *35* (10), 1058-1077.

312. Kang, S.; Lee, D.; Kim, J.; Capasso, A.; Kang, H. S.; Park, J.-W.; Lee, C.-H.; Lee, G.-H. J. D. M., 2D semiconducting materials for electronic and optoelectronic applications: potential and challenge. 2020, *7* (2), 022003.

313. Panin, G. N. J. C., Solitons; Fractals, Optoelectronic dynamic memristor systems based on two-dimensional crystals. 2021, *142*, 110523.

314. Liu, K.; Yan, Q.; Chen, M.; Fan, W.; Sun, Y.; Suh, J.; Fu, D.; Lee, S.; Zhou, J.; Tongay, S. J. N. l., Elastic properties of chemical-vapor-deposited monolayer MoS2, WS2, and their bilayer heterostructures. 2014, *14* (9), 5097-5103.

315. Li, M.-Y.; Chen, C.-H.; Shi, Y.; Li, L.-J. J. M. T., Heterostructures based on two-dimensional layered materials and their potential applications. 2016, *19* (6), 322-335.

316. Lotsch, B. V. J. A. R. o. M. R., Vertical 2D heterostructures. 2015, *45*, 85-109.

317. Chou, S.; Harris Jr, J. J. A. p. l., Room-temperature observation of resonant tunneling through an AlGaAs/GaAs quasiparabolic quantum well grown by molecular beam epitaxy. 1988, *52* (17), 1422-1424.

318. Alzahrani, A.; Alruqi, A.; Karki, B.; Koralalage, M. K.; Jasinski, J.; Sumanasekera, G. J. N. E., Direct fabrication and characterization of vertically stacked Graphene/h-BN/Graphene tunnel junctions. 2021, *2* (4), 040010.

319. Campbell, P. M.; Tarasov, A.; Joiner, C. A.; Ready, W. J.; Vogel, E. M. J. J. o. A. P., Band structure effects on resonant tunneling in III-V quantum wells versus two-dimensional vertical heterostructures. 2016, *119* (2), 024503.

320. Wang, H.; Zhao, Y.; Xie, Y.; Ma, X.; Zhang, X. J. J. o. S., Recent progress in synthesis of two-dimensional hexagonal boron nitride. 2017, *38* (3), 031003.

321. Dresselhaus, M.; Jorio, A.; Souza Filho, A.; Saito, R. J. P. T. o. t. R. S. A. M., Physical; Sciences, E., Defect characterization in graphene and carbon nanotubes using Raman spectroscopy. 2010, *368* (1932), 5355-5377.

322. Inaba, H.; Kurosawa, K.; Okuda, M. J. J. j. o. a. p., Resonant tunneling in double-barrier structures with trapezoidal potential profiles. 1989, *28* (11R), 2201.

323. Ainslie, M. A. J. T. J. o. t. A. S. o. A., Reflection and transmission coefficients for a layered fluid sediment overlying a uniform solid substrate. 1996, *99* (2), 893-902.

324. Yamamoto, H. J. A. P. A., Resonant tunneling condition and transmission coefficient in a symmetrical one-dimensional rectangular double-barrier system. 1987, *42* (3), 245-248.

325. Mahmud, K.; Kutz, J.; Reinhardt, W. J. P. R. A., Bose-Einstein condensates in a one-dimensional double square well: Analytical solutions of the nonlinear Schrödinger equation. 2002, *66* (6), 063607.

326. Shao, Z.-a.; Porod, W.; Lent, C. S. J. P. R. B., Transmission resonances and zeros in quantum waveguide systems with attached resonators. 1994, *49* (11), 7453.

327. Van Delft, D.; Kes, P. J. P. T., The discovery of superconductivity. 2010, *63* (9), 38-43.

328. Schmalian, J. J. M. P. L. B., Failed theories of superconductivity. 2010, *24* (27), 2679-2691.

329. Buckel, W.; Kleiner, R., *Superconductivity: fundamentals and applications*. John Wiley & Sons: 2008.

330. Kunzler, J. J. R. o. M. P., Superconductivity in high magnetic fields at high current densities. 1961, *33* (4), 501.

331. Gavaler, J.; Talvacchio, J. *Superconducting Electronic Film Structures*; WESTINGHOUSE SCIENCE AND TECHNOLOGY CENTER PITTSBURGH PA: 1991.

332. Xin, Y.; Li, W.; Dong, Q.; Yang, T.; Tian, B.; Li, Q. J. S. S.; Technology, Superconductors and Lenz's law. 2020, *33* (5), 055004.

333. Hamlin, J. J., Superconductivity near room temperature. Nature Publishing Group: 2019.

334. Pogosov, W. V.; Combescot, M.; Crouzeix, M. J. P. R. B., Two-Cooper-pair problem and the Pauli exclusion principle. 2010, *81* (17), 174514.

335. Müller, K. A.; Bednorz, J. G. J. S., The discovery of a class of high-temperature superconductors. 1987, *237* (4819), 1133-1139.

336. Lee, D.; Selvamanickam, V.; Salama, K. J. P. C. S., Influences of Y2BaCuO5 particle size and content on the transport critical current density of YBa2Cu3Ox superconductor. 1992, *202* (1-2), 83-96.

337. McDonald, D. G.; Peterson, R. L.; Hamilton, C. A.; Harris, R. E.; Kautz, R. L. J. I. T. o. E. D., Picosecond applications of Josephson junctions. 1980, *27* (10), 1945-1965.

338. Ryazanov, V. V.; Bol'ginov, V. V.; Sobanin, D. S.; Vernik, I. V.; Tolpygo, S. K.; Kadin, A. M.; Mukhanov, O. A. J. P. P., Magnetic Josephson junction technology for digital and memory applications. 2012, *36*, 35-41.

339. Kolli, S. K.; Velpula, S.; Yenubari, K. K. J. v., Superconductors in the Field of Communication and Study Various Electric Properties. *6*, 2015-2018.

340. Mei, T. J. I. J. o. M. P. B., Tunneling Effect of Cooper Pairs in a Superconductor-Insulator-Superconductor-Insulator-Superconductor Structure. 2002, *16* (24), 3697-3705.

341. An, J.; Pickett, W. J. P. R. L., Superconductivity of MgB 2: covalent bonds driven metallic. 2001, *86* (19), 4366.

342. Nagamatsu, J.; Nakagawa, N.; Muranaka, T.; Zenitani, Y.; Akimitsu, J. J. n., Superconductivity at 39 K in magnesium diboride. 2001, *410* (6824), 63-64.

343. Fan, Y.; Ru-Shan, H.; Ning-Hua, T.; Wei, G. J. C. p. l., Electronic structural properties and superconductivity of diborides in the MgB2 structure. 2002, *19* (9), 1336.

344. Antropov, V.; Belashchenko, K.; Van Schilfgaarde, M.; Rashkeev, S. J. a. p. c.-m., Electronic structure, bonding and optical spectrum of MgB2. 2001.

345. Xi, X.; Zeng, X.; Soukiassian, A.; Jones, J.; Hotchkiss, J.; Zhong, Y.; Brubaker, C.; Liu, Z.-K.; Lettieri, J.; Schlom, D. G. J. S. S.; Technology, Thermodynamics and thin film deposition of MgB2 superconductors. 2002, *15* (3), 451.

346. Rafailov, P.; Dworzak, M.; Thomsen, C. J. S. s. c., Luminescence and Raman spectroscopy on MgB2. 2002, *122* (7-8), 455-458.

# CURRICULUM VITAE

NAME: Ali Alzahrani

ADDRESS: Department of Physics and Astronomy

102 Natural Science Building
University of Louisville
Louisville, KY, 40292

EMAIL: amsy2014@hotmail.com

EDUCATION:

Ph. D.: Department of Physics &Astronomy May 2022

University of Louisville – Kentucky, U.S.A GPA: 3.89/4

Master: Department of Physics &Astronomy December 2019

University of Louisville – Kentucky, U.S.A GPA: 3.89/4

Master: Department of Physics

Western Illinois University– Illinois, U.S.A GPA: 3.193/4

Bachelor: Department of Physics

Umm-Al-Qura-University – Makkah, Saudi Arabia. May 2005

EMPLOYMENT HISTORY:

| | |
|---|---|
| Science Teacher at Middle School | 2005 to 2006 |
| Arar City, Saudi Arabia. | |
| Physics Teacher at High School | |
| Bisha City, Saudi Arabia. | 2006 to 2009 |
| Physics Teacher at High School | |
| Al-Baha City, Saudi Arabia. | 2009 to 2010 |
| Teaching Assistance, Umm-Al-Qura-University | |
| Makkah City, Saudi Arabia. | 2010 to 2022 |

PUBLICATIONS & PRESENTATIONS:

1- “Direct fabrication and characterization of vertically stacked Graphene/h-BN/Graphene tunnel junctions” *Ali Alzahrani, Adel Alruqi, Bhupendra Karki, K.K.M.B. Adikaram, Jacek Jasinski, Gamini Sumanasekera.* Ali Alzahrani *et al* 2021 *Nano Ex.* 2 040010.

2- “DIRECT FABRICATION OF VERTICALLY STACKED DOUBLE BARRIER TUNNEL JUNCTIONS BASED ON GRAPHENE AND h-BN” *Ali Alzahrani, K.K.M.B. Adikaram, Jacek Jasinski, Gamini Sumanasekera. Electronic Materials Letters.*

3- “DIRECT FABRICATION AND CHARACTERIZATION OF VERTICALLY STACKED $MgB_2$ /h-BN/ $MgB_2$ TUNNEL JUNCTIONS” *Ali Alzahrani, K.K.M.B. Adikaram, Hank Paxton, Gamini Sumanasekera. (*Will be submitted soon).

4- “Interference Colors of Crystal Quartz Due to Optical Activity under Sunlight IIIumination” Oral Presentation, Western Illinois University.

5- “Heat Diffusion” Oral Presentation, GSRRC (2019), University of Louisville, Kentucky.

6- “2D MATERIALS BASED HETEROSTRUCTURES FOR QUANTUM TUNNELING: A LITHOGRAPHY FREE TECHNIQUE” Oral Presentation, GSRRC (2022), University of Louisville, Kentucky.

7-The 5th International Conference and Exhibition on Lasers, Optics and Photonics” Oral Presentation” Poster” during November 28-30,2016 in Atlanta, USA.

8- “Advances in the Casimir force and heat transfer phenomena”, London, UK,2022

9- 12th International Conference on Applied Physics and Mathematics, Singapore (2022).

10- “Direct fabrication and characterization of vertically stacked Graphene/h-BN/Graphene tunnel junctions” Oral Presentation,2022 International Conference of Advanced Research in Applied Science, Engineering, and Technology (2022).